Human branching cholangiocyte organoids recapitulate functional bile duct formation.

Floris JM Roos[1,2,3], Gilles S van Tienderen[1]*, Haoyu Wu[4]*, Ignacio Bordeu[5,6]*, Dina Vinke[1], Laura Muñoz Albarinos[1], Kathryn Monfils[1], Sabrah Niesten[1], Ron Smits[7], Jorke Willemse[1], Oskar Rosmark[8], Gunilla Westergren-Thorsson[8], Daniel J Kunz[3,6,9], Maurice de Wit[10], Pim J French[11], Ludovic Vallier[2,3], Jan NM IJzermans[1], Richard Bartfai[4], Hendrik Marks[4], Ben D Simons[3,5,6], Martin E van Royen[10], Monique MA Verstegen[1**], Luc JW van der Laan[1 **]

*indicates equally author contribution, **shared senior authorship

[1] Department of Surgery, Erasmus MC Transplant Institute, University Medical Center Rotterdam, Rotterdam, The Netherlands
[2] Wellcome–MRC Cambridge Stem Cell Institute, University of Cambridge, Cambridge, The United Kingdom
[3] Department of Surgery, University of Cambridge and NIHR Cambridge Biomedical Research Centre, Cambridge, Cambridge, The United Kingdom
[4] Radboud University, Department of Molecular Biology, Nijmegen, The Netherlands
[5] Wellcome Trust/Cancer Research UK Gurdon Institute, University of Cambridge, Cambridge, The United Kingdom
[6] Department of Applied Mathematics and Theoretical Physics, Centre for Mathematical Sciences, University of Cambridge, Cambridge, The United Kingdom
[7] Erasmus MC, University Medical Center Rotterdam, Department of Gastroenterology and Hepatology, Rotterdam, The Netherlands
[8] Lung Biology, Department Experimental Medical Science, Lund University, Lund, Sweden
[9] Wellcome Sanger Institute, Wellcome Genome Campus, Hinxton, University of Cambridge, Cambridge, The United Kingdom
[10]Erasmus MC, University Medical Center Rotterdam, Department of Pathology, Rotterdam, The Netherlands
[11]Erasmus MC, University Medical Center Rotterdam, Cancer Treatment Screening Facility, Department of Neurology, Rotterdam, The Netherlands

Keywords. Cholangiocyte organoids, branching morphogenesis, cholangiocarcinoma, disease modelling, cholangiocytes, intrahepatic bile duct, embryonic bile duct development

Corresponding author:
Prof. Dr. Luc JW van der Laan
Erasmus MC, Room NA-1008, department of Surgery
Rotterdam, The Netherlands
Email address: l.vanderlaan@erasmusmc.nl
Phone number: (+31)10-7037757

Highlights

- A branching morphology can be induced in adult intrahepatic cholangiocyte organoids
- Branching cholangiocyte organoids resemble functional tubular structures *in vitro*
- The branching characteristics are comparable to *in vivo* branching organs
- A complex, new cholangiocarcinoma organoid can be established using a similar protocol

eTOC

The intrahepatic bile ducts consist of a complex branching morphology. Here, Roos *et al.* demonstrate that a branching tubular architecture can be induced in human adult intrahepatic cholangiocyte organoids. These, BRCOs faithfully recapitulate aspects of *in vivo* branching organs and can be used to study bile duct development.

Abstract

Human cholangiocyte organoids show great promise for regenerative therapies and *in vitro* modeling of bile duct development and diseases. However, the cyst-like morphology of organoids does not reflect the branching morphology of the intrahepatic bile ducts. BRCOs self-organize into complex tubular structures resembling the intrahepatic bile duct architecture. Single cell transcriptomics and functional analysis showed high similarity to primary cholangiocytes and, importantly, the branching growth mimics aspects of tubular development and is dependent on JAG1/NOTCH2 signaling. Furthermore, branching cholangiocarcinoma organoids (BRCCAO), that display an *in vitro* morphology similar to primary tumors were established using a similar approach. Moreover, these BRCCAOs better match the transcriptomic profile of primary tumors and showed increased chemoresistance to previous cholangiocarcinoma organoids. In conclusion, BRCOs recapitulate a complex process of self-organizing branching morphogenesis in culture. This provides an improved model to study tubular formation, bile duct functionality, and associated biliary diseases.

Introduction

The biliary tree is a complex tubular system compromising the extrahepatic bile duct (EHBD) and intrahepatic bile ducts (IHBDs), that transport bile to the duodenum.[1-3] Cholangiocytes (biliary epithelial cells) line these ducts, providing a physical barrier to bile, and modify its composition.[4,5] Although IHBDs and EHBDs have similar types of cholangiocytes, large morphological differences exist. Most importantly, only IHBDs display a complex branching architecture. Branching is a common phenomenon in organogenesis of mammalian species and in many organs, such as the mammary glands, salivary glands, the pancreatic ducts, and the bile ducts.[6] From all these organs, organoid cultures have been developed providing opportunities to study branching formation *in vitro*. To date, however, no human organoid model from adult tissue has been established that adequately reflects tubular development *in vitro*. Similarly, current cholangiocyte organoid models form cyst-like structures with a fluid-filled lumen surrounded by an epithelial monolayer[7-12], making them unsuitable to study branching morphogenesis and diseases that affect tubular formation *in vitro*.

Here, we report the establishment of branching cholangiocyte organoids (BRCOs) from human adult IHBDs. *In vitro*, BRCOs grow into self-renewing, self-organizing branching structures. BRCO cells closely resemble mature cholangiocytes on a single-cell transcriptome level and recapitulate the heterogeneity of *in vivo* cholangiocytes.[13-16] BRCOs exhibit mature cholangiocyte functional properties, such as alkaline phosphatase (ALP) activity.[5] Ductal growth in BRCOs is tip-driven, their dynamics and spatial organization are behaving according to probabilistic rules, and their tubular formation mimics aspects as seen *in situ*. Furthermore, organoids derived from an Alagille syndrome (AGS) patient[17-19] were unable to branch due to absence of NOTCH signaling. Finally, we demonstrate that branching cholangiocarcinoma (CCA) organoids[20] (BRCCAOs) can be formed from primary CCA tumors. BRCCAOs closely resemble the primary tumor-tissue architecture, transcriptomic profile, and provide a better model for drug responses to clinically relevant chemotherapeutics. Overall, these results demonstrate the unique aspects of this organoid model for studying (malignant) biliary diseases, processes involved in tubular formation, and branching bile duct organization.

Results

Establishment of branching cholangiocyte organoids

During embryonic development the IHBDs develop from the ductal plate under the influence of canonical-WNT signaling.[21] However, at the latter stages of tubular development β-catenin is more tightly regulated[21] and in adulthood cholangiocyte proliferation seems β-catenin independent.[13,14] In addition, it is known that the TGF-β pathway is essential for tubular growth in other branched tissues.[6] Following this rationale, BRCOs were established by applying a two-stage culture method. First, intrahepatic cholangiocyte organoids (ICOs, n=20) were initiated from liver biopsies using standard canonical-WNT stimulating conditions.[7] After 3 passages, medium was replaced by the 'branching-initiation' medium, that simultaneously stimulates (via RSPO1) and inhibits (via Dickkopf-related protein 1 –DKK1) the canonical-WNT pathway, while no longer inhibiting the TGF-β pathway via A83.01. Hereafter, ICOs changed to a branching pattern (Fig. 1A, S1A and methods). BRCOs could be induced from 14/20 (70%) ICO lines, cultured from a variety of liver biopsies (Table S1). No underlying patient characteristics that could compromise branching development, such as donor age or liver disease, were identified. As shown in Fig. S1B, BRCOs could only be established from ICOs and not from extrahepatic cholangiocyte organoids (n=3). Interestingly, only adult ICOs and not fetal-ICOs could develop to BRCO (n=3, Fig. S1C, Table S1). Mostly, the BRCO cultures consist of a variable mix of branching and non-branching (cyst-like) organoids (Fig. S1D, mean % of BRCOs 48.4±SD25.8, n=14). In contrast, once established *in vitro*, BRCOs could be passaged long-term by mechanical dissociation while maintaining a similar branching architecture (>20 passages), without obtaining any common oncogenic mutations or chromosomal instabilities, indicating that when BRCOs are formed, they retain their characteristics under external perturbations.

BRCO cells resemble primary cholangiocytes

BRCOs expand through the elongation of existing branch bifurcations and trifurcations of proliferative tips, resulting in 3D ramified architectures (Fig. 1B, S1A and Video S1). The properties and variabilities between BRCOs were consistent with non-stereotypic branching dynamics (Fig. S1E). When analyzed by electron microscopy, we found that individual cells within BRCOs displayed ultrastructural features of columnar epithelial cells, such as microvilli and tight junctions (Fig. 1C, indicated by arrows). Immunofluorescence staining's for cholangiocyte markers cytokeratin (KRT)19 and 7 showed expression in all cells (Fig. 1D, S1F, Video S2). Nuclei are located at the basolateral side of BRCO cells (Fig. 1SF), with the bulk of cytoplasm being towards the lumen, suggesting cell polarization. This was confirmed by mature cholangiocyte markers for secretin receptor (SCTR, basolateral side), and the pronounced expression of tight-junction marker zonula occludens (ZO-1) which was co-localized with cystic fibrosis transmembrane conductance regulator (CFTR) at the luminal side of tubes (Fig. S1F). Finally, F-actin staining revealed the presence of a lumen while showing increased activity across the luminal side, likely due to staining of microvilli (Fig. 1D, S1F, Video S2). All these cholangiocyte-typic features were similar to the *in vivo* situation.[5] Interestingly, some cells located at the tips were albumin positive (Fig. S1F). qRT-PCR of BRCOs showed expression of typical biliary markers such as *KRT19*, *KRT7*, Hepatocyte nuclear factor-1 beta (*HNF-1β*), Trefoil Factor 1 (*TFF1*) and *TFF2* (Fig. 1E).[15] Compared to ICOs[7], and in line with the albumin staining, BRCOs have higher expression of hepatocyte-related genes such as *SERPINA1* (known as alpha-1

antitrypsin), Albumin (*ALB*), and *CYP3A4* (Fig. 1E), suggesting that some BRCO cells express hepatocyte-related markers, as is found in primary cholangiocytes.[13] In contrast, BRCOs showed limited expression of the shared progenitor/mature cholangiocyte markers *SOX9* and *TROP2*, and the WNT-target gene leucine-rich-repeat-containing G-protein-coupled receptor *(LGR)5* was severely downregulated (P<0.0001) compared to ICOs.[7]

BRCOs recapitulate functional bile ducts *in vitro*

Bright field and confocal imaging of BRCOs suggested that BRCOs have an open lumen (Fig. 1A and D and S1F). This was confirmed by active transport of fluorescent rhodamine-123 into the lumen of BRCOs via multi-drug-receptor-1 (MDR1), revealing a network of connected ducts (Fig. 2A). Blocking MDR1 transporter by verapamil, blocked the transport of rhodamine-123 and caused the fluorescence to reside within the BRCO cells (Fig. 2B). *In vivo*, cholangiocytes regulate bile composition by transportation, secretion, and absorption of ions, bile substances, and water.[5] In order to demonstrate the presence of these functions in BRCOs, we first assessed secretin and somatostatin receptor activity. Upon secretin stimulation, BRCOs swell by active ion transport and increased osmolality and lose their slender tubular structures (Fig. 2C). Somatostatin significantly inhibited swelling (secretin 1.3±0.03 swelling vs. somatostatin addition 1.15±0.05, p=0.01, Fig. 2D), demonstrating the functionality of both receptors, and suggesting functional ion and water transportation via CFTR and aquaporins. Ion channel activity was confirmed in a monolayer of BRCOs using an ussing chamber set up. Forskolin stimulated, and GlyH-101 (CFTR-inhibitor) inhibited short circuit current (Isc), indicating functional CFTR-activity (Fig. 2E). Similarly, upon incubation with uridine 5'-triphosphate, an increase of Isc was observed, which was specifically inhibited by T16Ainh-A01, indicating anoctamin-1 (ANO1) activity. Next, activity of important cholangiocyte enzymes were tested. Similar to cholangiocytes *in vivo*[22], ALP activity was present and primarily located on the luminal side of the BRCOs (Fig. 2F), while gamma-glutamyl transferase (GGT)-activity was also clearly detectable in BRCOs (Fig. 2G).

Finally, to investigate if we could induce hepatocyte-like differentiation within BRCOs, we applied a hepatocyte differentiation protocol.[7] After 14 days of differentiation, BRCOs lost their tubular structures and acquired a denser, cyst-like morphology (Fig. 2I), similar to ICOs in differentiation conditions[7,8] , but contrasted with undifferentiated controls (Fig. 1B, Fig. 2H). Hepatocyte marker expression decreased in BRCOs and increased in ICOs after differentiation, although only a significant difference was observed for *ALB* (Fig. 2J). Interestingly, the opposite was observed for *LGR5* expression (Fig. 2J), that increased in BRCOs and decreased in ICOs after differentiation, however this did not reach statistical significance. When hepatocyte specific function was assessed, clearly protein secretion levels of A1AT and albumin were significantly reduced in BRCOs, while increased in ICOs after hepatic differentiation (p<0.05, Fig. 2K). Collectively, these results indicate that BRCOs recapitulate functional properties of IHBDs. Although some expression of hepatocyte-related genes was observed in BRCOs, hepatic functionality was limited, suggesting that only biliary cells that occasionally express hepatocyte-related genes are present in BRCOs.

Single cell transcriptomic analysis reveals that BRCOs differ from ICOs but are similar to primary cholangiocytes

To fully characterize the transcriptomic differences between ICO and BRCO cells and to capture cellular

heterogeneity within BRCOs, we performed single-cell RNA sequencing (scRNA-seq) using CEL-seq2.[23] In total, 3456 cells were analyzed from 3 donor matched BRCOs and ICOs (Fig. 3A). Using a stringent quality threshold, a similar number of cells (BRCOs: 1105 and ICOs: 1429) were retained, and comparable numbers of genes and UMIs were detected in BRCOs and ICOs (Fig. S2A-C). To identify different cell populations, we performed cluster analysis and applied for the visualization. After batch correction (Fig. S2D and methods) two main groups of cells, separated by organoid type, were observed (Fig. 3B, Sup. File 1). Cluster analysis revealed seven sub-clusters (Fig. 3B) of which clusters 5 and 7 were mainly cells in the G2M and S phases of the cell cycle. ICO cells had high expression of the proliferation marker *Ki67* (83.4% versus 16.6% in BRCOs, Fig. S2E). *In vivo,* mature cholangiocytes are generally quiescent but can proliferate in response to injury or damage.[24-26] When analyzing cell-cycle phases, significantly more G1 cells in BRCOs were found (avg. 75.1%), compared to ICOs (avg. 65.8%; $p<0.05$, Fig. S2E). A similar trend in proliferation was observed via EdU incorporation. EdU was incorporated in more ICOs cells (23.9% ± SD 11.2 EdU^+ cells, n=3) than in BRCOs (10.6% ± SD 2.1, p=0.11, n=3, Fig. S2F), indicating a possible lower proliferating activity in BRCOs. We further explored transcriptomic differences in the non-dividing cell clusters (2-4 vs. 1 and 6), and identified 476 significantly differentially expressed (DE) genes between BRCOs and ICOs (Fig. S2G, Sup. File 1). Pathway analysis revealed that genes upregulated in BRCOs are mostly involved in metabolic processes, while upregulated genes in ICOs are enriched in the Cajal body pathway, normally found in proliferating cells (Fig. S2H). Together, these results suggest that BRCOs have a district gene expression pattern and are less proliferative than ICOs.

Subsequently, we investigated the gene expression of known (im)mature cholangiocyte markers.[15] Although cells from both organoid types express mature cholangiocyte markers such as *EPCAM*, *CD24*, *SOX9*, *KRT7* and *KRT19*, highlighting their biliary origin, we observed significantly decreased expression of *SOX9*, *KRT7* and *KRT19* in BRCOs (Fig. 3C and 3D). Interestingly, previous data indicates that *KRT19* is upregulated in ICOs compared to primary cholangiocytes.[13] In contrast, mature cholangiocyte genes *SPP1* and *LYZ* are significantly higher expressed in BRCOs (Fig. 3C and 3D). In addition, ICO cells express high levels of *MUC5AC* and *MUC5B*, two markers that are hardly detectable in BRCO cells (Fig. 3C and 3D) or in $EPCAM^+$ cells *in vivo*.[13] Furthermore, BRCOs have higher expression of the hepatocyte-related genes *SERPINA1*, *ALB* and *CYP2E1*, confirming previous observations (Fig. 1E). To investigate if BRCOs better resemble human cholangiocytes *in vivo*, we performed gene set enrichment analysis (GSEA) using published datasets of cholangiocyte organoids and their corresponding tissue (see methods).[8] We found that BRCO genes were significantly more enriched in gene sets reflecting the primary tissue (Fig. 4A), including genes such as *UGT2B11*, *UGT2B7*, *CYP3A5*, *AKR1C1*, *AKR1C2*, and *AKR1C3*, which are involved in multiple metabolic pathways. However, as expected, ICO gene enrichment was found to correspond only with organoids (Fig. 4A) and was driven by genes involved in proliferation (*CCNB*, *CDK6*, *CND1*, *PCLAF*, *CKS2*, *DLGAP5*, *TBX3*, and *MAP2K6*). In summary, the scRNA-seq analysis shows that BRCOs differ from ICOs, display less proliferative features, and more importantly better correspond to mature cholangiocytes.

Proteomics of BRCOs confirms differences with ICOs and similarities with cholangiocytes

To investigate differences in protein production between BRCOs and ICOs, we performed stable isotope labeling by amino acids in cell culture (SILAC)-based mass spectrometry (Fig. S3A). A segregation of BRCOs

and ICOs was observed when applying principal component analysis (PCA, PC2-axis, Fig. S3B). We found an overlap of 653 proteins produced in all samples, however no differential expression between these proteins was detected (Fig. S3C). Therefore, we focused on uniquely produced proteins by the organoids and BRCOs produced more unique proteins than ICOs (702 vs. 132, Fig. S3D and F). Furthermore, we noticed that some DE genes from the scRNA-seq analysis, correspond to the production of 36 unique proteins (Fig. S3E and Sup. File 1). Finally, we investigated how these proteins correlate to highly expressed proteins in primary (gallbladder) cholangiocytes.[27] As shown in Fig. S3G, the important cholangiocyte channels SLC12A2 and ABCC3, as well as PDL1 and CLDN2, were solely present in BRCOs. In contrast, ICOs produced CCL20, a protein associated with the biliary disease primary sclerosing cholangitis.[28]

Cellular heterogeneity in BRCOs in relation to heterogeneity of primary intrahepatic cholangiocytes

Next, we focused on the transcriptomic heterogeneity of BRCO cells. Besides the proliferating cluster IV, we identified 3 clusters (I-III) in BRCOs (Fig. 4B). Recent evidence indicates that there is heterogeneity in the intrahepatic cholangiocytes (IHC), with a subset of IHCs expressing hepatocyte-related genes.[13,14] Interestingly, and in line with these observations, cluster I cells distinctly express hepatocyte-related genes: *GC*, *PCK1*, *ALB* and *CYP2E1* (Fig. 3C and Fig. S4C and D). These are likely the cells surrounding the tips of the BRCOs that stained positive for albumin (Fig. S1F). In addition, we identified expression of cholangiocyte markers *TACSTD2*, *TFF1* and *TFF3* in cluster II and III, which are not detectable in cluster I (Fig. 4B), and in cluster II a small group of cells expressing *LGR5* was detected (Fig. 4B). Of note, *CLDN2* was highly expressed in I and II, and almost absent in III. Immunostainings revealed the presence of highly expressing CLDN2 cells in the tips (cluster I) and along the distal part of the tubes (cluster II, Fig. S1F), suggesting that cells from cluster III could be located at the proximal part of the ducts. These results suggest that cells from cluster II and III represent the mature cholangiocyte compartment of the tubular structures, with a few *LGR5*$^{+}$ cells in cluster II maintaining some stem cell-like features.[13]

To further characterize the different cell clusters, we compared our scRNA-seq results to the human adult liver cell atlas.[13,15] Onlyhepatocytes and EPCAM^{+} cells/cholangiocytes, and ICO cells from the atlas were included and compared to the clusters of BRCO and ICO cells. As shown in Fig. 4C, ICO cells from both studies grouped together suggesting proper batch correction. Interestingly, BRCO cells from cluster I (red) grouped closely with primary hepatocytes (Fig. 4C). In contrast, BRCO cells from cluster II (green) are closer to the EPCAM^{+}/cholangiocyte cells, leaving a few *LGR5*$^{+}$ cells separated from the other cells in cluster II (Fig. 4C). BRCO cells from cluster III are in between the EPCAM^{+}/cholangiocyte and hepatocyte clusters (Fig. 4C) and may miss an *in vivo* counterpart. Next, we quantified the transcriptomic relationship between BRCOs and EPCAM^{+}/cholangiocytes using connectivity analysis. Revealing that BRCOs have a higher connectivity (Fig. 4D) to EPCAM^{+}/cholangiocytes (0.10944828) than ICOs (0.0020928). In addition, GSEA confirmed that the majority of BRCO genes are significantly more enriched in primary EPCAM^{+}/cholangiocytes than in ICOs (Fig. 4E, Sup. File 1). Interestingly, pathway analysis subsequently revealed that BRCOs have an enrichment of genes (*PKHD1*, *PAK1*, *BMP2* and *VEGFA)* that are involved in branching morphogenesis of an epithelial tube (GO:0048754).

Finally, to confirm the transcriptomic similarities between BRCOs and primary cholangiocytes and to compare BRCOs to ICO cultured in the same conditions (Tysoe *et al.*[12]) as BRCOs, we integrated our data with previously published scRNA-seq data from these specific ICOs[29] and its matching primary IHC (Fig. S4A). Overall, we found that both ICOs[7,12] were separated and clearly clustered, while BRCO cells and IHCs were more scattered. Sub-cluster analysis of BRCOs showed that especially cluster I and II demonstrate a correlation to primary IHCs, confirming previous analysis (Fig. 4C and S4B). However, the *Ki67*$^{+}$ cluster IV of BRCOs are close to the proliferating cells from both ICOs (Fig. S4B and C). In addition, similar to previous observations, BRCOs express *Ki67* and *LGR5* to a lesser extent than both types of ICOs (Fig. S4C and D), and only BRCO and IHC cells express hepatocyte markers such as *ALB* and *GC* (Fig. S4C and D). Together these analyses confirm that BRCOs have a transcriptome distinct from previous cholangiocyte organoids, that it closely resembles primary IHCs and represents the heterogeneity present in EPCAM^{+} cells *in vivo*.

BRCOs show essential traits of branching morphogenesis *in vitro*

Since BRCOs display a branching morphology, we investigated if their growth dynamics and spatial organization conformed to known morphogenetic programs. EdU incorporation and Ki67 staining's showed that proliferating cells were almost exclusively located on the peripheral tips of the organoids (Fig. 5A, B, and S5A and S5B). This is consistent with tip-driven branching, a feature shared with other branching organs during development.[30] Furthermore, upon contact with surrounding ducts, proliferative tips of BRCOs did not form reconnections or shunts. Instead, we found that under such steric constraints, tips arrested their growth (Fig. S5C). This explained the observed absence of cell proliferation in sub-peripheral regions of BRCOs. Additionally, we observed that, provided there was enough free space around them, two tips could avoid collision by changing their direction of growth, as shown in Video S3. This observation suggests that steric constraints are essential for tip termination to occur.

BRCOs follow probabilistic rules of branching and termination

To gain further insight into the growth dynamics of BRCOs, we reconstructed the spatial organization and topology of the full ductal network of three individual BRCOs at day 5 till day 8 of culture (Fig. 5C and S5D). Quantitative analysis of duct lengths, defined as the length between consecutive branch points, revealed an approximately exponential distribution (Fig. 5D). This suggested that branching is stochastic (probabilistic), with the timings between consecutive bifurcation being un-correlated. Such behavior is consistent with a non-stereotypical program, where branching events are regulated locally, at the individual tip level. Additionally, we observed a lower abundance of short ducts than expected from a purely exponential length distribution (Fig. 5D). This was related to the typical size of tips at the time of branching, which acted as a lower bound for the duct lengths. Altogether, these observations fit a model of stochastic growth and branching for BRCOs *in vitro*, similar to the dynamics observed in branching organs *in vivo*.[29] Within this framework, known as the branching annihilating random walk (BARW), growing proliferative tips perform a "persistent random walk" giving rise to a trail of immobile and proliferatively inactive ductal cells (Fig. 5E). At the same time, growing tips also undergo serial rounds of (stochastic) tip branching, and may terminate growth (or "annihilate") when they come within a critical distance, termed the annihilation radius, of a neighboring duct or tip. Additionally, to account for the self-avoiding behavior, we consider small repulsive interactions between tips and ducts (Fig. 5E). After estimating the model parameters from the data (see Methods), we tested whether BRCO growth fitted

within the framework of the BARW model. For this we segmented and quantified the ductal network organization (Fig. 5F and S5F) and compared the BARW predictions to the data (Methods and Fig. 5F). Morphologically, the model reproduced with high accuracy the distribution of duct lengths and the low abundance of short ducts observed experimentally (Fig. 5D, R^2=0.96). Statistical measures, such as the probability (q_i) that a tip terminates at branch level (*i*) (Fig. 5G, H and S5G, Methods), and topological measures, such as the distribution of the subtree sizes (Fig. 5I), persistence's (Fig. 5J) and tip-to-tip distance (example in Fig. 5F and S5H) showed good agreement with the model (R^2=0.94, R^2=0.92 and R^2=0.97, respectively). These quantitative analyses show that the growth dynamic of BRCOs is consistent with a non-stereotypical, locally regulated branching program, similar to that observed in other branching contexts, *in vivo*.

Key liver developmental pathways are active in BRCOs

Next, we investigated the molecular mechanisms that could drive the tip-driven branching dynamics in BRCOs. Increasing evidence indicates that primary cholangiocytes express WNT-ligands but use β-catenin independent signaling for self-replication and regeneration.[14,31] BRCOs are grown in conditions that both stimulate and inhibit canonical WNT signaling and they are established from ICOs which strongly upregulate WNT/β-catenin target genes compared to IHCs.[9,13] Thus, we investigated if the BRCO and ICO culture conditions affect pathways by examining genes that are crucial for liver development.[32-34] When examining the WNT/β-catenin pathway, we detected significantly lower expression of *LGR5* and *AXIN2* in BRCOs compared to ICOs (Fig. S6A), confirming previous results (Fig. 1E, 3D and S4C). In contrast and as expected, downstream targets of the non-canonical WNT planar cell polarity (PCP) pathway, *JUN* and *JUND*, were significantly elevated in BRCOs (Fig. S6A). With respect to the YAP/HIPPO pathway, we assessed the expression of *YAP1* and its downstream targets.[31,32] *YAP1* expression was slightly upregulated in BRCOs (Fig. S6B), but downstream targets were hardly detectable except for *KLF6* (Fig. S6B).

JAG1/NOTCH2 signaling is essential for branching morphogenesis *in vitro*

Several signaling pathways are known to be involved in branching morphogenesis. For instance, the TGF-β pathway, highly active in BRCOs (Fig. S6c) has been implicated as a termination signal[6] and might contribute to tip termination signals during *in vitro* branching. However, inhibition of TGF-β via A83-01 did not result in arrest of branching *in vitro* (Video S4). Similarly, blockage of retinoic acid synthesis, an important pathway for biliary development[35], did not affect growth or branching dynamics (Fig. S6D). Furthermore, appropriate JAG1/NOTCH2 signaling is required for IHBD development from the hepatoblasts. Inadequate NOTCH signaling, as seen in Alagille syndrome patients, results in a deficient tubular formation.[17] No significant differences for *NOTCH2* and *JAGGED1* (*JAG1*) expression between BRCOs and ICOs was observed (Fig. 6A). However, *JAG1* expression was significantly higher (Fig. S6E, BRCO_posJAG1) in the mature cholangiocytes cluster (cluster 3, Fig. 3B and cluster II, Fig. 4B, 4C and S4C) that is located near the tips, and overlaps with *LGR5* expression, suggesting that *JAG1* could be essential in cells that drive tubular growth. To further investigate the potential involvement of the NOTCH pathway, ICOs were initiated from the same AGS patient previously used to study cholangiocyte organoids.[7] To determine the patient's mutation, MLPA analysis and Sanger sequencing on AGS ICOs was performed. A large heterozygous mutation in *JAG1 (mJAG1)* was found consisting of two large deletions (of 3473 base pairs (bp) and 4811 bp), starting from the last 7 bp of exon 10 and extending to the first 27 bp of exon 24

(Fig. S6F), which confirmed AGS.[18] qRT-PCR and PCR blot analyses confirmed the presence of relatively short mutant mRNA products in AGS ICOs, while being undetectable in healthy ICOs (Fig. S6G and H). As potential compensation of *mJAG1*, AGS ICOs had higher expression of *NOTCH2* compared to healthy ICOs (Fig. S6I). Western Blot analysis confirmed the presence of a mJAG1 protein in AGS ICOs (Fig. 6B). In addition, immunofluorescence showed a clear difference in JAG1 localization. Healthy ICOs predominantly expressed JAG1 at the plasma membrane, while this localized expression was absent in AGS ICOs (Fig. 6C). Although proliferation was diminished in AGS ICOs compared to healthy ICO (22.7%±5.8SD vs. 4.1%±0.3SD p=0.01, Fig. 6D), they formed normal cystic organoids. However, upon switching to branching- medium, AGS ICOs failed to show branching morphogenesis, stopped proliferating, and underwent cell death (Fig. 6E). Addition of exogenous chimeric JAG1 protein to AGS ICOs did not rescue these effects (Fig. S6J), which may be due to limited receptor access or haploinsufficiency.[36] Finally, the involvement of NOTCH signaling in branching morphogenesis of BRCOs was confirmed by using the NOTCH-inhibitor DAPT. At first, BRCOs are forming (24 hours), however within days of DAPT treatment, existing branches are retracting, formation of new branches is completely prevented and partial remodeling to cystic organoids is observed (Fig. 6F). In summary, these results suggest that appropriate JAG1/NOTCH2 signaling is essential for branching morphogenesis in BRCOs.

Cholangiocarcinoma organoids in branching conditions undergo morphological and gene expression changes resembling the primary tumor

One of the hallmarks of cancer is the disturbance of morphological cues resulting in typical dysplastic tumor architecture. Since BRCOs demonstrate a complex architecture, we hypothesized that our culture protocol could aid in modelling CCA. To test this hypothesis, three different CCAO lines were cultured under branching conditions (BRCCAOs). A change in morphology occurred within two weeks of culture, forming dense spheroidal organoids with branch-like outgrowths (Fig. 7A and S7A). H&E staining of BRCCAOs showed formation of multiple peripheral branches with a lumen, variable in diameter, surrounded by compact layers of cells and showed a resemblance to the primary tumor (Fig. 7B). Branches were more tightly packed together compared to BRCOs, and adhered to multiple other tubes, which resulted in multilayered epithelial structures, resembling dysregulated growth of CCAs *in vivo* (Fig. 7B). BRCCAOs showed widespread expression of the CCA tumor marker KRT7 (Fig. S7B).[37]Expression of ZO-1, related to morphogenesis and polarization in tissue,[38] indicated a lack of cellular polarization in BRCCAOs, in contrast to BRCOs (Fig. S1F and S7C). In addition, BRCCAOs showed proliferation in both tips and ducts, as demonstrated by EdU and Ki67 staining (Fig. 7C and S7D). In general, proliferation rates were comparable between CCAOs and BRCCAOs (5.1% ± SD 0.3 vs. 9.2% ± SD 3.1, p=0.1, Fig. S7E). The disorganized proliferation patterns might reflect a compromised tip-inhibition mechanism, resulting in irregular growth, with tightly packed branching-like structures. Quantitative measurements indicate that BRCCAOs were significantly smaller and more circular than BRCOs (Fig. 7D). Qualitatively, the structure of BRCCAOs could be recapitulated in the BARW model proposed for BRCOs by limiting tip-duct interactions (see Methods). Subsequently, the model produced dense and disorganized structures, and reproduced the size-reduction observed in BRCCAOs (Fig. S7F and G). Furthermore, the model indicated that BRCCAOs have an internal and an external structure filled with active tips, as was already seen *in vitro* (Fig. 7D,S7F and G). This data shows that BRCCAOs consist of CCA cells that form a perturbed structure resembling tumor morphology.

To assess if the morphological changes are corroborated by changes in gene expression, bulk transcriptome analysis of BRCCAOs and CCAOs (n=3) was performed.). A pronounced difference in overall gene expression between BRCCAOs and CCAOs was found (PCA, PC2, Fig. S7H). Despite the relatively large interpatient variability (PC1, Fig. S7H), we detected 149 DE genes (Sup. File 1) that were expressed in each tumoroid (Fig. S7I). Regulators of MAPK activity *DUSP1* and *DUSP5*, key effectors of cellular growth and survival[39], were among the most DE genes (Fig. 7E). Similar to BRCOs, *JUN* and *JUND*[40] were upregulated in BRCCAOs, indicating activity of the PCP pathway. GSEA analyses revealed that CCAOs have higher expression of genes related to cellular proliferation (Fig. 7F and S7J), while BRCCAOs show higher expression of genes related to complex cellular pathways (Fig. 7F), including tumor-associated hypoxia (NES 2.85).[41] Interestingly, TGF-β signaling, a pathway directly linked to metastasis and chemo-resistance[42], was upregulated in BRCCAOs compared to CCAOs (Fig. 7F). To investigate whether the BRCCAO transcriptome is more closely related to the primary tumor tissues, a gene correlation analyses was performed. For this, we integrated and filtered RNA-seq data of patient-paired tumor tissue based on the DE genes between BRCCAOs and CCAOs. When comparing CCAO and BRCCAO conditions, a relatively low correlation coefficient (CC) was observed (CC 0.59±0.06). Interestingly, when comparing organoids to primary tumor tissue, BRCCAOs showed a high correlation to CCA tumor (CC 0.80 ±SD 0.05, Fig. 7G). The correlation of CCAOs and CCA tumor was much lower (CC 0.55 ±SD 0.08). Overall, our analyses revealed striking differences between the transcriptome of CCAOs and BRCCAOs, and it shows that the transcriptome of BRCCAO more closely resembles that of the primary CCA tumor.

As cholangiocarcinomas *in vivo*, BRCCAOs are chemo resistant

We postulate that, similar to the transcriptome, the responses to drug treatments in BRCCAOs better reflect the drug responses of primary tumors. Although used as the gold standard for palliative treatment, it is known that primary CCA tumors are quite resistant to gemcitabine and/or cisplatin chemotherapy.[43] Therefore, we incubated CCAOs and BRCCAOs with gemcitabine and/or cisplatin for 72 hours, to mimic single and combinational therapies. Similar to published results[44], CCAOs were resistant to cisplatin monotherapy, as were BRCCAOs. When combining cisplatin (10µM) with different doses of gemcitabine, a clear dose-dependent response on cell viability was detected (Fig. 7H). A remarkable difference in response was observed between BRCCAOs and CCAOs. CCAOs showed the highest sensitivity for the combination treatment with an average gemcitabine IC50 value of 0.388 µM. The sensitivity of BRCCAOs for gemcitabine was > 10.000-fold higher with an average IC50 of 5760 µM ($p<0.001$, Fig. 7H). This effect might be related to the differences in cell proliferation rate, as has been described for primary tumors, however no significant difference was observed (Fig. S7K).[45] This indicates that drug resistance factors, other than proliferation rates, are involved in the insensitivity of BRCCAOs for gemcitabine and cisplatin. In summary, these results demonstrate that BRCCAOs better mimics CCA tumor tissue on a transcriptional level, resulting in a high resistance to chemotherapeutics., At standard regimen dosages for CCA patients (1000 mg/m^2), tumor tissue concentrations of gemcitabine are estimated to range from 24-70 µM.[46-48] At these clinically-relevant concentrations, CCAOs are highly sensitive and die when exposed to gemcitabine, while BRCCAOs remain resistant. Gemcitabine and cisplatin combinational therapy provides patients with only a modest benefit in overall survival[49] and BRCCAOs closely reproduce this response.

Discussion

With the establishment of the biologically relevant BRCOs, we demonstrated that human tissue-derived IHCs can be expanded *in vitro* as self-organizing branching epithelial bile ducts. The transcriptomic profile of BRCOs closely resembles that of *in vivo* IHCs and we show that BRCOs are capable of mimicking tubular formation *in vitro.* Finally, we demonstrate that this culture method can also be applied to model CCA. BRCCAOs form structures with disorganized growth-patterns, and BRCCAO gene expression profiles resemble those of the original tumor. Furthermore, drug-responses in BRCCAOs were more reminiscent of the *in vivo* tumor response. These results demonstrate that our culture method provides a unique *in vitro* model for studying functional bile ducts, aspects of branching development, as well as (non-)cancerous biliary diseases.

The introduction of cholangiocyte organoids[50] from human adult tissue as described by Huch *et al.*[7] and Sampaziotis *et al.*[9] allowed for long-term culture of cholangiocytes. However, both protocols form organoids consisting of a polarized monolayer of cells with a central cavity, independent of the region from where the organoid-initiating cells were obtained.[7,9] The unique architecture of the BRCOs developed here, provide an opportunity to study tubular formation. We show that the formation of BRCOs is driven by NOTCH signaling and that it follows tip-driven branching and termination dynamics similar to that seen *in vivo*.[51,52] These typical dynamics indicate that tips bifurcate following probabilistic rules, yet arrest their growth in crowded regions, recapitulating aspects of organ development. This makes BRCOs a useful *in vitro* model to study branching morphogenesis in general, as well as biliary development and its associated diseases.

Previous studies show that human cryopreserved IHCs can be cultured in a combination with Matrigel/collagen type 1 and form branched/sprouted networks.[53] However, cells could only be passaged five passages, and no descriptive analysis comparing them to primary tissue were performed. Moreover, no analyses were described to investigate whether the branching mimics aspects of bile duct development. Interestingly, in common with our findings, the authors demonstrate that the addition of EGF (20ng/mL) and NOTCH2 signaling is essential for branching morphogenesis, and highlight the need, for HGF to form branching structures. Currently, HGF is not present in the BRCO-medium. Thus, subsequent experiments could focus on HGF addition to investigate if HGF might increase the branching ability of ICOs. Importantly, BRCOs only develop when cholangiocytes are exposed to both culture conditions in the order described, suggesting that branching *in vitro* can only occur under specific circumstances. During embryonic development the intrahepatic bile ducts develop from a monolayer of progenitor cells, the ductal plate.[21,54,55] Ductal plate-formation is WNT/β-catenin-dependent, but cholangiocyte differentiation and bile duct formation during later stages of embryonic development requires tight β-catenin regulation.[13,14,21]

To grow BRCOs, we start with a monolayer of cells cultured primarily under WNT/β-catenin signaling, as indicated by high expression of *AXIN2 and LGR5* in ICOs. After switching, β-catenin independent WNT signaling is also promoted, as confirmed by high expression of *JUN and JUND*.[56,57] Furthermore, we show that by inhibiting of NOTCH signaling with and without WNT inhibition (Fig. 2I and 6F), BRCOs transform back to cysts. Thus, BRCOs are established by mimicking the activity of different pathways involved in biliary development *in vivo.* Similar approaches could be applied to other organs as well.

Previous studies on cholangiocytes demonstrate that there are subtle, but important, local microenvironment-driven differences between intra- and extrahepatic cholangiocytes.[8,29] Moreover, these cholangiocytes have distinct embryonic origins and have a unique predisposition for cholangiopathies. Interestingly, *JAG1* is only highly expressed in IHCs[29] and is essential for proper tubular development. In line with these results, only ICOs can form BRCOs. Surprisingly, fetal-ICOs did not form tubular structures *in vitro*. *In vivo,* proper IHBD development starts from week 20.[58] The gestational age of the fetal livers used here is between 17-18 weeks, suggesting that the livers might have been too young to demonstrate branching *in vitro.* Alternatively, it could be that fetal-ICOs require additional stimulation or inhibition of pathways to form BRCOs. Importantly, recent transcriptome studies of cholangiocytes demonstrated heterogeneity in the biliary compartment, with a subset of cells expresses high levels of hepatocyte-related genes[13,14,29,31], and might be able to transdifferentiate to hepatocytes.[13,59] Only BRCOs recapitulate this heterogeneity (Fig. 3C, Fig. 4B, and S4C and D)[7,9], making them an exceptionally good model to study cholangiocytes *in vitro.*

WNT signaling pathways are frequently dysregulated in a variety of cancers.[37,60] In a clinical setting, elevated levels of DKK1 are related to lymphatic metastasis and poor prognosis in CCA[61], and a phase II clinical trial with an anti-DKK1 antibody in CCA patients is currently underway[62], showing the importance of the culture conditions described here. BRCCAOs show a unique phenotype, characterized by a dense organization of branch outgrowths and the phenotype is consistent with a model with a hindered capacity to control tip growth or to produce elongated ducts, as also seen *in vivo*.[63] This clear difference in growth patterns was previously not well recapitulated in CCAOs. Moreover, we show that transcriptionally, BRCCAOs are more representative to the *in vivo* patient tumor, while upregulating important tumor-related pathways, showcasing the complex cellular behavior in BRCCAOs. However, considering high inter-tumor heterogeneity present in CCAs *in vivo*[64], it remains a question to what extent BRCCAOs represent this heterogeneity. Thus, extending the scRNA-seq analysis to BRCCAOs could provide more granularity on the transcriptomic changes occurring, and the possible subpopulations that are affected.

Management of CCA is hurdled by the lack of response to treatment[37] and the need for novel therapies is still present as indicated by novel trials.[65,66] Preclinical models that better recapitulate (chemo)resistance, as shown by BRCCAOs, could aid this process. Interestingly, similar to BRCOs, we observed activation of the JNK pathway in BRCCAOs. Integration between JNK and β-catenin regulates cancer development.[67] Furthermore, *JUND* has been shown to mediate JNK-stimulated survival and anti-apoptotic signaling in collaboration with NF-κB[68], another upregulated pathway in BRCCAOs, hinting at a relationship between these important signaling pathways and chemoresistance. Further studies will focus on uncovering the molecular basis for the chemoresistance present in BRCCAOs.

In conclusion, our results indicate that BRCOs represent organoids that recapitulate both the complex morphological architecture as well as the transcriptomic heterogeneity present in human IHBDs. They represent a novel and unique model for studying human bile duct branching development, branching morphogenesis *in vitro*, and (malignant) biliary diseases.

Limitations of the study

BRCOs represent only cholangiocytes and do not contain any other liver cell types. Additional experiments could be performed to create a functional 'epithelial liver organoid' for instance by co-culturing BRCOs with hepatocyte-like cells. In addition, there is no data available of the CCA patients on how they responded to drug treatments as these patients underwent a curative resection. Therefore, a direct comparison of drug response could not be made.

Finally, there is no modelling data available on human IHBD development. Although, we demonstrated that BRCOs have tip-driven branching and they develop according to tubular growth as observed in other branching organs, addition of this data would provide further evidence that BRCOs recapitulate the morphology and growth dynamics as observed *in vivo*.

Author's contribution.
FJMR, GSvT, HW, IB, LV, RB, HM, BDS, MMAV and LJWL were involved in study concept and design. FJMR, GSvT, IB, HW, MvR, DV, JW, OR, GWT, KM, LAM, SN and MdW acquired, analyzed, and interpreted data. JNMIJ, RS and PJF were critical for obtaining materials and material support. HW, DJK, RS, RB, HM and BDS have provided technical support and helped to interpret data=. LJWL, JNMIJ, BDS and MMAV supervised the study. FJMR, GSvT, IB and HW drafted the manuscript, and all authors critically revised the manuscript.

Acknowledgements.
We thank the CASA clinics in Leiden and Rotterdam for collection of fetal tissues and dr. Sari (Erasmus MC) for her help with the Albumin ELISA. We would like thank Marilena Manolika and Remco de Louw (both Erasmus MC) for their help with the electron microscopy imaging and analysis, and dr. Atmodimedjo (Erasmus MC) for performing the genomic sequencing. In addition, we thank Kelly Meijsen (Erasmus MC) for her help with the swelling experiment, Shaojun Shi, Kübra Koten and Ruby Lieshout (all Erasmus MC) for the pathological examination of the primary cholangiocarcinoma tissue, dr. Spee (Utrecht University) for sharing the Rhodamine assay, Naomi Delleman (Erasmus MC) for designing the figures using biorender, staff of prof. dr. Clevers (Hubrecht Institute) for providing the AGS ICOs, and dr. Sampaziotis (University of Cambridge) for his expertise and suggestions for experiments. In addition, the LJWvdL laboratory acknowledges funding from the Dutch Gastroenterology and Hepatology Foundation (MLDS-diagnostiek grant D16-26) and the Medical Delta Regenerative Medicine 4D program. FJMR is partially funded by the Albert Geerts Fellowship (EASL regenerative hepatology consortium). IB and BDS acknowledges support of the UK Engineering and Physical Sciences Research Council (EP/P034616/1). BDS is supported by a Royal Society EP Abraham Research Professorship (RP/R1/180165). Finally, this project was partially funded by the Erasmus MC Human Disease Model Award 2018 (HDMA-380801).

Declaration of interest. The authors declare no competing interests.

Figure 1. Establishment and characterization of branching cholangiocyte organoids.
(a) Schematic overview of BRCO culture. IHCs are obtained from a liver biopsy and cultured as ICOs. After 3 passages, culture conditions are switched and BRCOs are formed. Scale bars indicate 2000µm, unless otherwise stated. **(b)** Growth over (two weeks) time of BRCOs. **(c)** Transmission electron microscopy images of single cells of BRCOs, arrows in the left panel indicate microvilli (left) and a tight junction (right). In the right panel the arrow points to microvilli, scale bars indicate 2 µm (left) and 1 µm (right). **(d)** Max projection of confocal images of BRCOs for KRT 19 and KRT7 (both red), F-actin (green) staining, nuclei are stained with DAPI (blue), scale bar indicates 100 µm. **(e)** qRT-PCR (mean ±SD) for cholangiocyte-, progenitor-related/WNT-target-, and hepatocytes genes in BRCOs and ICOs (donor matched n=3). Values are displayed as fold change compared to ICOs. All experiments in Fig.1C-E are with lines 2-4. Panel B is with BRCO line 1.

Figure 2. BRCOs resemble functional intrahepatic bile ducts *in vitro.*

(a) Max-projection of confocal image of rhodamine-123 (green), and in **(b)** after verapamil addition. Nuclei are stained with DAPI (blue) and scale bars in a and b indicate 100 µm. **(c)** BRCOs at T=0 minutes and T=60 minutes stimulated by secretin and secretin with somatostatin pre-treatment. **(d)** Quantification (mean ±SD) of the swelling assay in **c**. **(e)** Ussing chamber experiment of 2D grown BRCOs. **(f)** ALP activity in BRCOs and ICOs. **(g)** GGT activity (mean ±SD) in BRCOs and ICOs. Experiments a-g are performed on biological triplicates ICOs and BRCOs 3, 4 and 6. **(h)** Bright field images of organoids cultured in BRCO conditions (serving as a control, scale bars indicate 2000 µm) and in **(i)** cultured in hepatocyte-differentiation conditions, scale bars indicate 1000 µm and upon zoom 200µm. **(j)** qRT-PCR (mean ±SEM) of *ALB*, *CYP3A4, HNF4α, MRP2, A1AT* and *LGR5* in BRCOs, ICOs and for both after hepatocyte-differentiation (n=3). **(k)** Human A1AT and Albumin secretion (mean ±SEM) as measured via ELISA in ICOs, BRCOs, for both after hepatocyte-differentiation (n=3), and human serum sample (n=2 technical duplicate, positive control). Experiment h-k are performed on lines 6-8. *indicates significant difference ($p<0.05$).

Figure 3. Single cell transcriptomics demonstrates that BRCOs consist of cholangiocyte-like cells that differ from ICOs.

(a) Schematic overview of the scRNA-seq experiment. Donor matched ICOs and BRCOs (n=3) were treated with Trypsin-EDTA and single calcein^{+} cells were sorted into 384-well plates and sequenced via the CEL-Seq2 protocol. **(b)** Uniform Manifold Approximation and Projection (UMAP) plots of single cells from ICO and BRCO colored by different cell types (left) and by cluster number (right). Cells with similar transcriptome profiles are grouped as clusters. **(c)** UMAP plots showing expression levels of general mature and immature cholangiocyte (organoid) genes (*EPCAM*, *CD24*, *SOX9*, *KRT19*, *KRT7*, *LYZ*, *SPP1*, *MUC5B* and *MUC5AC*) and hepatocyte related genes (*ALB*, *CYP2E1* and *SERPINA1*). **(d)** Violin plots showing the transcription levels of significantly DE cholangiocyte genes from c.

Figure 4. **Transcriptomic heterogeneity in subsets of BRCO cells resembles that of primary cholangiocytes.**

(a) GSEA analysis of BRCO (top row) versus ICO (bottom row) as compared to the lists obtained from Rimland *et al.*[8] of DE genes between primary cholangiocytes and corresponding organoids from the common bile duct (CBD, left), gallbladder bile duct (GBD, middle), and pancreatic bile duct (PancBD, right). Genes were ranked according to expression level in cholangiocytes (left side) and organoids (right side).**(b)** UMAP plot BRCO cells colored by different clusters and the transcription levels of *LGR5*, selected hepatocyte (*GC*, *PCK1*, *ALB*, and *CYP2E1*), and cholangiocyte markers (*TACSTD2*, *CLDN2*, *TFF1* and *TFF3*). **(c)** UMAP plots showing the integration analysis of ICOs, hepatocytes and cholangiocytes. The plot on the left is colored based on cell types, and the one on the right highlights BRCO cells according to the clusters of Fig. 4B. **(d)** PAGA analysis showing the connectivity scores between different cell types, values are multiplied by 100. **(e)** GSEA of BRCO (left) versus ICO (right) as compared to the DE genes between primary cholangiocytes and ICOs from the Aizarani *et al.*[13] dataset. DE genes were ranked according to expression level in cholangiocytes (left) and organoids (right).

Figure 5. **BRCOs grow according to branching and annihilating random walk dynamics with tip maturation.**

Max-projections of confocal images of **(a)** EdU incorporation (green) and **(b)** Ki67 (green) staining. Nuclei are stained with DAPI (blue or grey), scale bars indicate 500μm (a) and 200 μm (b). **(c)** BRCO overlaid with the reconstructed ductal network (gray lines), the source is indicated in blue. **(d)** Duct-length distribution for BRCOs (black, n=3) and model prediction in yellow (R^2=0.96). **(e)** Schematic of the subprocesses in the BARW theory proposed. **(f)** Branching tree representation of the experimental ductal network in (d, left), outlining a subtree and the tip-to-tip path between two nodes (a) and (b) (dashed green), and example of a network obtained from the BARW model (right). **(g)** Schematics for the termination probability (q) and branching probability (1-q). Comparison of experimental measurements and model for **(h)** Termination probability (R^2=0.94), and the cumulative probability for **(i)** subtree persistence (R^2=0.97) and **(j)** sizes (R^2=0. 92). For **(e)** and **(h-j)**, experimental measurements appear in black (error bars correspond to the SD), and results of the model appear in orange (shaded area shows the SD from 1000 realizations). All experiments were performed on BRCO10 and BRCO9 (technical duplicate).

Figure 6. JAG1/NOTCH2 signaling is essential for branching morphogenesis in BRCOs.
(a) Violin plots showing the expression of selected genes involved in the NOTCH pathway for BRCOs (red) and ICOs (green)**. (b)** JAGGED1 protein expression analyzed via Western Blotting in AGS ICOs and healthy ICOs. β-actin was taken along as a loading control. **(c)** Immunofluorescence staining of healthy ICOs (left) and AGS ICOs (right) for JAGGED1 (green), KRT7 (Red) and Nuclei (DAPI, cyan). Scale bars indicate 100 µm and 25 µm upon zoom. **(d)** Percentage of EdU^+ cells (mean ±SD) as analyzed by flow cytometry in healthy ICOs (n=3) and AGS ICOs (n=2, technical replicates). **(e)** Organoids from an AGS patient cultured in ICO (left) and BRCO conditions (right). Scale bars indicate 2000 µm. **(f)** Effect of NOTCH signaling inhibitor DAPT (50 µM) on healthy BRCOs (top), and as a control normal BRCO conditions (bottom). Scale bars indicate 1000 µm. Panel a is created using ICO and BRCO lines 6,7 and 10, all other panels are performed with biological triplicates (ICO12, 15 and 16). *indicates significant difference ($p<0.05$).

Figure 7. Characterization and comparative analysis of BRCCAOs shows improved *in vitro* modelling of CCA.

(a) Representative bright field image of BRCCAOs. **(b)** H&E staining of cross-sectioned BRCCAOs and matched tumor tissue (n=3). **(c)** Max projection of confocal image of EdU (green) incorporation. Nuclei are stained by DAPI (blue). **(d)** 2D-projeced area (left) and circularity (right) of BRCAAOs and BRCOs. **(e)** Volcano scatter plot of statistical significance (adj. p-value) versus Log2FC showing DE genes between CCAOs and BRCCAOs. Positive log2 fold change indicates increased expression in BRCCAOs. Relevant genes are highlighted. **(f)** Pathway analyses of DE genes showing normalized enrichment score significantly upregulated in BRCCAOs (green) or CCAOs (red). **(g)** Correlation matrix of transcriptomic profiles of matched tumor tissue (CCAT), BRCCAOs and CCAOs. A value of 1 represents complete correlation, and a value of 0 represents no significant correlation. **(h)** Dose-response curves after 72h treatment with gemcitabine and cisplatin. Biological replicates are plotted separately. All scale bars indicate 200 µm. All experiments were performed with 3 pairs of BRCCAOs and CCAOs and performed in duplicate.

Star Material and Methods

DATA AND CODE AVAILABILITY

The scRNA-seq data (BRCOs and ICOs) and the bulk RNA-seq data (CCAs, CCAOs and BRCCAOs) are deposited in the GEO repository (GSE179601) and are publicly available as of the date of publication. In addition, the mass spectrometry proteomics data (ICOs and BRCOs) have been deposited to the ProteomeXchange Consortium via the PRIDE partner repository[69] with the dataset PXD028532 and DOI: 10.6019/PXD028532 and will be available at the date of publication. Original western blot images have been deposited at Mendeley and will be publicly available at the date of publication. The DOI is listed in the key resources table. The source code from the BARW model and analysis is available upon request to the corresponding author. Microscopy data reported in this paper will be shared by the lead contact upon reasonable request.

ProteomeXchange login for reviewers:
Username: reviewer_pxd028532@ebi.ac.uk
Password: PhjENkLb

CONTACT FOR REAGENT AND RESOURCE SHARING

Further information and requests for resources and reagents should be directed to and will be fulfilled by the lead contact, Prof. dr. LJW van der Laan (l.vanderlaan@erasmusmc.nl).

EXPERIMENTAL MODEL AND SUBJECT DETAILS

Cell lines

L-Wnt3a, 293T-HA-Rspo1-Fc and Noggin HEK-293 cell lines were used as described to generate conditioned media for organoid culture (secreting WNT3A, R-Spondin and Noggin). Cells were cultured in a humidified 5% CO_2 atmosphere at 37°C as previously described.[70,71]

METHOD DETAILS

Tissue and tumor collection

Tissue biopsies from liver (circa 0.5-3 cm^3, n=16) and extrahepatic bile duct (EHBD, circa 0.5-3 cm^3, n=3) were obtained from donor livers (n=14) or explant livers (n=2) during liver transplant procedures (for details see Table S1) performed at the Erasmus MC, Rotterdam, the Netherlands. The use of tissue biopsies and livers deemed unsuitable for transplantation was approved by the MEC of the Erasmus MC, (MEC-2012-090, MEC-2014-060). Fetal liver samples (n=3) were collected via the CASA clinic in Leiden and Rotterdam and the use of fetal tissues was approved by the MEC of the Erasmus MC (MEC-2006-202). Additionally, cholangiocarcinoma (CCA) tumor tissue biopsies (n=3) from both perihilar and intrahepatic CCA (see Table S1) were obtained through liver resections performed at the Erasmus MC (MEC-2013-143). Biopsies were stored at 4˚C in University of Wisconsin (UW, Bridge to Life Ltd. Belzer Cold Storage Solution) preservation solution during transport. For a complete overview of characteristics of patients or donors from whom biopsies were obtained, please see Table S1. All patients or their next of kin gave written informed consent to use their tissue.

Generation and culture of (tumor) organoids

Organoids from (adult and fetal) liver (IHBD)[7]- and adult EHBD[11] biopsies were processed, initiated, and expanded in the culture conditions as previously published.[70] Biopsies were digested by incubation with 4 mL collagenase digestion solution (2.5 mg/mL collagenase A1, Sigma) in Earle's Balanced Salt Solution (EBSS, Hyclone, ThermoFisher scientific) for 30 min at 37°C. Digestion solution was diluted by adding cold Advanced (Adv)DMEM/F12 (GIBCO, supplemented with 100 µg/mL penicillin/streptomycin, Fisher Scientific; HEPES 1M, Fisher Scientific; 1% Ultraglutamine 200mM, Fisher Scientific and Primocin, Invivogen) and centrifuged for 5 minutes, 4˚C at 453g. The cell suspension was filtered through a 70 µm Nylon cell strainer and centrifuged for 5 minutes, 4˚C at 453g. Supernatant was removed and the cell pellet was suspended in cold (4°C) or 25µL Basement Membrane Extract (BME, Cultrex) diluted with 30% of AdvDMEM/F12 which was allowed to solidify for 30-45 minutes at 37°C before 250µL start-up expansion medium (SEM) was added.[70] SEM consists of supplemented AdvDMEM/F12 (GIBCO, supplemented with 100 µg/mL penicillin/streptomycin, Life Technologies; HEPES 1M, Fisher Scientific; 1% Ultraglutamine 200mM, Fisher Scientific and Primocin, Invivogen) supplemented with 1% N2 (GIBCO) and 1% B27 (GIBCO), 1.25 mM N-Acetylcysteine (Sigma), 10 nM gastrin (Sigma), 50 ng/mL EGF (Peprotech), 10% RSPO1 conditioned media (homemade), 10% Noggin conditioned media (homemade), 30% WNT conditioned media (homemade), 10 µM (Y27632, Bioconnect), 10 µM hES cell cloning recovery solution (Tebu-bio), 100 ng/mL FGF10 (Peprotech), 25 ng/mL HGF (Tebu-bio), 10 mM Nicotinamide (Sigma), 5 µM A83.01 (Sanbio), and 10 µM Forskolin (Sigma). SEM was replaced with canonical-WNT stimulating expansion medium (EM), consisting of the same components without NOGGIN, WNT, Y27632, and hES cell cloning recovery solution, after three days.[70] Finally, branching organoids were created by switching culture conditions to non-canonical WNT stimulating conditions, consisting of William's E medium (WE, ThermoFisher Scientific) supplemented with 10 mM nicotinamide (Sigma), 17 mM sodium bicarbonate (Sigma), 0.2 mM 2-phospho-L-ascorbic acid trisodium salt (Sigma), 6.3 mM sodium pyruvate (Gibco), 14 mM glucose (Sigma), 20 mM HEPES (Fisher Scientific), ITS + premix (Life Technologies), 0.1 µM dexamethasone (Sigma), 2 mM Ultraglutamine (Fisher Scientific), 100 µg/mL penicillin/streptomycin

(Fisher Scientific), 20 ng/mL EGF (Peprotech), 10% RSPO1 conditioned media (homemade) and 100 ng/mL DKK-1 (Abcam Ltd), after 3 passages.[9,12]

Cholangiocarcinoma organoids (CCAOs) were initiated and expanded as previously described.[20] Processing and initiation of these organoids was similar to ICO counterparts described above, except tissue digestion was extended to 2 hours for tumor tissue that, after visual inspection, still had relatively large undigested tissue fragments left. BRCCAOs were created by switching culture medium to non-canonical WNT stimulating conditions after a minimum of 3 passages in expansion medium.

Time-lapse bright field microscopy

BRCOs (n=3, multiple wells over time) were cultured in glass bottom 96 well plates (SensoPlate™ 24 well, Greiner Bio-One) and imaged using bright field microscopy using an Opera Phenix system (PerkinElmer), equipped with a 10x air objective (NA 0.3), in non-confocal modus. Every 30 minutes, for 110 hours, a small z-stack was acquired to ensure optimal optical focus in several points of the growing organoid. The images were concatenated to create a time-lapse and observe growth of the organoids. Additional time-lapse analysis was performed with the addition of A83-01 (1µM) to inhibit the transforming growth factor beta (TGF-β) pathway, known to be involved in branching morphogenesis.[6]

Transmission Electron Microscopy (TEM)

To perform TEM, BRCOs were fixated in 1.6% glutaraldehyde and were stored at 4°C until processed. Subsequently, post fixation was performed using 1% osmium tetroxide for one hour. Next, acetone rinses were performed (8 times 15 minutes with increased percentage of acetone) and samples were infiltrated with 1:1 100% acetone:epoxy embedding medium for two days. First, they were embedded for one hour at room temperature, followed by an embedding at 40°C overnight, and finally a 24-hour step of embedding at 60°C. Subsequently, ultrathin sections of 60 a 70 nm were created at a 6-degree angle at speed of 1 mm/s with a Diatome diamond knife and an electronic microscope ultra-microtome (Leica UC7). Finally, ultrathin sections were imaged using a FEI Talos transmission electron microscope (Thermo Scientific), equipped with a 4K CMOS camera; samples were imaged using 80 kV.

Hematoxylin and Eosin (H&E) and Immunofluorescence (IF) staining

Organoids were fixed for 10 minutes using 4% paraformaldehyde removing the hydrogel. While primary CCA tissue was fixated overnight using 4% paraformaldehyde. Samples were paraffin embedded and cut as 4 µm thick slides. Subsequently, H&E staining was performed according to standard protocols. H&E-stained slides were imaged with Zeiss Axiokop 20 microscope and captured with a Nikon DS-U1 camera. If immunofluorescence was performed, slides were permeabilized with 0.1% Triton X-100 diluted in phosphate buffered saline (PBS) for 15 minutes. Subsequently, they were exposed to 10% goat serum diluted in 1% Bovine Serum Albumin (BSA)-PBS to prevent nonspecific antibody binding. Primary antibodies were added to the organoids and incubated overnight at 4°C. Finally, incubation with the secondary antibody took place for 60 minutes at room temperature and cell nuclei were stained with DAPI (Vectashield, Vectorlabs). Analysis took place on a SP5 confocal microscope (LEICA) equipped with a 405, 488 and 561 nm laser. Images were analyzed using ImageJ (version 1.52p, supplemented with FIJI).

Whole mount confocal IF staining

To evaluate protein expression of organoids, IF was performed using whole mount confocal microscopy with selected antibodies. In short, organoids were fixed for 10 minutes using 4% paraformaldehyde removing the hydrogel. Next, they were permeabilized with 0.1% Triton X-100 diluted in PBS for 15 minutes. Subsequently, they were exposed to 10% serum diluted in 1% BSA-PBS to prevent nonspecific antibody binding. Primary antibodies were added to the organoids and incubated overnight at 4˚C. Incubation with the secondary antibody took place for 60 minutes at room temperature. Additional cytoskeletal staining with Phalloidin Alexa Fluor™ 488 (1:200, ThermoFisher) and nuclear staining with DAPI was performed. Samples were imaged using a Leica 20X water dipping lens on Leica DM6000 CFS microscope with a LEICA TCS SP5 II confocal system or an Opera Phenix HCS system (PerkinElmer) equipped with a 20x air objective (NA 0.4) and 40x water immersion objective (NA 1.1). For detection on the Opera Phenix system, DAPI was excited with a 405 nm solid state laser and detected at 435-480 nm. EdU incorporation, Phalloidin Alexa Fluor 488, and the Ki67 immune labeling were excited at 488 and 561 nm and detected at 500-550 nm and 570-630 nm, respectively. Images were exported and further processed using ImageJ (version 1.52p, with FIJI).

Stable Isotope labeling by amino acids in cell culture (SILAC) sample preparation

ICOs and BRCOs (n=3) were cultured in the organoid SILAC media for 25 days**.** Both ICOs and BRCOs were cultured as normal, but for ICOs regular AdvDMEM/F12 was replaced with SILAC Advanced DMEM/F-12 Flex media (ThermoFisher) and for BRCOs, William's E Medium was replaced with SILAC William's E Medium (AthenaES). All culture medium contained arginine and lysine, either with the normal light isotopes of carbon, hydrogen and nitrogen (i.e.$^{12}C^{14}N$, Light), or with medium containing L-arginine-$^{13}C_6$-$^{15}N_4$ and L-lysine-$^{13}C_6$-$^{15}N_2$ (Heavy). All organoids were maintained in SILAC conditions (light or heavy media) for at least two passages, to allow SILAC isotope incorporation. Subsequently, they were analyzed by mass spectrometry to estimate incorporation by using BME light/organoid heavy ratios. To do so, lyophilized samples were rehydrated in 200 µL extraction buffer with 100 mM ammonium bicarbonate with 8 M urea, and homogenized using a Bioruptor®Plus (Diagenode SA, Seraing, Belgium) at 4°C for 20 cycles, 15 s ON/OFF. Samples were centrifuged (14000 g, 15 min) and the protein content of supernatants was determined using Pierce BCA Protein Assay Kit (Thermo Scientific, Waltham, MA, USA). 30 µg of protein was processed further by reduction with 5 mM tris-2-carboxyethyl phosphine for 30 min at 37°C, alkylated with 10 mM iodoacetamide for 45 min at room temperature, followed by overnight trypsin digestion at 37°C. Digestion was stopped by addition of formic acid (FA) to a pH < 3. Samples were desalted using C18 reversed-phase spin columns (Harvard Apparatus, Holliston, MA, USA) according to manufacturer's instructions. After desalting, samples were resuspended in 2% acetonitrile (ACN), 0.1% FA and the peptide concentrations were determined using a NanoDrop 2000c Spectrophotometer (Thermo Scientific).

Liquid chromatography (LC)–mass spectrometry (MS)/MS analysis

The LC MS/MS analysis was performed on Tribrid mass spectrometer Orbitrap Fusion equipped with a Nanospray source and coupled with an EASY-nLC 1000 ultrahigh pressure liquid chromatography (UHPLC)

pump (ThermoFisher Scientific, San Jose, CA). One microgram of peptides was loaded and concentrated on an Acclaim PepMap 100 C18 precolumn (75 µm x 2 cm, ThermoFisher Scientific, Waltham, MA) and then separated on an Acclaim PepMap RSLC column (75 µm x 25 cm, nanoViper, C18, 2 µm, 100 Å) with the column temperature of 45°C. Peptides were eluted by a nonlinear 2h gradient at the flow rate of 300 nL/min from 2% solvent B (0.1% FA/ACN, Merck)/98% Solvent A (0.1% FA in water, Merck) to 40% solvent B. The Orbitrap Fusion was operated in the positive data-dependent acquisition (DDA) mode. Full MS survey scans from m/z 375-1500 with a resolution 120,000 were performed in the Orbitrap detector. The automatic gain control (AGC) target was set to 4 × 105 with an injection time of 50 ms. The most intense ions (up to 20) with charge states 2-7 from the full MS scan were selected for fragmentation. MS2 precursors were isolated with a quadrupole mass filter set to a width of 1.2 m/z. Precursors were fragmented by Higher Energy Collision Dissociation (HCD) and detected in Orbitrap detectors with a resolution of 30,000. The normalized collision energy (NCE) in HCD cells was set at 30%. The values for the AGC target and injection time were 5 × 104 and 54 ms, respectively. The duration of dynamic exclusion was set at 45s and the mass tolerance window at 10 ppm.

SILAC Data analysis

Analysis of raw files was performed with MaxQuant (version 1.6.17.0). The resulting peak lists were searched in Andromeda against a reviewed human UniProtKB database (release 2021_02), complemented with the standard MaxQuant contaminant database. Enzyme specificity was set to trypsin/P with a maximum of two missed cleavages. Precursor mass tolerance was set to 4.5 ppm and fragment ion mass tolerance to 20 ppm. Carbamidomethylation of cysteine was used as fixed modification and deamidation (Asparagine and Glutamine), oxidation (Methionine, Proline) and acetylation were considered as variable modifications. The false discovery rate (FDR) was set to 0.01 for both peptides and proteins. The “match between runs” option was enabled with default settings to match identifications across samples. The mass spectrometry proteomics data have been deposited to the ProteomeXchange Consortium via the PRIDE partner repository[69] with the dataset identifier PXD028532 and DOI:10.6019/PXD028532.

RNA extraction, cDNA synthesis and RT-qPCR

Total RNA was collected after removal of the culture medium by adding 700µL of QIAzol lysis reagent (Qiagen) to a 24 well containing organoids (two 25µL BME domes). RNA was isolated using the miRNeasy kit (Qiagen) according to the manufacturer’s protocol[72] and the concentration was measured using a NANOdrop 2000 (ThermoFisher). cDNA from 500ng RNA was prepared using 5x PrimeScript RT Master Mix in a 2720 thermal cycler (Applied Biosystems). RT-qPCRs were conducted on an Applied Biosystems StepONE Plus Real-Time PCR machine (Applied Biosystems), according to the manufacturer's guidelines, with 45 cycles of amplification. Reactions consist of 10 µL SYBR™ Green PCR Master Mix (Thermofisher Scientific), 1 µL of primers (Applied Biosystems/Life Technologies), 4 µL sterile milliQ water, and 5 µL of diluted cDNA. Threshold levels were manually set at 0.25 for all miRNA assays, and the upper Cq limit for reliable detection was set at 35 cycles. RT-qPCR was performed with the primer sets provided in Table S2. All RT-qPCR data are presented as mean with a 95% confidence interval. RT-qPCR values are relative to the housekeeping gene Hypoxanthine-guanine-fosforibosyl-transferase *(HPRT)* or Glyceraldehyde 3-phosphate dehydrogenase *(GAPDH)*.

(Trans)differentiation towards hepatocytes

BRCOs and matching ICOs (from the same patient, n=3 individual patients) were differentiated towards hepatocytes. The hepatocyte differentiation protocol used was adapted from Huch *et al.* with slight modifications (Clevers *et al.* patent: WO2017149025A1)[73], as published by Verstegen *et al.*[11] Medium consisted of 5 days of EM supplemented with BMP7 (Peprotech, 25 ng/mL) for ICOs and 5 days of non-canonical WNT stimulating conditions supplemented with BMP7 (25 ng/mL) for BRCOs. Then, the cultures were passaged and medium was changed to the differentiation medium (DM): AdvDMEM/F12 medium supplemented with 1% N2 and 1% B27 and containing EGF (50 ng/mL), gastrin (10 nM), HGF (25 ng/mL), FGF10 (100 ng/mL), A83-01 (5 µM), DAPT (10 µM), BMP7 (25 ng/mL), iCRT3 (Sigma, 25µM, iWP2 (Sanbio, 3 µM), Carbachol (Sigma, 100µM), CHIR99021 (Sigma, 3µM), and dexamethasone (30 µM). Differentiation medium was changed every 3-4 days and the total differentiation protocol took 14 days (including pre-treatment with BMP7). Differentiation was accessed by gene expression analysis of genes associated with hepatocyte maturation (Albumin –*ALB*-, *HNF4α*, CYP3A4, *MRP2* and alpha-1-anti trypsin –*SERPINA1*-) and stemness/WNT-target gene (*LGR5*) by RT-qPCR, and ELISA for A1AT (AssayMax™ Human alpha-1-Antitrypsin kit, AssayPro) and Albumin. A1AT ELISA was performed on supernatant of the organoids (n=3, all conditions) according to the manufacturer's instructions. The assay was performed in duplo, and the readout was done on a microplate reader at a wavelength of 450 nm (CytoFluor series 4000, Applied Biosystems). Furthermore, hepatocyte function was assessed using a human albumin ELISA as previously described (Bethyl laboratories, Montgomery, TX, USA).[74] First, plates were coated with a Human Albumin antibody (ThermoFisher, A80-229A 1:200) and incubated for 1 hour at room temperature, afterwards plates were washed. Subsequently, blocking was performed using 1% BSA-PBS for 30 minutes and samples were incubated for 1 hour at room temperature. Reaction was detected by adding a detection antibody (ThermoFisher, A80-129P, 1:10000) for 1 hour at room temperature and plates were washed extensively afterwards. TMB substrate (ThermoFisher) was added and after turning blue the reaction was halted by stopping buffer (1M Sulfuric Acid, Sigma) addition. All measurements were performed in duplo and human serum (Bethyl, 1:200 diluted) was taken along as a positive control. Readout was performed on a microplate reader at a wavelength of 450 nm (CytoFluor series 4000, Applied Biosystems).

Gamma-Glutamyltransferase (GGT) functionality

Supernatant (10µL) of BRCOs (n=3) and ICOs (n=3) was collected. Activity was determined using a colorimetric assay kit (MAK089; Sigma-Aldrich), freshly made medium was used as a negative control. The equivalent serum GGT activity in IU/L was calculated following the manufacturer's instructions by multiplying the average increase in absorbance over 30 minutes.

Alkaline Phosphatase functionality

ALP staining was carried out on BRCOs and ICOs (both, n=3) using the 5-bromo-4-chloro-3-indolyl-phosphate/nitro blue tetrazolium (BCIP/NBT, Promega) color development substrate. 5 mL of WE were mixed with 33µl of NBT and subsequently with 16.5µl of BCIP. 500µL of substrate mix was added to each well (24 well plate) and readout was performed after 30 minutes.

Rhodamine-123 transport functionality

Functionality of the Multi Drug Resistance (MDR)-1 transporter was assessed using the Rhodamine-123 assay.[10] Specificity was determined by blocking MDR-1 transporter with Verapamil (10 µM, Sigma Aldrich) for 30 min at 37˚C prior to Rhodamine-123 incubation (100 µM, Sigma Aldrich). Subsequently nuclei were counterstained by Hoechst 33342 (Sigma) and confocal images were acquired using a Leica SP5 confocal microscope (LEICA) equipped with a 405 and 488 nm laser.

Secretin, somatostatin and cholangiocyte ion-channel functionality

To assess functionality of secretin and somatostatin, a slight modification of the Forskolin-Induced Swelling (FIS) assay as developed by Dekkers *et al.*[75] for testing cystic fibrosis transmembrane conductance regulator (CFTR) was applied. For this, BRCOs and ICOs were incubated for 30 min with 3 µM calcein-green (Sigma), stimulated with secretin (10 µM) or secretin and somatostatin (100 µM) and analyzed by confocal live cell microscopy at 37˚C for 120 min (LSM710, Zeiss). The total or single organoid area (XY plane) increase relative to t=0 of secretin treatment was quantified using velocity imaging software (Improvision) and compared to non-stimulated controls. Cell debris and unviable structures were manually excluded from image analysis. To further confirm CFTR-functionality we performed an ussing chamber assay as previously published.[76] BRCOs were seeded on a transwell culture plate (24 well plate 6.5mm, Corning) to grow them in a 2D fashion. Prior to seeding of the cells, transwell inserts were coated with 5% matrigel (Corning) in PBS for 2 hours. Fully expanded domes of organoids were collected in WE and centrifuged (453*g*, 5 min, 4˚C). After removal of the supernatant, organoids were mechanically broken by vigorously up and down pipetting. The organoid suspension was spun down again, and the cell pellet was made single cell by digestion in Trypsin-EDTA (TE) for 25 to 40 min at 37°C. Cells were washed in WE and sieved through a cell 70 µm cell strainer. Approximately $3x10^5$ cells were suspended in 200 µL WE with components medium and seeded on transwell inserts. Medium was changed every 3-4 days. To check confluence, the cells were examined by daily microscopy and electrophysiological analysis was performed after 4 days. Upon forming a confluent monolayer, transwells were placed in an Ussing chamber (Physiologic instruments) set up to analyze functional cholangiocyte-specific transporter channels (CFTR and Ca^{2+}-activated Cl^- channel) using Acquire & Analyze Software 2.3 (Physiologic Instruments, San Diego, California). The temperature of the chambers was kept at 37°C by warm water bath circulation and chambers were gassed with 95%O_2, 5%CO_2. Each chamber consisted of 3mL modified Meyler solution (128 mmol/liter NaCl, 4.7 mmol/liter KCl, 1.3 mmol/liter $CaCl_2$, 1.0 mmol/liter $MgCl_2$, 0.3 mmol/liter Na_2HPO_4, 0.4 mmol/liter NaH_2PO_4, 20 mmol/liter $NaHCO_3$, 10 mmol/liter HEPES, supplemented with glucose (10 mmol/liter) at pH 7.3). Current was clamped and every second short circuit current (Isc) was recorded. CFTR-dependent anion secretion was activated by adding Forskolin (3µL, 10mM) to both sides of the cells, and GlyH-101 (3µL, 20mM, apical). Calcium (Ca^{2+}) activated chloride (Cl-) channels (CaCC) were stimulated by UTP (3µL, 50mM, apical) and inhibited by T16Ainhibitor-A01 (3µL, 50mM, apical). The Isc measurements are presented as µA/cm^2. Data was visualized using Excel (Microsoft).

Cell proliferation assessment

Cell proliferation was determined using 5-Ethynyl-2'-deoxyuridine (EdU)-incorporation (ThermoFisher), performed according to the manufacturer's protocol. In short: EdU (10µM) was added to the medium and incubated for 4 hours at 37˚C degrees. BRCOs, ICOs, CCAOs and BRCCAOs were dissociated into single cell suspension via Trypsin-EDTA and suspended in 200µL of 1%BSA-PBS to be analyzed by flow cytometry according to protocol (Canto flow cytometer, BD Biosciences). The gating strategy was performed as previously published.[77] In short gating was based on forward scatter (FSC) and sideward scatter (SSC). Doublets were gated out via a single cell gate (height vs. width). EdU positivity gate was based on the background expression of FITC in organoids without EdU incorporation. Subset analysis was done using Flowjo (version v10.6.1, BD) analysis software. To determine the location of the proliferative cells in BRCOs and CCAOs, EdU incorporation was performed on fixated cells (as previously described for IF staining) by adding EdU (10µM) to the medium. Next click-it labeling was performed according to the manufacturer's instructions. Subsequently nuclei were counterstained by DAPI and confocal images were acquired using the Opera Phenix system (PerkinElmer).

Preparation of single-cell suspensions and FACS

Organoids (ICO and BRCO lines 6, 7 and 10) were incubated with Calcein for 45 min at 37^{o}C before dissociation for live staining of the cells. To get single cells, organoids were then dissociated and digested by 0.05% Trypsin-EDTA following the online protocol.[78] Single-cells were obtained using the flow cytometer FACS Aria (BD Biosciences) equipped with a 130 µm nozzle. Only GFP positive cells (living cells) were sorted into 384-well plates containing a unique CEL-seq primer and 5 µL mineral oil (Sigma, M5310) per well. Plates were stored at -80 ^{o}C until they were processed.

Single-cell RNA library preparation

Single-cell RNA libraries were prepared according to the mCEL-seq2 protocol.[23] Briefly, plates were thawed on ice, and then 100 nL lysis buffer (0.2% Triton X-100, 2mM dNTPs, 1:50.000 ERCC ExFold RNA spike-in (Thermo, 4456739)) was dispensed per well using the Nanodrop Ns-2 Stage (BioNex). SuperScript™ II Reverse Transcriptase (Invitrogen, 18064-14) was used in reverse transcription reaction mix following the protocol, 4 ^{o}C for 5 min; 25 ^{o}C for 10 min; 42 ^{o}C for 60 min; 70 ^{o}C for 10 min. 960 nL second-strand reaction mix containing *E. coli* DNA ligase (NEB, M0205L), *E. coli* DNA polymerase I (NEB, M0209L) and Random hexamer (sigma, 11034731001) were used per well for second-strand synthesis with the following protocol, 16°C for 2 hours. Next, cDNA from one 384-well plate was pooled, and *in vitro* transcription was performed using the MEGAscript™ T7 Transcription Kit (Invitrogen, AMB 1334-5) by incubating the reaction at 37°C for 14 hours. Afterwards, the amplified RNA was fragmented and cDNA was converted using Superscript II and the random octamer primer. Libraries were amplified for 9 cycles using Phusion® High-Fidelity PCR Master Mix (NEB, M0531S) with the Nextflex primers, and quantified on the bio-analyzer using DNA high-sensitivity kit. Barcoded libraries were sequenced on an Illumina NextSeq 500 with 42+38bp paired-end reads at a depth of 24.2-32 million reads per plate.

Single-cell RNA-seq data analysis

Left read of paired-end reads contains the barcode information with 1-8bp to be the unique molecular identifier (UMI), 9-16bp to be the cell barcodes followed by polyT stretch. Barcode information from left reads were first extracted and added to the corresponding right reads using extract function from UMI-

tools 1.0.0.[79] Right reads of read pairs were aligned to an artificial human genome (hg38) containing sequences of 92 ERCC spike-ins using STAR-2.7.0f[80] with default settings. Aligned reads were assigned to genes using featureCount 1.6.4[81] with the following parameter, -g gene_id. For each cell, the number of UMIs per gene was counted and the gene-cell matrixes were generated using count function from UMI-tools 1.0.0 with the following settings, --per-gene, --per-cell. For the downstream analysis, gene-cell matrixes were merged per donor and imported into R. Seurat 3.0[82] was used for data filtering, normalization, scaling, clustering, marker identification and visualization following the standard process. Briefly, Seurat objects were generated from the combined gene-cell matrixes per donor and cells that are not with the following criteria (1000< UMIs < 25000, mt%<50%) were filtered out. Then, UMIs were log normalized, and number of total UMIs and mitochondrial gene expression were regressed out during the data scaling. Seurat objects of different donors were integrated using the functions FindIntegrationAnchors and IntegrateData from Seurat to minimize the biological effects. Differentially expressed genes from each cluster were identified using a Wilcoxon Rank Sum test with a cut-off of adj-P <0.05, ending up with 476 DE genes. Cell cycling prediction analysis was performed using CellCycleScoring function in Seurat.[82] Pathway analysis was performed using Enrichr web tool[83] with the significantly differentially expressed genes as input. The R package fgsea 23 (1.12.0)[84] was used for GSEA. Genes upregulated in either BRCOs or ICOs were used as input, and then compared to the differentially expressed gene set published by Rimland *et al.*[8] (tissue vs. organoids of the common bile duct, gallbladder bile duct, and pancreatic bile duct) and ICOs vs. tissue from the Aizarani *et al.*[13] dataset. An enrichment score normalized to the mean enrichment of random samples with the same size (NES) was calculated, and adj-p<0.05 generated from the Benjamini-Hochberg method was applied as a threshold of significance. In addition, the previous published datasets by both Sampaziotis *et al.*[29] (ArrayExpress: E-MTAB-8495) and Aizarani *et al*.[13] (GEO accession number: GSE124395) were integrated within our own dataset using Seurat integration[79] and analyzed as previously described. For the connectivity analysis, PAGA from Scanpy was applied following the default settings.[85]

Organoid clearing and imaging

Small blocks of agarose were fixed and stained using DAPI (Vectashield). After staining, organoids were optically cleared using a previously established protocol.[86] Organoids in low melting point agarose were firstly put in 50% PBS and 50% methanol for 30 minutes. Subsequently, they were put in 100% methanol overnight and treated with 50% 1:2 benzyl alcohol/benzyl benzoate (BABB) and 50% methanol for 30 minutes. Finally, clearing was completed by putting the organoids in 100% BABB and storing them at 4°C until imaging. For imaging, organoids are placed in a 24 well glass bottom imaging plate (SensoPlate™ 24 well, Greiner Bio-One). Complete organoids were imaged in 3D using the Opera Phenix HCS system (Perkin Elmer) in confocal modus (spinning disk) equipped with two sCMOS cameras. After a pre-scan (5x objective) to select the area of interest, the organoids were imaged with a 20x air objective (NA 0.4, field of view is 421394 μm^2). Nuclear DAPI was excited with a 405 nm solid state laser and detected using a 435-480 band pass filter. The large Z-stacks with a step-size of 3.6 µm (optimal for these optics), ranging from below to above the organoid of interest was tiled to cover the predetermined area of interest. Individual images were exported as TIFF files and subsequently reconstructed.

Segmentation of the ductal network

The ductal networks of (n=3) BRCOs were reconstructed manually using a purpose-built graphical user interface (GUI) (implemented in MATLAB R2020a, The MathWorks, Inc., Natick, Massachusetts, USA). This GUI allowed us to locate and mark the lumen of ducts as well as bifurcation events in medium sized organoids, resulting in a three-dimensional reconstruction of the ductal networks (see Figures 5C and S5D). In general, when working with *in vivo* or *ex vivo* tissues, it is easy to recognize the main duct of a branching tissue, this corresponds to the duct that connects the whole ductal tree to the exterior of the organ, as is the case of the common bile duct in the biliary tree. The main duct represents the root of a branching tree and can be used as a reference to extract its structural and topological features. A challenge of working with *in vitro* cultures, such as BRCOs, was that there is no notion of a main duct that could be used as the root. We could, in principle, define the root as the initial duct, from which the whole tree nucleated. Unfortunately, it was impractical to track this location from when the organoids were seeded to when they were imaged, thus the root location was inferred from the data. As organoids were cultured in 3D conditions and grew in a uniform and isotropic fashion, we defined the location of the root around the geometric center of the organoids (see blue marker in Figs. 5C and S5D). The statistical properties of the branching trees were observed to vary slightly with different choices of the location of the root around the geometric center of the BRCOs.

Construction of the branching tree

To analyze the structure and topology of branching trees, we focused on the sequence of branching and termination events within the tree. For this, we reduced the ductal reconstruction towards an effective branching tree network, where nodes in the tree represent either branching events (nodes with degree 3) or end-points (nodes with degree 1, see Figs. 5H), where the node degree corresponds to the number of edges (ducts) that span from a given node.

End-to-end-point distance distribution

The distribution of distances between all nodes in a complex network relates to the network spectrum and provides a topological measure that is independent of the existence of a root node. Inspired by this, we measured the distribution of distances between every pair of end-nodes in the ductal tree. This distance was measured in units of tree levels, i.e., the distance measures the number of ducts that separate both end-points.

Termination probability

A branching tree can be characterized by hanging it from its root (see construction of branching network, and Figs. 5F and S5F). After defining the root as level zero (level i=0), every branching node and end-node can be identified by its level (or distance) from the root node. To measure the termination probability (q_i) as a function of the level (i) we then measured, for every level, the fraction of the total number of nodes in that level that correspond to end-nodes (nodes of degree 1) (Fig. 5G-H). A value of $q_i<1/2$ indicates a net expansion of the tree, as bifurcations are more likely than end-points. Conversely, $q_i>1/2$ translates to a contraction of the tree, with a larger proportion of end-nodes, while $q_i=1/2$defines a critical regime, where branching and termination events are balanced. It was previously observed that a stochastic branching and terminating dynamics of tip-drive growth self-organizes, in the long term, into a balanced regime ($q_i=1/2$), where active tips form a propagating front at the periphery of the expanding tissue.[30]

Thus, the existence of a plateau around q_i=1/2, is a good indication of an underlying stochastic dynamics of growth (see Fig. 5H).

Subtree size and persistence

A subtree was defined as a subset of the whole tree that has a sub-root (or common ancestor) at a level greater than zero (i>0). To measure the subtree size and persistence (Fig. 5I-J), we considered only subtrees whose common ancestor lied in generation i=4 (see example in Fig. 5F). The subtree size corresponded to the total number of ducts in a given subtree, while the subtree persistence measured the number of levels spanned by the subtree. This choice for the pruning generation (i=4) was arbitrary, but kept fixed when analyzing both experimental networks and numerical simulations, in order to make their results comparable.

Projected area and circularity

For BRCCAOs, reconstruction of the full ductal network was infeasible due to the lack of a well-defined internal ductal structure. To compare BRCCAOs to BRCOs and also to the model proposed, we quantified their 2D-projected area and circularity. This was done by analyzing bright field images of BRCCAOs (n=21) and BRCOs (n=24) after 7-8 days of culture. The outline of the organoids was traced manually, and their total area (*A*) and perimeter (*P*) measured (see Fig. 7D). It is worth noting that because organoids tend to grow radially in every direction, the projected area may be used to estimate their volume. To assess the organoid morphology, we measured the circularity of their projected area, defined as the ratio $4\pi A/P^2$ (see Fig. 7D). This measure, sometimes referred to as compactness, is independent of the sizes of the organoids, and takes a maximum value of 1 when the object is a perfect circle, and approaches zero as the outline of the objects get rougher. Organoids with lower values of circularity are characterized by having more and longer ductal outgrowths, while organoids with circularity closer to 1 have a more compact, spheroidal shape.

Model of branching and termination dynamics

To model the growth dynamics of branching organoids, we use a variant of the Branching and Annihilating Random Walk (BARW) model previously proposed to describe the process of branching morphogenesis in the mouse mammary gland and kidney ductal epithelium.[30] Active tips are modeled as particles that perform a persistent random walk, leaving behind a trail along the traversed path corresponding to the ductal structure of the network. Active tips are subject to Possonian branching events, i.e., branching occurs at a constant rate such that the timing between consecutive branching events is random and statistically uncorrelated characterized by an exponential distribution. As the time between consecutive branching events is directly proportional to the length of the ducts, this model also predicts an exponential distribution of duct lengths. However, experimental observation showed that short ducts were less abundant than expected from a purely exponential distribution (see Fig. 5D), suggesting the existence of a short-term memory in the branching dynamics that prevents a tip from undergoing two consecutive rounds of branching in a very short period of time. This was accounted for in the model by introducing a refractory period τ measured from the time of the last branching event which prevented a tip from terminating or undergoing another round of branching before the refractory period had elapsed. A Poisson branching process with a refractory time is known as a *renewal process*, where for a single tip,

the time between events (waiting times, τ) follows the relation $p_\tau(\tau) = \Theta(\tau - \tau_0)se^{-s(\tau-\tau_0)}$where s is the branching rate, and $\tau_0$the refractory period. The step-function $\Theta(x)$ is zero for $x < 0$, and one for $x \geq 0$, and ensures that tips do not branch during the refractory period. For a given tip, the mean time between branching events in given tip is $< \tau >= \tau_0 + 1/s$. We noted, however, that a refractory period alone was not sufficient to account for the observed deviation from the exponential decay of duct length, suggesting further remodeling might take place during the organoid growth. Careful observation of the 3D reconstructed organoids (Fig. 5C and S5D) revealed that newly branches tips have a characteristic size of about 40 microns, which also contributed to a low frequency of short ducts. With these two features, a refractory period, and a typical size of tip at branching, the model recapitulated the morphological properties of ducts (Fig. 5E).

Based on experimental observations, we considered two types of tip interactions: a termination mechanism, by which a tip arrests its growth when coming within the inhibition radius (R_a) of another particle, and a second longer-ranged mechanism by which a tip is repelled from existing tips and/or ducts. As the organoids are grown in free 3D space, we ran our numerical simulations considering an infinite system size. Simulations were terminated either when all tips became inactive, or when the predefined maximum simulation time was reached (set at the culturing time). To mimic the initial state of a branching organoids, we initialized our simulations with a rudimentary duct of unit length, where both ends were considered proliferative. The center-point of this initial duct is considered the root of the branching tree.

Numerical simulations of the BARW model

Simulations of the BARW were performed by implementing a finite difference algorithm, with a time-step $\Delta t = 1$. At every time-step active tips were chosen in random order to perform branching with probability σ /(1+ σ) or elongate with probability 1 /(1+ σ), σ denotes the ratio of branching to elongation rate of active tips. Tip termination was implemented by introduction of an inhibition radius R_a. Tip termination occurred when a tip got within the inhibition radius of another particle (tip or duct). Based on the observations that tips elongated freely as long as they did not collide with other ducts, and to prevent tips from terminating due to the presence of their own duct, tips only sensed other particles that lied within R_a and at an angle lower than $\pi/4$ with respect to the direction of movement of the tip. In the three-dimensional simulation, given the position $r_1 = (x_1, y_2, z_3)$ of an active tip elongating in a direction defined by the polar and azimuthal angles (θ, ϕ) in spherical coordinates, an elongation event implied a translation of the active tip from position $r_1$to position

$$r_2 = r_1 + L(sin(\theta')cos(\phi'), sin(\theta')sin(\phi'), cos(\theta')),$$

where the step length was fixed to unity, $L = 1$. The direction (θ', ϕ') related to the orientation of the parent particle (θ, ϕ) by

$$(\theta', \phi') = (\theta, \phi) + \delta\theta(arcos(1 - 2u_1) - \pi/2, u_2),$$

where the second term on the right-hand side corresponds to a random noise distributed uniformly on a 2D sphere, with $u_1 \in U([0,1[)$ and $u_2 \in U([-\pi, \pi])$, and $\delta\theta \in [0,1]$ is the noise amplitude. When $\delta\theta = 0$, there is no noise in the system and ducts grow following a perfect straight line, with infinite persistence.

For positive values of $\delta\theta$, ducts deviate from a straight line as they grow, with $\delta\theta = 1$ corresponding to a random walk. A self-avoidance mechanism was introduced as described by Hannezo *et al.*[30]. This implementation considers that a tip at position r_i can sense a repulsive force from all other particles r_j within a repulsion radius R_a, i.e. $|r_i - r_j| \leq R_a$. Additionally, we considered that the affected tip could only sense those particles in the half-space in front of it, as described for the inhibition process. Considering the direction of the center of mass of all repelling particles with respect to the location of the tip r_i

$$p_i = \frac{\sum_j \quad (r_i - r_j)}{\left|\sum_j \quad (r_i - r_j)\right|},$$

then the active tip suffered, at each elongation event, an additional displacement opposite to the direction of the repelling particles of the form $-f_r r_i$, where f_r corresponded to the strength of the repulsive force. During a branching event, two new branches were generated forming an angle α between them. The orientations of the new branches were defined as described by Hannezo *et al.*[30]. To account for the typical size of tips at branching, we positioned the offspring branches at a distance L_b from the parent tip, with L_b chosen at random from a uniform distribution between L and the typical radius of active tips. The parent duct and the two offspring branches were considered coplanar, and the angle of rotation of the two offspring branches with respect to the plane perpendicular to the parent duct was chosen randomly from a uniform distribution, mimicking the isotropic growth of BRCOs. A refractory period τ_0 was also introduced, such that if a given tip underwent a branching event at time t, the same tip could only terminate, or branch again after the time $t + \tau_0$ had been reached. This refractory time was independent for each active tip and accounted for a maturation period before a tip could branch again.

Estimating model parameters from BRCO data

In three-dimensions, the BARW has two key parameters that must be defined, the branching-to-elongation rate ratio σ, which measures how often a tip branches in relation to its elongation, and the inhibition radius R_a. From live-imaging of growing organoids (Video S1), we estimated the duct elongation speed to be on the order of $5\ \mu m/h$, with which we calibrated our numerical step-length $L = 1$ to $5\ \mu m$ and time-step $\Delta t = 1$ to 1 hour. $From\ this$, and the average duct length between two bifurcation events of 108 μm, we estimated = $\sigma = 0.05\ \pm 0.001$ (SD) between the (n=3) BRCO samples. Through fitting, we found that the lower bound $\sigma = 0.04$ achieved the best results. It is worth noting that the elongation rate of $5\ \mu m/h$ is an approximated measure that may have contribution both from tip elongation and tissue reorganisation in BRCOs. The inhibition radius was set to $R_a = 80\ \mu m$, which was estimated from the typical diameter of growing tips.

Organoids were cultured for approximately 7-8 days, so we set the maximum simulation time to 8 days (192 hours). The refractory period was estimated from the small size plateau in the duct length distribution to be $\tau_0 \approx 10$ hours. The parameter L_b, for the typical size of tips at branching, was chosen from a uniform distribution with bounds 5 μm and 40 μm (the typical radius of tips), which resulted in good qualitative agreement with the data. The repulsion radius R_r was set to $R_r = 1.2R_a = 120\ \mu m$, with a repulsive strength of $f_r = 0.2$. These parameters were adjusted to provide qualitative agreement

with experimental observations of tip-tip repulsion (see Video S3). We note that the overall measures of the network topology and long-term decay of the duct length distribution depended weakly on different choices of τ_0, L_b, R_r and f_r , yet they are essential for the model to account for the fine structure in the data.

To estimate the noise amplitude $\delta\theta$, we measured the relative deviation $(L_d - l_d)/l_d$, of the duct length L_d between two consecutive branch points and the straight distance between the branch points l_d. This resulted in a value of 0.14, corresponding approximately to $\delta\theta^2$, so that $\delta\theta = 0.37$. Variations of this parameter did not affect the quantitative measurements of the ductal network topology. Finally, the angle formed by offspring branches (see Fig. S5I) had a typical value of $95°(SD = 50°)$. However, we note that this measure is likely affected by the clearing process, where organoids are flattened when the structural support is removed, hence the large variance. In the numerical simulations we considered that the angle α between offspring branches was uniformly distributed, $\alpha \in U([80°, 110°])$. Quantitative measurements showed little sensitivity to changes in the distribution of α.

Model parameter for simulation or BRCCAOs

As BRCAAOs lacked a well-defined branching network, it was impossible to reconstruct its ductal structure and estimate parameters for this system. Instead, we hypothesized how the different model parameters could have been affected based on empirical observation. Bright field and confocal images revealed that BRCCAOs have a particularly compact structure, unlike in BRCOs where ducts are dispersed. This dense nature of BRCCAOs, as indicated by a smaller size of BRCCAOs compared to BRCOs after 7-8 days of culture (Fig. 7D), was an indication that the tip-duct and tip-tip interaction mechanisms might be compromised. To account for this in the model, we considered the extreme case were both the inhibition (R_a) and repulsion (R_r) radii are zero, eliminating tip-tip and tip-duct interaction altogether. Moreover, the dense organization of BRCCAOs was also reflected in the morphology of their boundary. These organoids were characterized by having a well-defined boundary, without long duct protruding outwards (as was the case in BRCOs), which was quantified by measuring the organoid circularity (Fig. 7D). From the perspective of the BARW model, this implies that BRCCAOs have a reduced capacity to form elongated, persistent ducts, which we accounted for in the model by doubling the noise amplitude with respect to the value for BRCOs, so that, we set to $\delta\theta = 0.74$. This accounted, qualitatively, to the morphological differences observed between BRCOs and BRCCAOs (Fig. S7F).

Goodness of fit

Comparison between the distributions of duct lengths, subtree sizes and persistence, end-to-end node distances, and termination probability were performed using a goodness of fit statistic R^2. Given a set of $n$of experimental measurement $(x_1, x_2, \ldots, x_n)$, whose average value is given by $\underline{x}$, and a corresponding set of theoretical predictions $(y_1, y_2, \ldots, y_n)$, then

$$R^2 = 1 - \frac{\sum_{i=1}^{n} (x_i - y_i)^2}{\sum_{i=1}^{n} (x_i - \underline{x})^2},$$

which takes values in [0,1]. A value of $R^2 = 1$, indicates that the prediction fits the data perfectly.

DAPT, BMS493 and Chimeric Jagged 1 assay

Effect of inhibiting the retinoic acid receptor on BRCOs was evaluated by adding BMS493 (1µM, Sigma) for 120 hours to the culture medium of BRCOs.[34] Additionally, the effect of inhibiting the NOTCH receptor on branching was assessed by incubating BRCOs with DAPT (50 µM) for ten days. Normal BRCOs and BRCOs exposed to vehicle control (DMSO) were taken along as a control. Similarly, in a dose dependent (50ng/mL; 80ng/mL; 100ng/mL; 200ng/mL and 500ng/mL) testing manner recombinant Human Jagged 1 Fc Chimera (Biotechne; RZL2220041) was added to the culture conditions of the ICOs derived from the Alagille Syndrome patient to improve branching in these organoids. To evaluate branching morphogenesis over time, the process was captured by transmission microscopy (EVOS® FL Cell Imaging System, ThermoFisher) for all medium additions.

Western Blot assay

For Western Blotting samples from ICOs (n=3) and ICOs from the (corrected) Alagille patient were obtained. The organoids were lysed with house made 2x Laemmli Sample Buffer (Bio-Rad, 161-0737) supplemented with 1,4-Dithithreitol (DTT; 0.1M) for 5 minutes at 95°C. Protein concentrations were evaluated with the bicinchoninic acid (BCA) protein assay (ThemoFisher Scientific; 23227) according to the manufacturer's protocol. Protein samples migrated through a sulfate polyacrylamide gel (8%) in running buffer for 105 minutes at 100 V and were blotted to a polyvinlylideenfluoride membrane (Merck Chemicals BV; IPFL85R) using blotting buffer for 2 hours at 250 mA. Molecular weight of proteins was determined using precision plus protein dual color standard (Bio-Rad; 1610374) 250 kDa marker. Membranes were blocked with Odyssey blocking buffer (Westburg BV; 927-40000) for 1 hour at room temperature. Subsequently, membranes were incubated overnight at 4°C with a polyclonal antibody to JAGGED1 and a monoclonal β-actin antibody. Followed by one hour incubation with secondary antibodies after washing. Immunoblots were scanned by Odyssey 3.0 (Clx) imaging system and analyzed using Image Studio Lite (Version 5.2).

DNA processing and sequencing of *JAGGED1*

Two full domes (25 µL) of ICOs derived from an AGS patient were collected by centrifuging in a 15 mL tube for 5 minutes, 4°C at 453 g. DNA was isolated from the obtained pellet using QIAamp Micro DNA kits (Qiagen) according to the manufacturer's protocol. Subsequently, the concentration was measured on a NANOdrop 2000 (ThermoFisher). Using Sanger sequencing (Macrogen) and Multiplex Ligation-dependent Probe Amplification analysis (Probemix P184, version C3; MRC Holland) two large heterozygous deletions were detected. Further sequence of the mutated strand was determined by PCR amplification using GoTaq (Promega Benelux BV; M7805) and Q5 high-fidelity DNA polymerase according to manufacturer's protocol (NEB; M0491) and subsequently analyzed using gel electrophoresis. Finally, amplicons were Sanger sequenced until the exact mutation was obtained. The used primers are listed in Table S2. In addition, DNA was obtained from BRCOs (n=3) to investigate oncogenic mutations and chromosomal stability of long-term passaged BRCOs (>passage 15). DNA was isolated and concentration was measured similar as described above from two full domes (50 µL) of BRCOs. Subsequently, targeted next generation sequencing was performed by semiconductor sequencing with the Ion Torrent platform using the supplier's materials and protocols (Thermo Fisher Scientific) with a custom-made dedicated panel for mutational analysis (65 genes).[87] In addition, the panel comprised 262 highly polymorphic single

nucleotide polymorphism (SNP) amplicons for copy number variation (CNV) detection (chromosomes: 1p, 2p, 3p, 5q, 6p, 7pq, 8pq, 9p, 10q, 11q, 12q, 13q, 15q, 16q, 17pq, 18q, 19pq and Xpq). Library and template preparations were performed consecutively with the AmpliSeq Library Kit 2.0-384 LV and the Ion 540 Chef kit. Sequencing was performed on a 540 chip with the Ion GeneStudio S5XL system. Data were analyzed with Sequence Pilot Analysis Software (JSI Medical Systems). CNV (ie, amplifications, gains and deletions) was analyzed by normalized coverage using the Sequence Pilot Analysis Software.

Bulk RNA-seq of primary tumor and tumor organoids

RNA from CCA primary tissue and CCAOs and BRCCAOs (n=3 biological replicates) was collected in lysis buffer (QIAzol lysis reagent, Qiagen) and the RNA was isolated using the miRNeasy mini kit (Qiagen) as previously described under the subheading RNA-isolation. Bulk RNA-seq was performed by Novogene (Beijing, China) resulting in 20-30 million, 150 nucleotides long, paired-end reads. Sequencing data were uploaded to the Galaxy Web platform public server usegalaxy.org.[88] Sequences were trimmed for adapters using Trim Galore! (Version 0.4.3.1), and mapped using RNA STAR (version 2.6.8a)[80] against the human reference genome (GRCh38). Mapped reads were translated to counts using FeatureCounts (version 2.0.1)[81] applying the built-in hg38 genome annotation file. CCA primary tissue bulk RNA-seq data from patient CCA1 was retrieved from a previously published manuscript (accession number GSE84073)[20] and incorporated into our dataset. Raw counts were batch corrected using ComBat-seq[89] (available via sva package version 3.36.0) using a negative binomial regression model. Analysis of differential expression was performed using edgeR[90] (version 3.32.1) and Limma86 (version 3.46.0)[91] R packages. Genes were considered differentially expressed when the adjusted p-value was <0.05 (Benjamini Hochberg FDR corrected). Subsequent GSEA on the log2FC values was done using fgsea[84] (version 1.16.0) and gage[92] (version 2.40.1) R packages. To increase specificity, fgsea results were filtered using gage results so that only pathways which are significant and in the same direction in both methods are retained. To assess similarity between tissue and organoid, we filtered total genes to only include DE genes between CCAOs and BRCCAOs. This set of genes was used to create a Pearson's correlation matrix.

***In vitro* drug assay on (BR)CCAOs**

CCAOs (n=3) and matching BRCCAOs (n=3) were dissociated to single cells or small clumps with TrypLE (ThermoFisher; 12604013) for 3 x 5 minutes at 37˚C while applying mechanical disruption through pipetting. TrypLE was inactivated by adding cold AdvDMEM/F12, centrifuged for 5 minutes (4˚C at 453 g) and counted for plating out at a concentration of 5000 cells/5 µL BME in 96 well plates (Cellstar). Organoids were cultured for three days. Subsequently, a concentration dilution series of gemcitabine (range 10nM-10µM), cisplatin, or a combination of both compounds was added and cell viability was measured using CellTiter-Glo (Promega) after 72 hours. All experimental conditions were tested in biological and technical triplicate. An experimental concentration range was determined and dose-response curves were fitted using nonlinear least squares regression fitting and plotted relatively compared to non-treated controls.

Statistical analyses

Data are presented as mean ± standard deviation (SD) unless otherwise specified. Data other than sequencing data were analyzed and plotted using Prism Software 8.0 (GraphPad). Biological and technical

replicates are specified in the figure legends for each experiment. In all tests, a P value of <0.05 is considered significant and was determined by two-tailed Student's t test, unless otherwise specified in the figure legends. When comparing more than two means, significance was assessed by ANOVA tests.

SUPPLEMENTARY ITEM TITLES

1. Table S1. Patient and organoid culture characteristics
2. Table S2. List of genes and primers used
3. Figure S1. BRCOs represent complex tubular biliary organoids that can only be established from intrahepatic cholangiocytes.
4. Figure S2. BRCOs are significantly limited in their proliferation compared to ICOs.
5. Figure S3. Protein expression analyzed by SILAC reveals differences between BRCOs and ICOs.
6. Figure S4. scRNA-seq. demonstrates transcriptomic differences between BRCOs and ICOs.
7. Figure S5. BRCOs network reconstruction and statistics.
8. Figure S6. Pathways important for branching in BRCOs.
9. Figure S7. Additional characterization of BRCCAOs.
10. Video S1. BRCO growth and Mature BRCO
11. Video S2. Whole mount confocal of KRT7 F-actin and DAPI on BRCOs
12. Video S3. Tip avoidance in BRCOs
13. Video S4. Inhibiting TGF-β pathway in BRCOs
14. Supplementary File 1: Transcriptomics and proteomics
15. Key resource table

References

1. Castaing D. Surgical anatomy of the biliary tract. HPB (Oxford). 2008;10(2):72-76.
2. Zong Y, Stanger BZ. Molecular mechanisms of bile duct development. Int. J. Biochem. Cell Biol. 2011;43:257–264.
3. Si-Tayeb K, Lemaigre FP, Duncan SA. Organogenesis and development of the liver. Dev Cell. 2010;18(2):175-189.
4. Strazzabosco M, Fabris L. Functional anatomy of normal bile ducts. Anat Rec (Hoboken). 2008;291(6):653-660.
5. Boyer JL. Bile formation and secretion. Compr Physiol. 2013 Jul;3(3):1035-78.
6. Hannezo E, Simons BD. Multiscale dynamics of branching morphogenesis. Curr Opin Cell Biol. 2019 Oct;60:99-105.
7. Huch M, Gehart H, Boxtel R van, *et al.* Long-term culture of genome-stable bipotent stem cells from adult human liver. Cell. 2015;1–14.
8. Rimland CA, Tilson SG, Morell CM, *et al.* Regional differences in human biliary tissues and corresponding *in vitro* derived organoids. Hepatology. 2021 Jan;73(1):247-267.
9. Sampaziotis F, Justin AW, Tysoe OC, *et al*. Reconstruction of the mouse extrahepatic biliary tree using primary human extrahepatic cholangiocyte organoids. Nat. Med. 2017;23:954–963.
10. Sampaziotis F, de Brito MC, Madrigal P, *et al.* Cholangiocytes derived from human induced pluripotent stem cells for disease modeling and drug validation. Nat Biotechnol. 2015 Aug;33(8):845-852.
11. Verstegen MMA, Roos FJM, Burka K, *et al.* Human extrahepatic and intrahepatic cholangiocyte organoids show region-specific differentiation potential and model cystic fibrosis-related bile duct disease. Sci Rep. 2020 Dec 14;10(1):21900.
12. Tysoe OC, Justin AW, Brevini T, *et al.* Isolation and propagation of primary human cholangiocyte organoids for the generation of bioengineered biliary tissue. Nat Protoc. 2019 Jun;14(6):1884-1925.
13. Aizarani N, Saviano A, Sagar, *et al*. A human liver cell atlas reveals heterogeneity and epithelial progenitors. Nature. 2019 Aug;572(7768):199-204.
14. Planas-Paz L, Sun T, Pikiolek M, *et al.* YAP, but Not RSPO-LGR4/5, Signaling in Biliary Epithelial Cells Promotes a Ductular Reaction in Response to Liver Injury. Cell Stem Cell. 2019 Jul 3;25(1):39-53.e10.
15. Segal JM, Kent D, Wesche DJ, *et al.* Single cell analysis of human foetal liver captures the transcriptional profile of hepatobiliary hybrid progenitors. Nat Commun. 2019 Jul 26;10(1):3350.
16. MacParland SA, Liu JC, Ma XZ, *et al.* Single cell RNA sequencing of human liver reveals distinct intrahepatic macrophage populations. Nat Commun. 2018;9(1):4383.
17. Li L, Krantz ID, Deng Y, *et al*. Alagille syndrome is caused by mutations in human Jagged1, which encodes a ligand for Notch1. Nat Genet. 1997;16(3):243-251.
18. Oda T, Elkahloun AG, Pike BL, *et al.* Mutations in the human Jagged1 gene are responsible for Alagille syndrome. Nat Genet. 1997;16(3):235-242.
19. McDaniell R, Warthen DM, Sanchez-Lara PA, *et al.* NOTCH2 mutations cause Alagille syndrome, a heterogeneous disorder of the notch signaling pathway. Am J Hum Genet. 2006;79(1):169-173.
20. Broutier L, Mastrogiovanni G, Verstegen MMA, *et al.* Human primary liver cancer-derived organoid cultures for disease modeling and drug screening. Nat Med. 2017;23(12):1424-1435.
21. Cordi S, Godard C, Saandi T, *et al.* Role of β-catenin in development of bile ducts. Differentiation; Research in Biological Diversity. 2016 Jan-Mar;91(1-3):42-49.

22. Alvaro D, Benedetti A, Marucci L, *et al*. The function of alkaline phosphatase in the liver: regulation of intrahepatic biliary epithelium secretory activities in the rat. Hepatology. 2000 Aug;32(2):174-84.
23. Hashimshony T, Senderovich N, Avital G, *et al.* CEL-Seq2: sensitive highly-multiplexed single-cell RNA-Seq. Genome Biol. 2016 Apr 28;17:77.
24. LeSage GD, Benedetti A, Glaser S, *et al*. Acute carbon tetrachloride feeding selectively damages large, but not small, cholangiocytes from normal rat liver. Hepatology. 1999 Feb;29(2):307-19.
25. LeSage GD, Glaser SS, Marucci L, *et al*. Acute carbon tetrachloride feeding induces damage of large but not small cholangiocytes from BDL rat liver. Am J Physiol. 1999 May;276(5):G1289-301.
26. Maroni L, Haibo B, Ray D, et al. Functional and structural features of cholangiocytes in health and disease. Cell Mol Gastroenterol Hepatol. 2015 Jul 1;1(4):368-380.
27. Uhlén M, Fagerberg L, Hallström BM, *et al.* Tissue-based map of the human proteome. Science. 2015 Jan 23;347(6220):1260419.
28. Jiang X, Karlsen TH. Genetics of primary sclerosing cholangitis and pathophysiological implications. Nat Rev Gastroenterol Hepatol 2017;14:279-295
29. Sampaziotis F, Muraro D, Tysoe OC, *et al*. Cholangiocyte organoids can repair bile ducts after transplantation in the human liver. Science. 2021 Feb 19;371(6531):839-846.
30. Hannezo E, Scheele CLGJ, Moad M, *et al.* A Unifying Theory of Branching Morphogenesis. Cell. 2017 Sep 21;171(1):242-255.
31. Pepe-Mooney BJ, Dill MT, Alemany A, *et al.* Single-Cell Analysis of the Liver Epithelium Reveals Dynamic Heterogeneity and an Essential Role for YAP in Homeostasis and Regeneration. Cell Stem Cell. 2019 Jul 3;25(1):23-38.e8.
32. Goessling W, North TE, Lord AM, *et al.* APC mutant zebrafish uncover a changing temporal requirement for wnt signaling in liver development. Dev Biol. 2008;320(1):161-174.
33. McLin VA, Rankin SA, Zorn AM. Repression of Wnt/beta-catenin signaling in the anterior endoderm is essential for liver and pancreas development. Development. 2007;134(12):2207-2217.
34. Yimlamai D, Christodoulou C, Galli GG, *et al.* Hippo pathway activity influences liver cell fate. Cell. 2014 Jun 5;157(6):1324-1338.
35. Koike H, Iwasawa K, Ouchi R, *et al.* Modelling human hepato-biliary-pancreatic organogenesis from the foregut-midgut boundary. Nature. 2019 Oct;574(7776):112-116.
36. McCright B, Lozier J, Gridley T. A mouse model of Alagille syndrome: Notch2 as a genetic modifier of Jag1 haploinsufficiency. Development. 2002 Feb;129(4):1075-82.
37. Banales JM, Cardinale V, Carpino G, *et al.* Cholangiocarcinoma: current knowledge and future perspectives consensus statement from the European Network for the Study of Cholangiocarcinoma (ENS-CCA). Nature Reviews Gastroenterology & Hepatology. 2016 May;13(5):261-80.
38. Odenwald MA, Choi W, Buckley A, *et al.* ZO-1 interactions with F-actin and occludin direct epithelial polarization and single lumen specification in 3D culture. Journal of cell science. 2017 Jan 1;130(1):243-59.
39. Nunes-Xavier C, Roma-Mateo C, Rios P, *et al.* Dual-specificity MAP kinase phosphatases as targets of cancer treatment. Anti-Cancer Agents in Medicinal Chemistry (Formerly Current Medicinal Chemistry-Anti-Cancer Agents). 2011 Jan 1;11(1):109-32.
40. Lamb JA, Ventura JJ, Hess P, *et al.* JunD mediates survival signaling by the JNK signal transduction pathway. Molecular cell. 2003 Jun 1;11(6):1479-89.
41. Bhandari V, Hoey C, Liu LY, *et al.* Molecular landmarks of tumor hypoxia across cancer types. Nature genetics. 2019 Feb;51(2):308-18.
42. Colak S, Ten Dijke P. Targeting TGF-β signaling in cancer. Trends in cancer. 2017 Jan 1;3(1):56-71.

43. Banales JM, Marin JJ, Lamarca A, *et al.* Cholangiocarcinoma 2020: the next horizon in mechanisms and management. Nature Reviews Gastroenterology & Hepatology. 2020 Sep;17(9):557-88.
44. Li L, Knutsdottir H, Hui K, *et al.* Human primary liver cancer organoids reveal intratumor and interpatient drug response heterogeneity. JCI insight. 2019 Jan 24;4(2).
45. Gupta A, Gautam P, Wennerberg K, *et al*. A normalized drug response metric improves accuracy and consistency of anticancer drug sensitivity quantification in cell-based screening. Communications biology. 2020 Jan 23;3(1):1-2.
46. Reddy LH, Couvreur P. Novel approaches to deliver gemcitabine to cancers. Curr Pharm Des. 2008;14(11):1124-37.
47. Ciccolini J, Serdjebi C, Peters GJ, Giovannetti E. Pharmacokinetics and pharmacogenetics of Gemcitabine as a mainstay in adult and pediatric oncology: an EORTC-PAMM perspective. Cancer Chemother Pharmacol. 2016 Jul;78(1):1-12.
48. Bapiro TE, Richards FM, Goldgraben MA, *et al.* A novel method for quantification of gemcitabine and its metabolites 2',2'-difluorodeoxyuridine and gemcitabine triphosphate in tumour tissue by LC-MS/MS: comparison with (19)F NMR spectroscopy. Cancer Chemother Pharmacol. 2011 Nov;68(5):1243-53.
49. Valle J, Wasan H, Palmer DH, *et al.* Cisplatin plus gemcitabine versus gemcitabine for biliary tract cancer. New England Journal of Medicine. 2010 Apr 8;362(14):1273-81.
50. Marsee A, Roos FJM, Verstegen MMA, *et al*. Building consensus on definition and nomenclature of hepatic, pancreatic, and biliary organoids. Cell Stem Cell. 2021 May 6;28(5):816-832
51. Scheele CL, Hannezo E, Muraro MJ, *et al*. Identity and dynamics of mammary stem cells during branching morphogenesis. Nature. 2017 Feb 16;542(7641):313-317
52. Sznurkowska MK, Hannezo E, Azzarelli R, *et al.* Defining Lineage Potential and Fate Behavior of Precursors during Pancreas Development. Dev Cell. 2018 Aug 6;46(3):360-375.
53. Smith Q, Bays J, Li L, *et al*. Directing Cholangiocyte Morphogenesis in Natural Biomaterial Scaffolds. Adv Sci (Weinh). 2022 Jan;9(3):e2102698.
54. Zong Y, Panikkar A, Xu J, *et al*. Notch signaling controls liver development by regulating biliary differentiation. Development. 2009;136(10):1727-1739.
55. Kodama Y, Hijikata M, Kageyama R, *et al*. The role of notch signaling in the development of intrahepatic bile ducts. Gastroenterology. 2004;127(6):1775-1786.
56. Geisler F, Strazzabosco M. Emerging roles of Notch signaling in liver disease. Hepatology. 2015;61(1):382-392.
57. Chen Y, Chen Z, Tang Y, *et al.* The involvement of noncanonical Wnt signaling in cancers. Biomed Pharmacother. 2021 Jan;133:110946.
58. Roskams T, Desmet V. Embryology of extra- and intrahepatic bile ducts, the ductal plate. Anat Rec (Hoboken). 2008 Jun;291(6):628-35.
59. Raven A, Lu WY, Man TY, *et al.* Cholangiocytes act as facultative liver stem cells during impaired hepatocyte regeneration. Nature. 2017 Jul 20;547(7663):350-354.
60. Zimmerli D, Hausmann G, Cantù C, *et al*. Pharmacological interventions in the Wnt pathway: inhibition of Wnt secretion versus disrupting the protein-protein interfaces of nuclear factors. Br J Pharmacol. 2017 Dec;174(24):4600-4610.
61. Shi RY, Yang XR, Shen QJ, *et al.* High expression of Dickkopf-related protein 1 is related to lymphatic metastasis and indicates poor prognosis in intrahepatic cholangiocarcinoma patients after surgery. Cancer. 2013 Mar 1;119(5):993-1003.

62. Goyal L, Sirard C, Schrag M, *et al*. Phase I and Biomarker Study of the Wnt Pathway Modulator DKN-01 in Combination with Gemcitabine/Cisplatin in Advanced Biliary Tract Cancer. Clin Cancer Res. 2020 Dec 1;26(23):6158-6167.
63. Chung YE, Kim MJ, Park YN, *et al*. Varying appearances of cholangiocarcinoma: radiologic-pathologic correlation. Radiographics. 2009 May-Jun;29(3):683-700.
64. Zhang M, Yang H, Wan L, *et al.* Single-cell transcriptomic architecture and intercellular crosstalk of human intrahepatic cholangiocarcinoma. J Hepatol. 2020 Nov;73(5):1118-1130.
65. Javle M, Lowery M, Shroff RT, Weiss KH, *et al.* Phase II Study of BGJ398 in Patients With FGFR-Altered Advanced Cholangiocarcinoma. J Clin Oncol. 2018 Jan 20;36(3):276-282.
66. Abou-Alfa GK, Macarulla T, Javle MM, *et al*. Ivosidenib in IDH1-mutant, chemotherapy-refractory cholangiocarcinoma (ClarIDHy): a multicentre, randomised, double-blind, placebo-controlled, phase 3 study. Lancet Oncol. 2020 Jun;21(6):796-807.
67. Nateri AS, Spencer-Dene B, Behrens A. Interaction of phosphorylated c-Jun with TCF4 regulates intestinal cancer development. Nature. 2005 Sep 8;437(7056):281-5.
68. Lamb JA, Ventura JJ, Hess P, *et al.* JunD mediates survival signaling by the JNK signal transduction pathway. Mol Cell. 2003 Jun;11(6):1479-89.
69. Vizcaíno JA, Deutsch EW, Wang R, et al. ProteomeXchange provides globally coordinated proteomics data submission and dissemination. Nat Biotechnol. 2014 Mar;32(3):223-6.
70. Broutier L, Andersson-Rolf A, Hindley CJ, *et al.* Culture and establishment of self-renewing human and mouse adult liver and pancreas 3D organoids and their genetic manipulation. Nat Protoc. 2016 Sep;11(9):1724-43.
71. Barker N, Huch M, Kujala P, *et al.* Lgr5(+ve) stem cells drive self-renewal in the stomach and build long-lived gastric units in vitro. Cell Stem Cell. 2010 Jan 8;6(1):25-36
72. Roest HP, Ooms LSS, Gillis AJM, *et al.* Cell-free MicroRNA miR-505-3p in Graft Preservation Fluid Is an Independent Predictor of Delayed Graft Function After Kidney Transplantation. Transplantation. 2019 Feb;103(2):329-335.
73. Clevers H, Gehart H. WO2017149025 - IMPROVED DIFFERENTIATION METHOD. Retrieved from Https://patentscope.wipo.int/search/en/detail.jsf?docId=WO2017149025&tab=PCTBIBLIO, accessed upon May 1st 2020.
74. Vanwolleghem T, Libbrecht L, Hansen BE, *et al*. Factors determining successful engraftment of hepatocytes and susceptibility to hepatitis B and C virus infection in upa-Scid mice. J Hepatol. 2010 Sep;53(3):468-76.
75. Dekkers JF, Wiegerinck CL, de Jonge HR, *et al.* A functional CFTR assay using primary cystic fibrosis intestinal organoids. Nat Med. 2013 Jul;19(7):939-45.
76. Roos FJM, Bijvelds MJC, Verstegen MMA, *et al.* Impact of hypoxia and AMPK on CFTR-mediated bicarbonate secretion in human cholangiocyte organoids. Am J Physiol Gastrointest Liver Physiol. 2021 Mar 3. Epub ahead of print.
77. Roos FJM, Verstegen MMA, Muñoz Albarinos L, *et al.* Human bile contains cholangiocyte organoid initiating cells which expand as functional cholangiocytes in non-canonical WNT stimulating conditions. Front Cell Dev Biol. 2021 Feb 9;8:630492.
78. Zilionis R, Nainys J, Veres A, *et al.* Single-cell barcoding and sequencing using droplet microfluidics. Nat Protoc. 2017 Jan;12(1):44-73.
79. Smith T, Heger A, Sudbery I. UMI-tools: modeling sequencing errors in Unique Molecular Identifiers to improve quantification accuracy. Genome Res. 2017 Mar;27(3):491-499.

80. Dobin A, Davis CA, Schlesinger F, *et al.* STAR: ultrafast universal RNA-seq aligner. Bioinformatics. 2013;29(1):15-21.
81. Liao Y, Smyth GK, Shi W. featureCounts: an efficient general purpose program for assigning sequence reads to genomic features. Bioinformatics. 2014 Apr 1;30(7):923-30.
82. Butler A, Hoffman P, Smibert P, *et al*. Integrating single-cell transcriptomic data across different conditions, technologies, and species. Nat Biotechnol. 2018 Jun;36(5):411-420.
83. Kuleshov MV, Jones MR, Rouillard AD, *et al.* Enrichr: a comprehensive gene set enrichment analysis web server 2016 update. Nucleic Acids Res. 2016 Jul 8;44(W1):W90-7.
84. Korotkevich G, Sukhov V, Sergushichev A. Fast gene set enrichment analysis. BioRxiv. 2019, doi: 10.1101/060012.
85. Wolf FA, Hamey FK, Plass M, *et al.* PAGA: graph abstraction reconciles clustering with trajectory inference through a topology preserving map of single cells. Genome Biol. 2019 Mar 19;20(1):59.
86. van Royen ME, Verhoef EI, Kweldam CF, *et al.* Three-dimensional microscopic analysis of clinical prostate specimens. Histopathology. 2016 Dec;69(6):985-992.
87. Hermans BCM, Derks JL, Hillen LM, *et al.* In-depth molecular analysis of combined and co-primary pulmonary large cell neuroendocrine carcinoma and adenocarcinoma. Int J Cancer. 2022 Mar 1;150(5):802-815.
88. Afgan E, Baker D, van den Beek M, *et al.* The Galaxy platform for accessible, reproducible and collaborative biomedical analyses: 2016 update Nucleic Acids Res. 2016 Jul 8;44(W1):W3-W10.
89. Hang Y, Parmigiani G, Johnson WE. *ComBat-seq*: batch effect adjustment for RNA-seq count data. NAR Genom Bioinform. 2020 Sep;2(3):lqaa078.
90. Robinson MD, McCarthy DJ, Smyth GK. edgeR: a Bioconductor package for differential expression analysis of digital gene expression data. Bioinformatics. 2010 Jan 1;26(1):139-40.
91. Ritchie ME, Phipson B, Wu D, Hu Y, Law CW, Shi W, Smyth GK. limma powers differential expression analyses for RNA-sequencing and microarray studies. Nucleic Acids Res. 2015 Apr 20;43(7):e47.
92. Salzberg SL, Phillippy AM, Zimin A, *et al.* GAGE: A critical evaluation of genome assemblies and assembly algorithms. Genome Res. 2012 Mar;22(3):557-67.

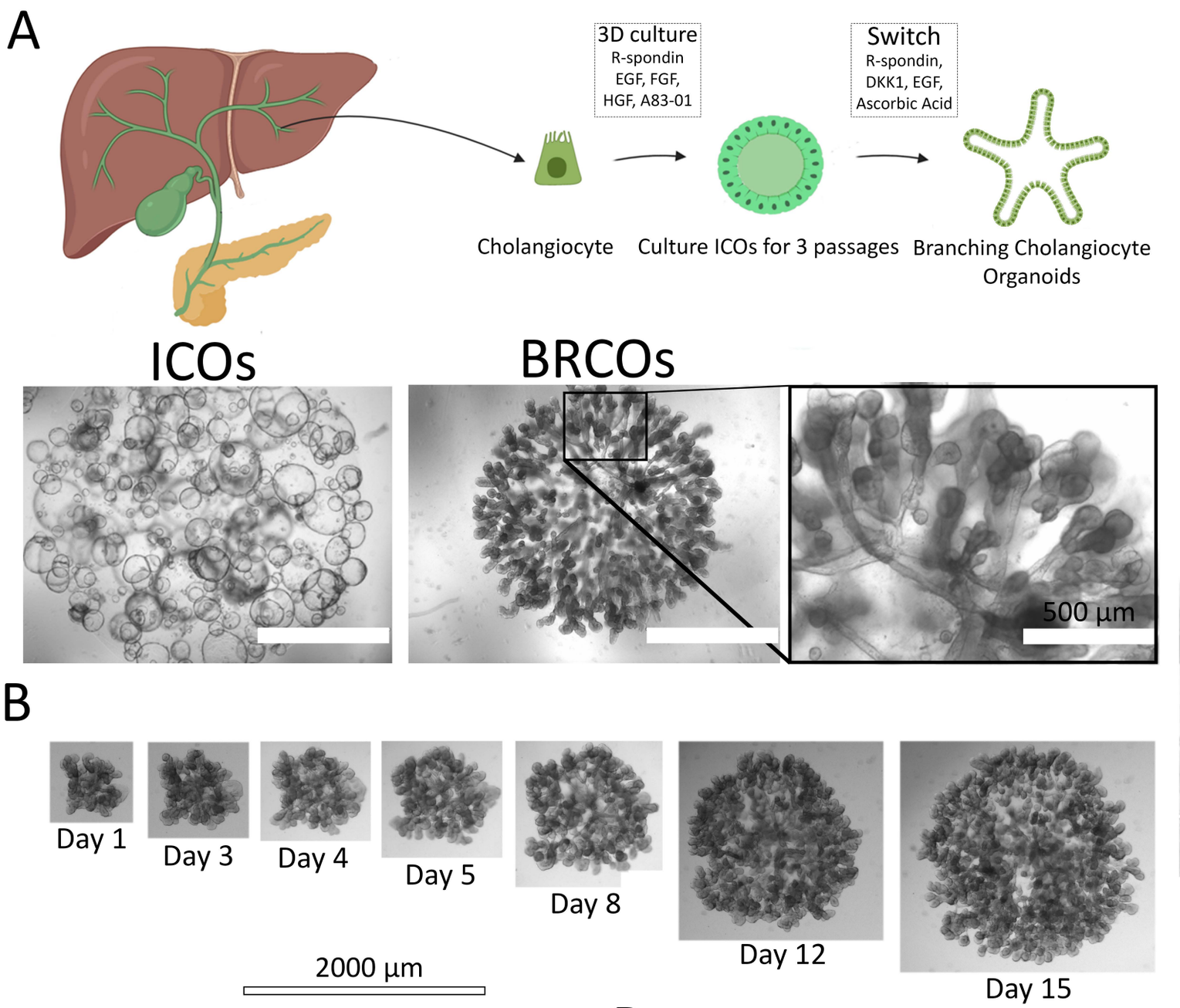
A
3D culture
R-spondin
EGF, FGF,
HGF, A83-01
Switch
R-spondin,
DKK1, EGF,
Ascorbic Acid
Cholangiocyte
Culture ICOs for 3 passages
Branching Cholangiocyte
Organoids
ICOs
BRCOs
500 µm

B
Day 1
Day 3
Day 4
Day 5
Day 8
Day 12
Day 15
2000 µm

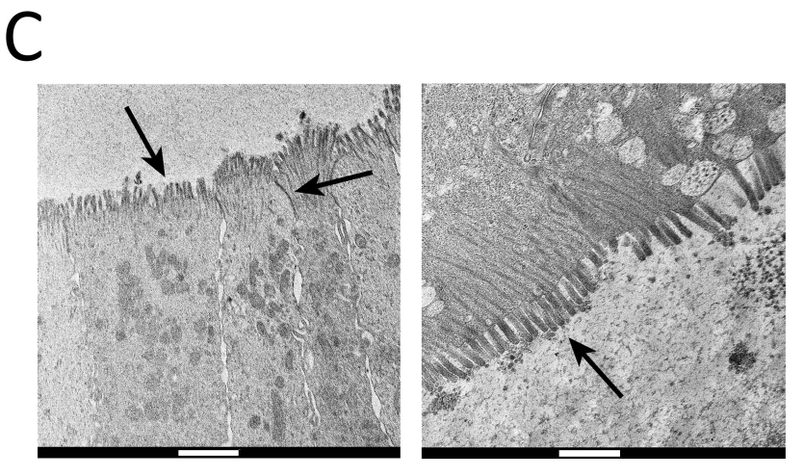
C

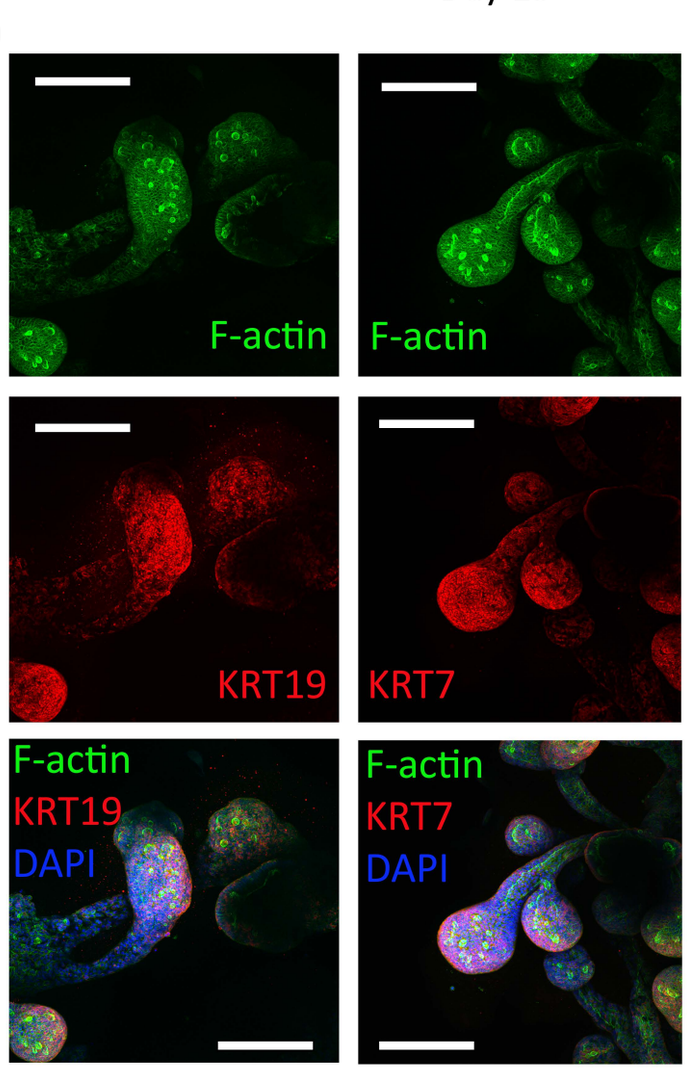
D
F-actin
F-actin
KRT19
KRT7
F-actin
KRT19
DAPI
F-actin
KRT7
DAPI

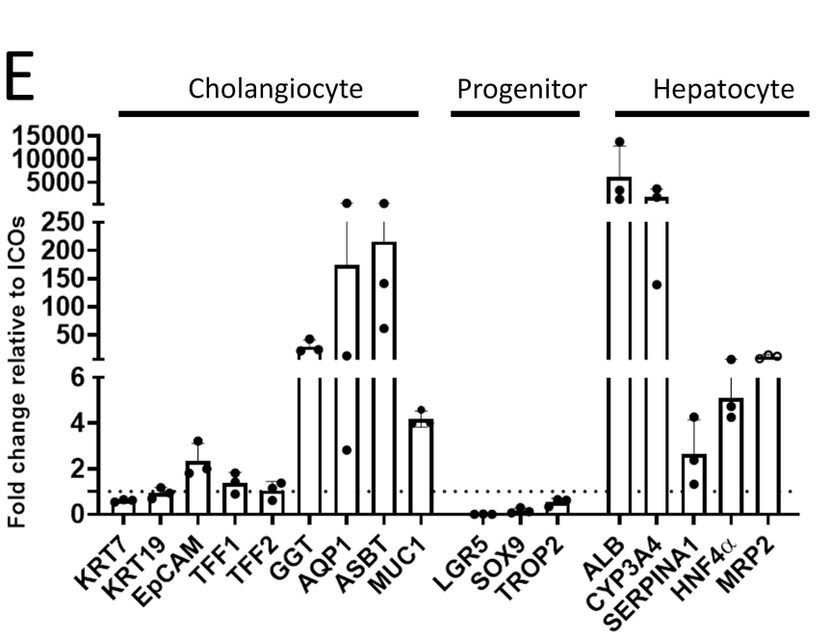
E
Cholangiocyte
Progenitor
Hepatocyte
Fold change relative to ICOs
15000
10000
5000
250
200
150
100
50
6
4
2
0
KRT7
KRT19
EpCAM
TFF1
TFF2
GGT
AQP1
ASBT
MUC1
LGR5
SOX9
TROP2
ALB
CYP3A4
SERPINA1
HNF4α
MRP2

A

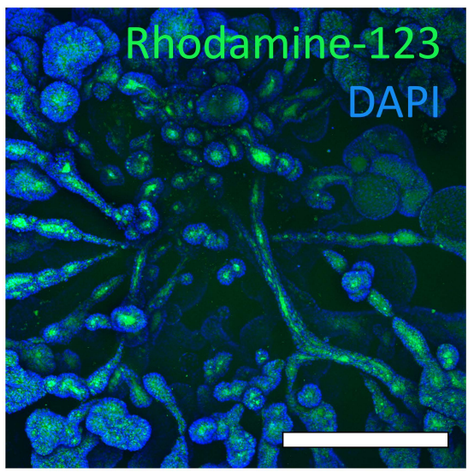
Rhodamine-123
DAPI

B

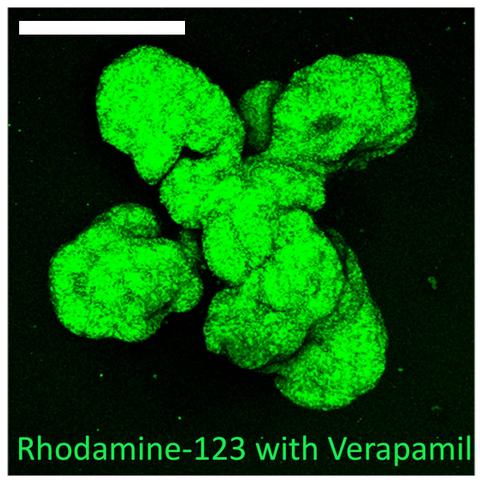
Rhodamine-123 with Verapamil

C

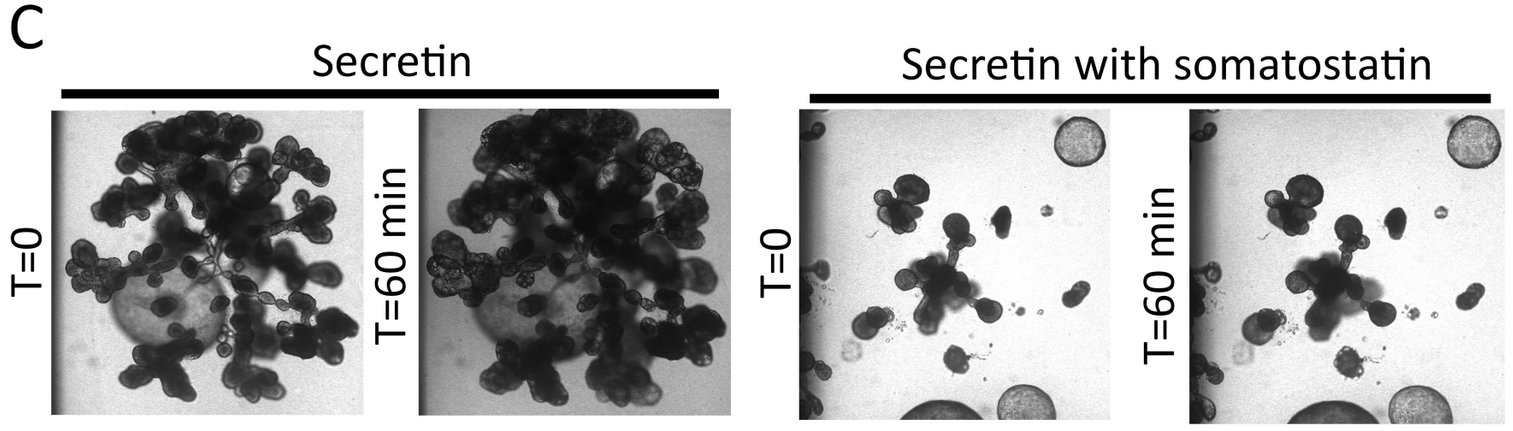
Secretin
T=0
T=60 min
Secretin with somatostatin
T=0
T=60 min

D

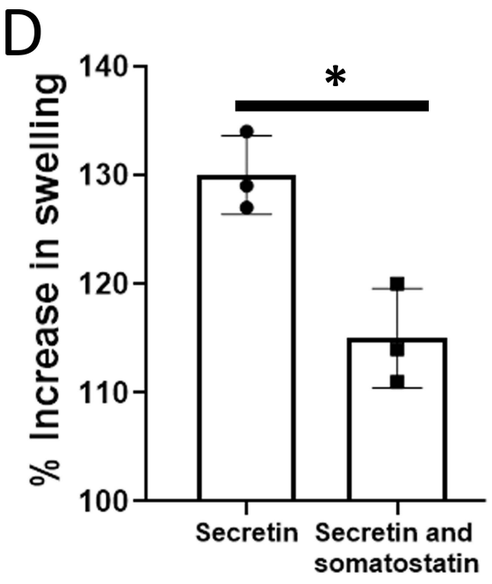
% Increase in swelling
140
130
120
110
100
*
Secretin
Secretin and somatostatin

E

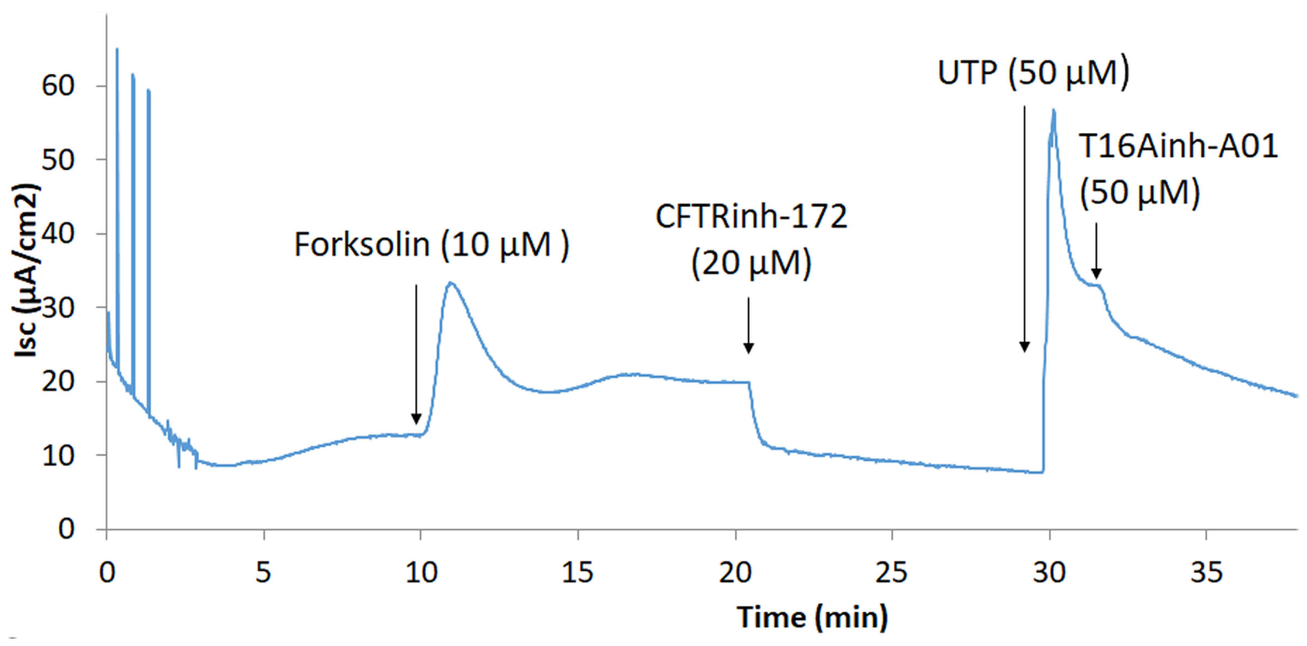
Isc (μA/cm2)
60
50
40
30
20
10
0
Forksolin (10 μM)
CFTRinh-172
(20 μM)
UTP (50 μM)
T16Ainh-A01
(50 μM)
0
5
10
15
20
25
30
35
Time (min)

F

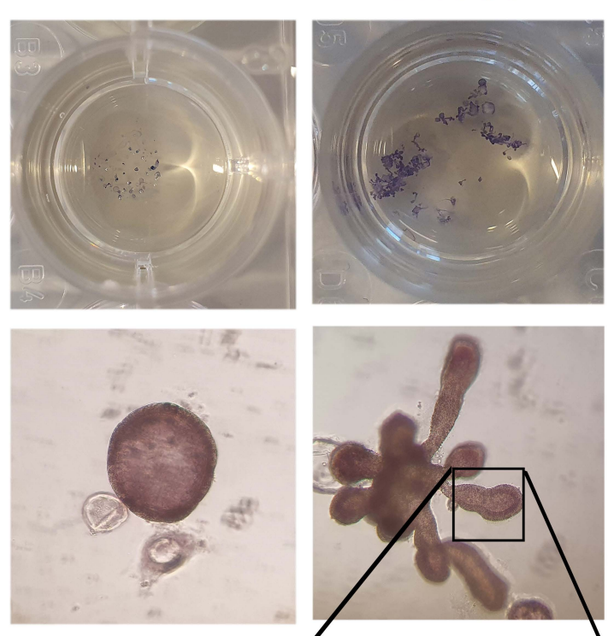
ICOs
BRCOs

G

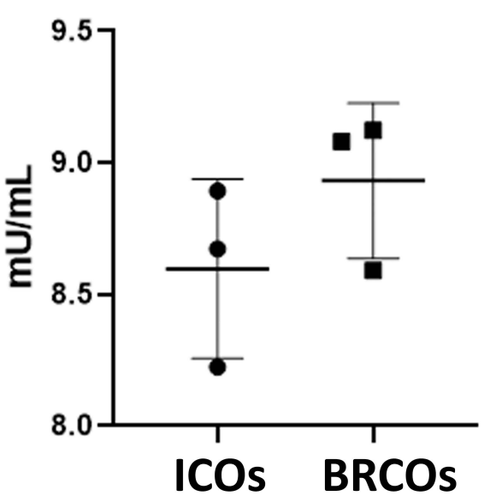
GGT Activity
mU/mL
9.5
9.0
8.5
8.0
ICOs
BRCOs

H

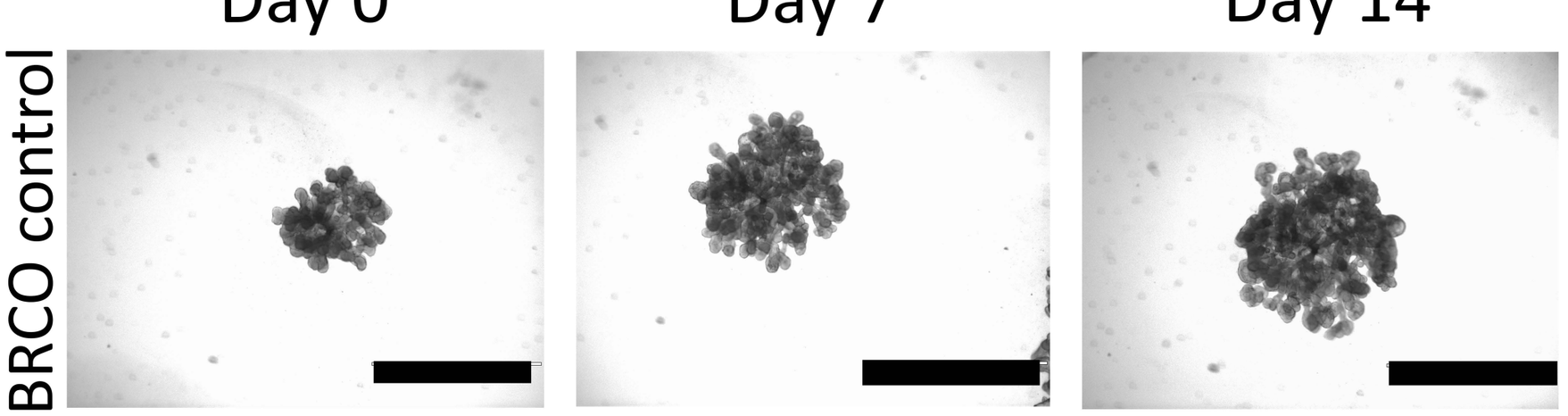
Day 0
Day 7
Day 14
BRCO control

I

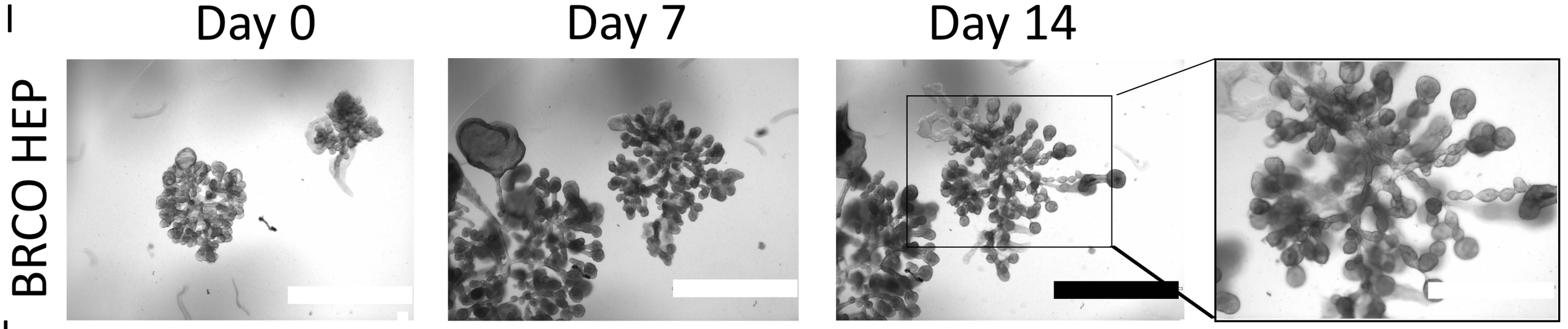
Day 0
Day 7
Day 14
BRCO HEP

J

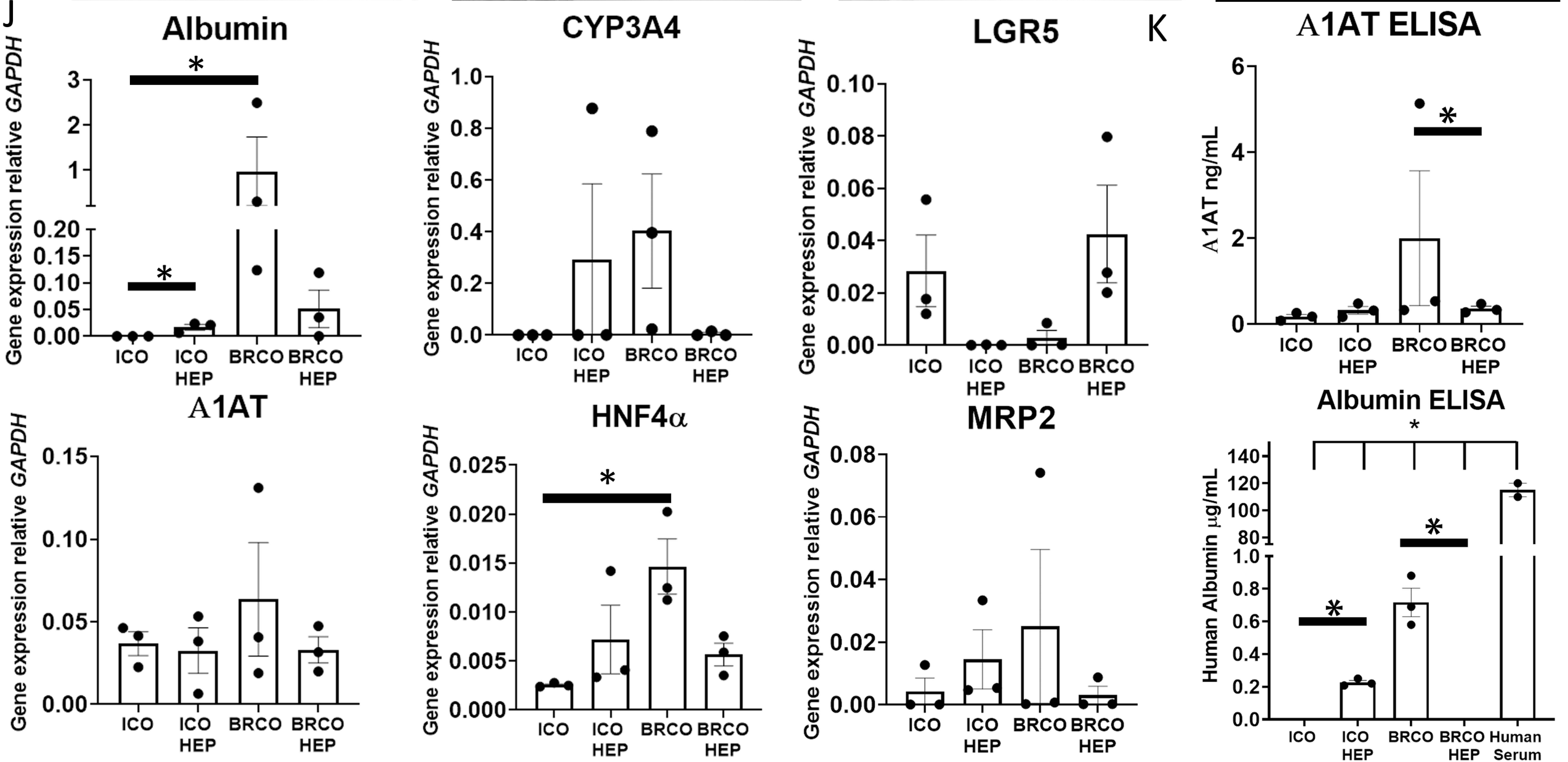
Albumin
CYP3A4
LGR5
A1AT ELISA
A1AT
HNF4α
MRP2
Albumin ELISA
Gene expression relative GAPDH
A1AT ng/mL
Human Albumin μg/mL
ICO
ICO HEP
BRCO
BRCO HEP
Human Serum

A

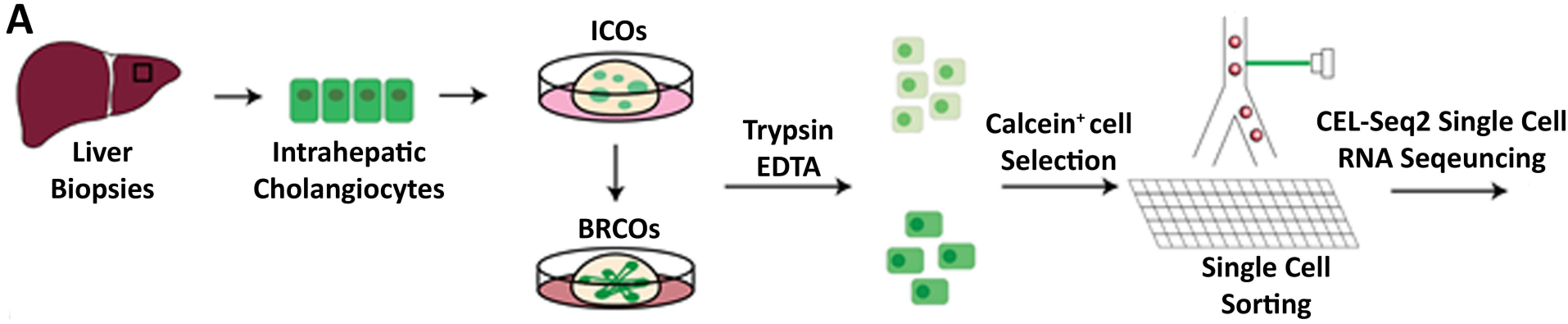
Liver Biopsies
Intrahepatic Cholangiocytes
ICOs
BRCOs
Trypsin EDTA
Calcein+ cell Selection
CEL-Seq2 Single Cell RNA Seqeuncing
Single Cell Sorting

B

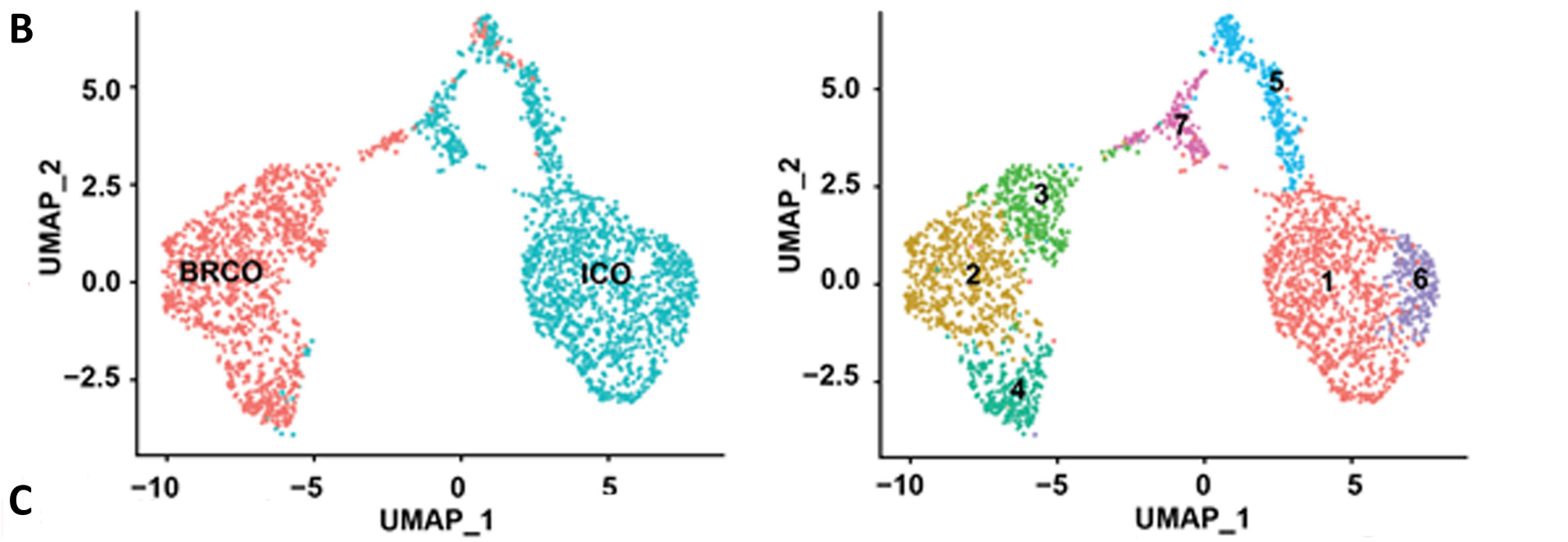
BRCO
ICO
UMAP_1
UMAP_2
1
2
3
4
5
6
7

C

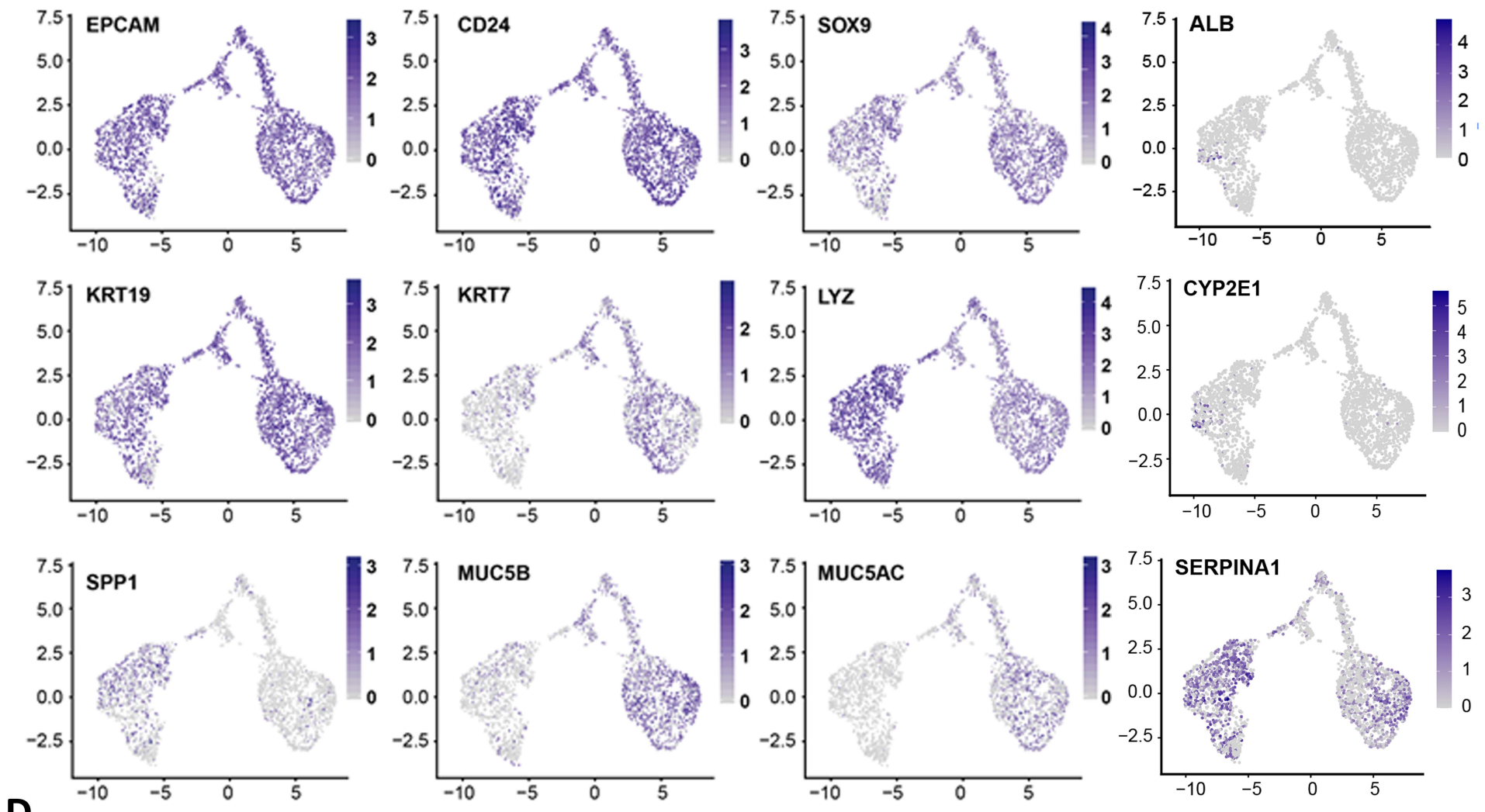
EPCAM
CD24
SOX9
ALB
KRT19
KRT7
LYZ
CYP2E1
SPP1
MUC5B
MUC5AC
SERPINA1

D

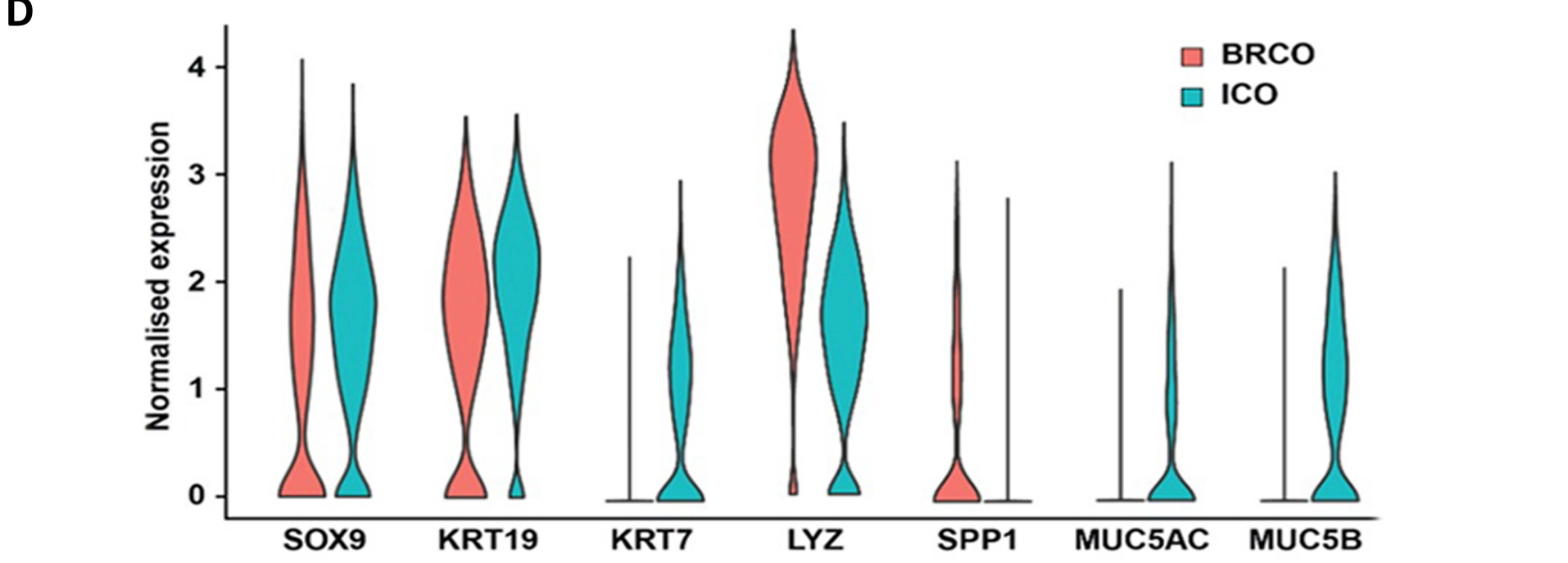
BRCO
ICO
Normalised expression
SOX9
KRT19
KRT7
LYZ
SPP1
MUC5AC
MUC5B

A

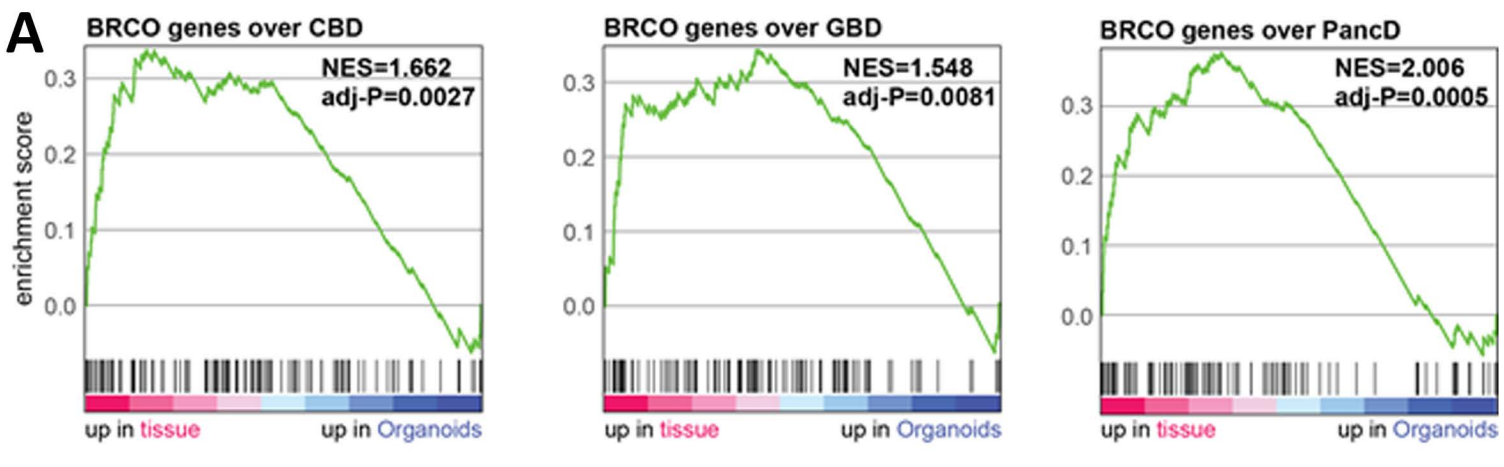
BRCO genes over CBD
NES=1.662
adj-P=0.0027
BRCO genes over GBD
NES=1.548
adj-P=0.0081
BRCO genes over PancD
NES=2.006
adj-P=0.0005
enrichment score
up in tissue
up in Organoids

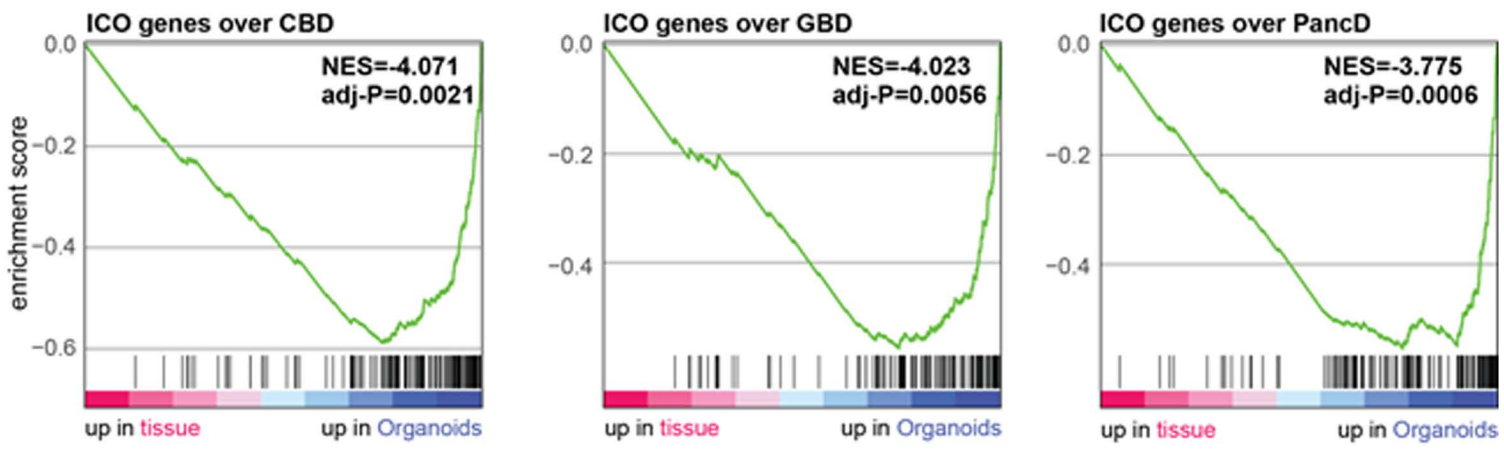
ICO genes over CBD
NES=-4.071
adj-P=0.0021
ICO genes over GBD
NES=-4.023
adj-P=0.0056
ICO genes over PancD
NES=-3.775
adj-P=0.0006
enrichment score
up in tissue
up in Organoids

B

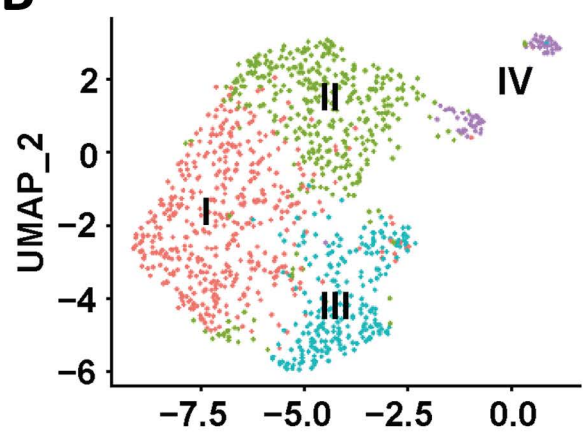
UMAP_2
I
II
III
IV

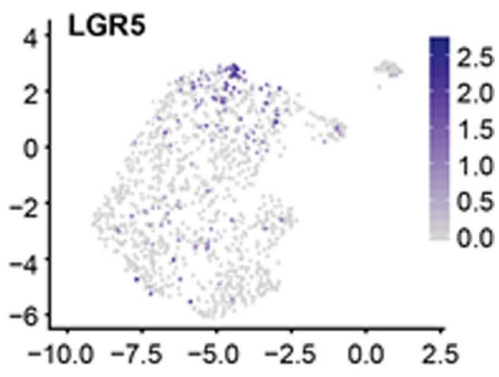
LGR5

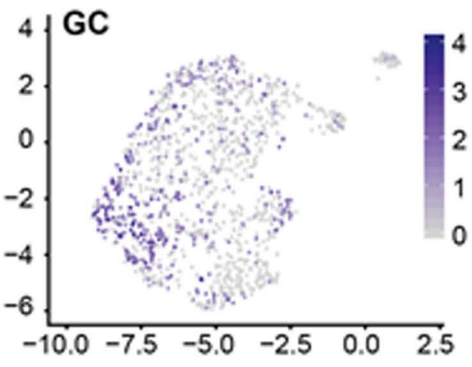
GC

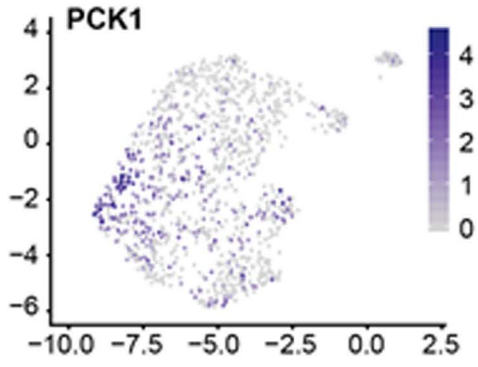
PCK1

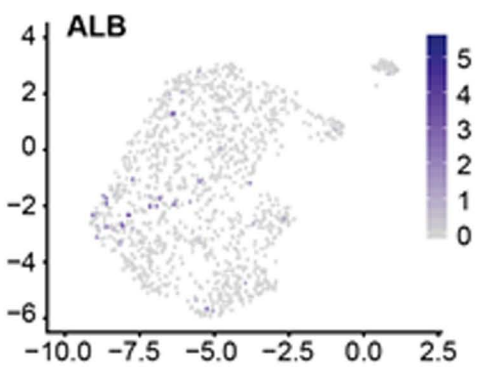
ALB

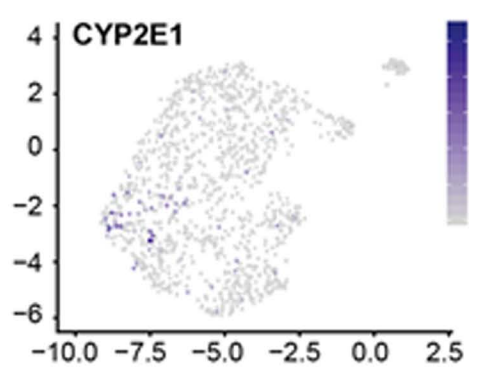
CYP2E1

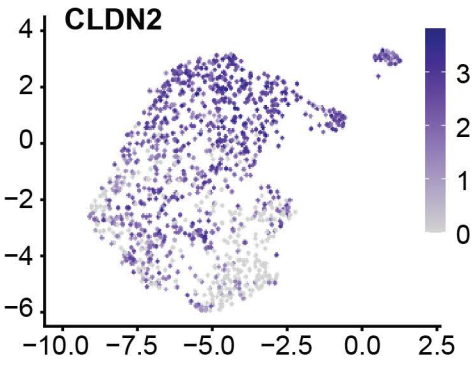
CLDN2

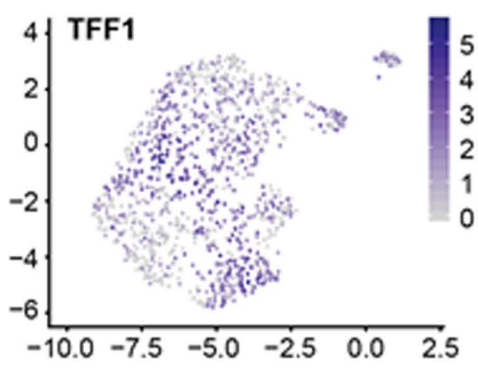
TFF1

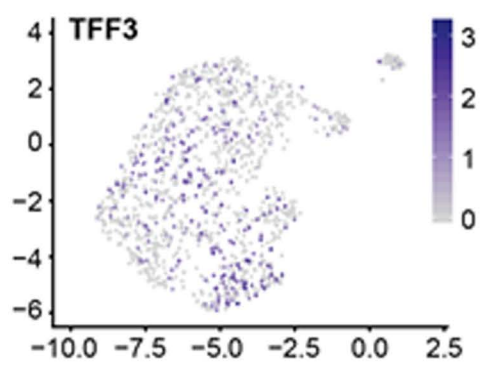
TFF3

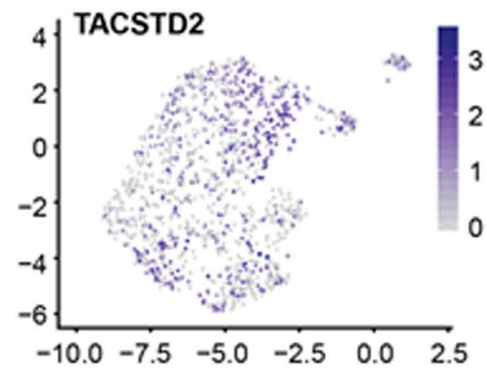
TACSTD2

C

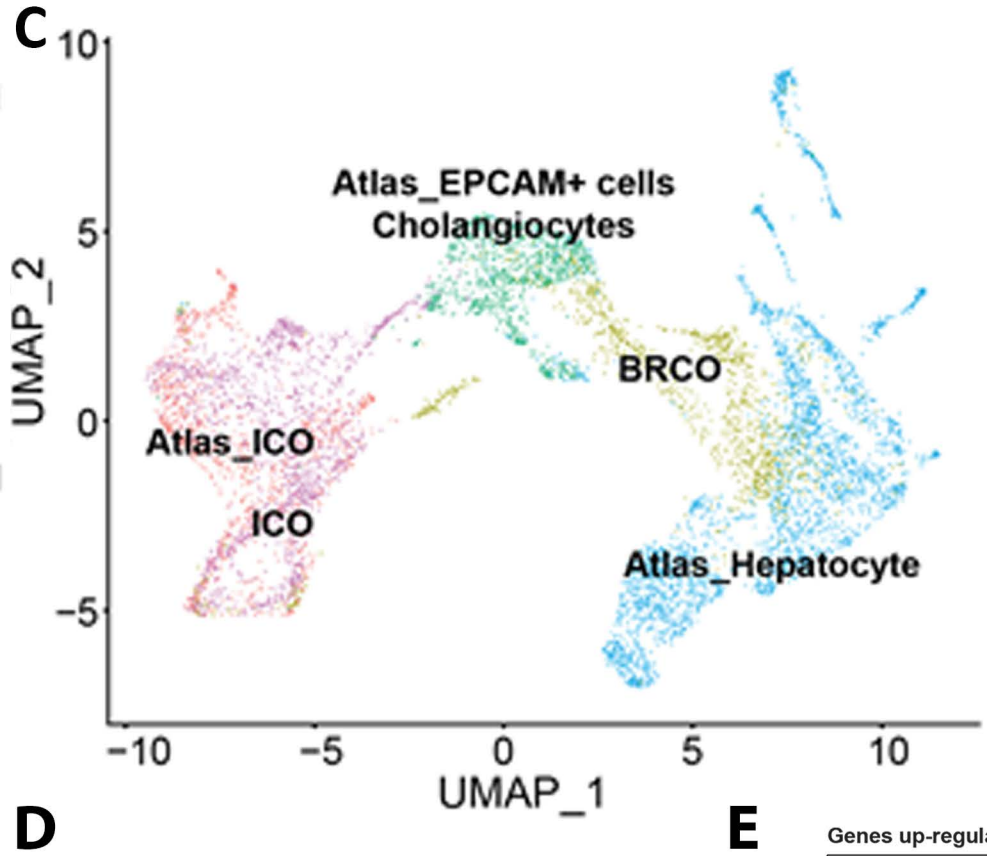
Atlas_EPCAM+ cells
Cholangiocytes
BRCO
Atlas_ICO
ICO
Atlas_Hepatocyte
UMAP_1
UMAP_2

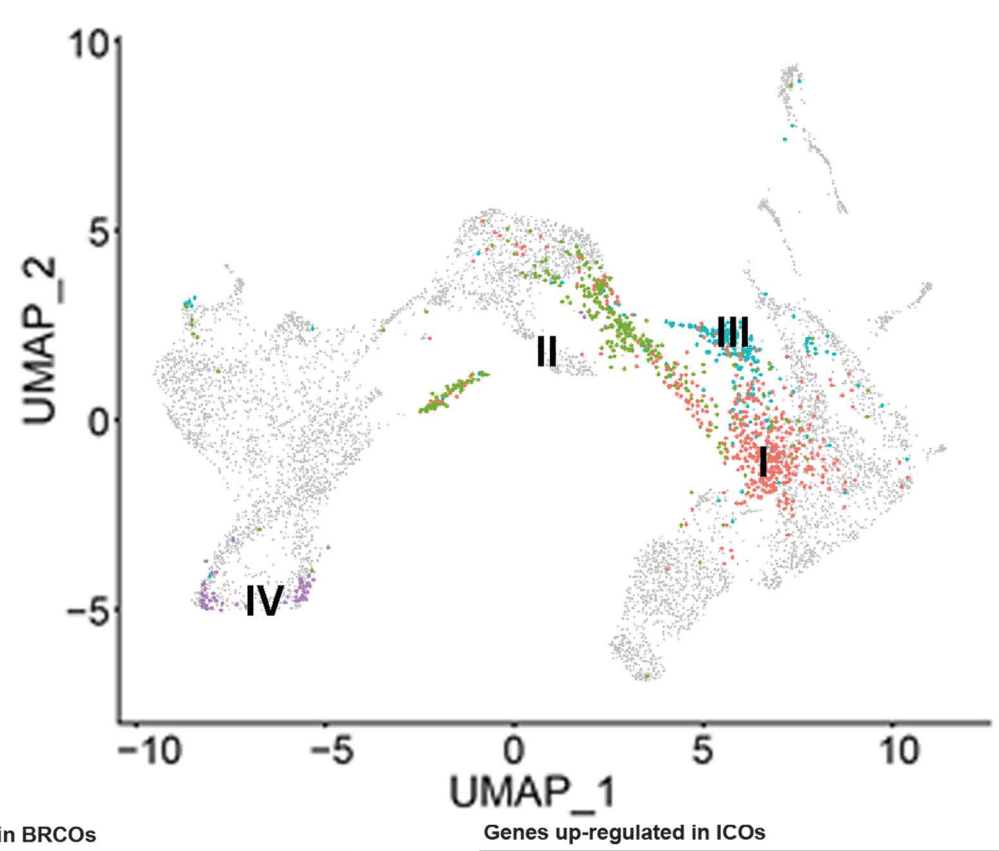
I
II
III
IV
UMAP_1
UMAP_2

D

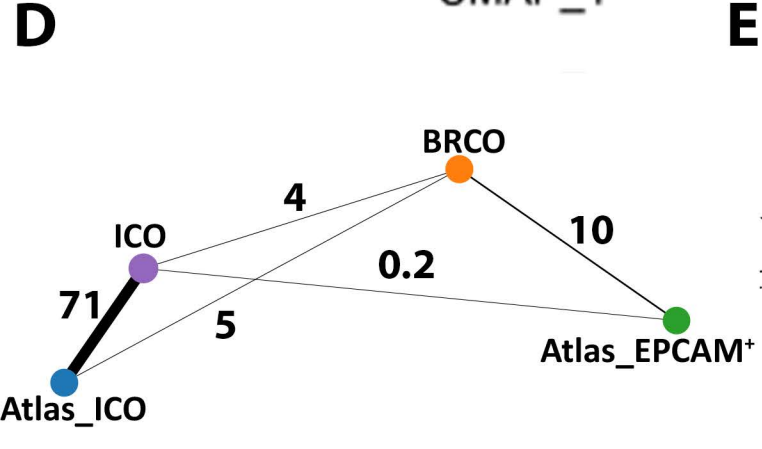
BRCO
ICO
Atlas_ICO
Atlas_EPCAM+
4
10
0.2
71
5

E

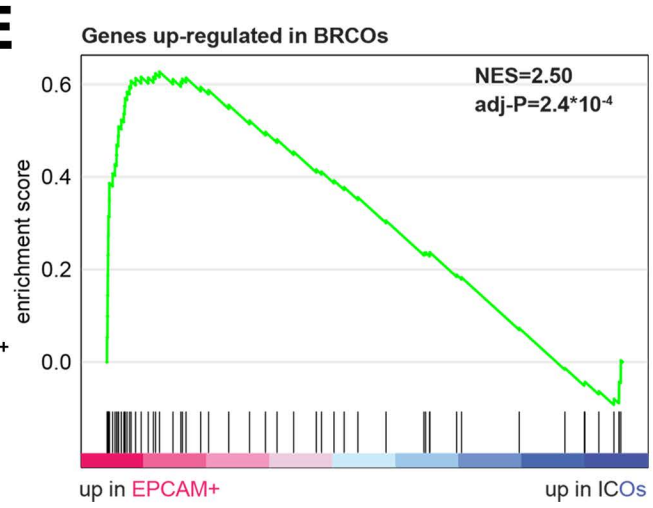
Genes up-regulated in BRCOs
NES=2.50
adj-P=2.4*10-4
enrichment score
up in EPCAM+
up in ICOs

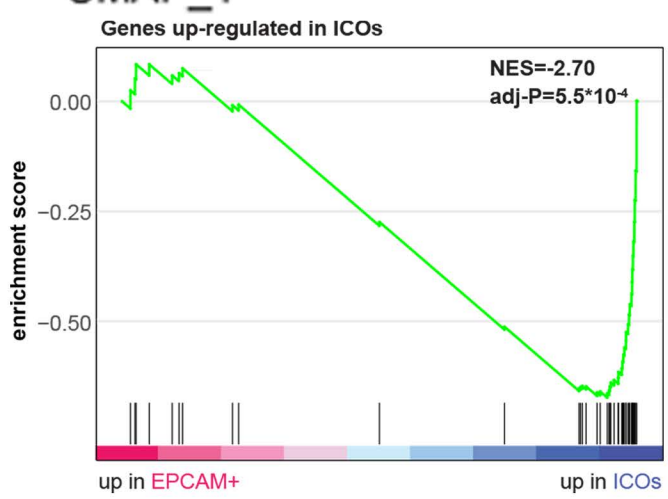
Genes up-regulated in ICOs
NES=-2.70
adj-P=5.5*10-4
enrichment score
up in EPCAM+
up in ICOs

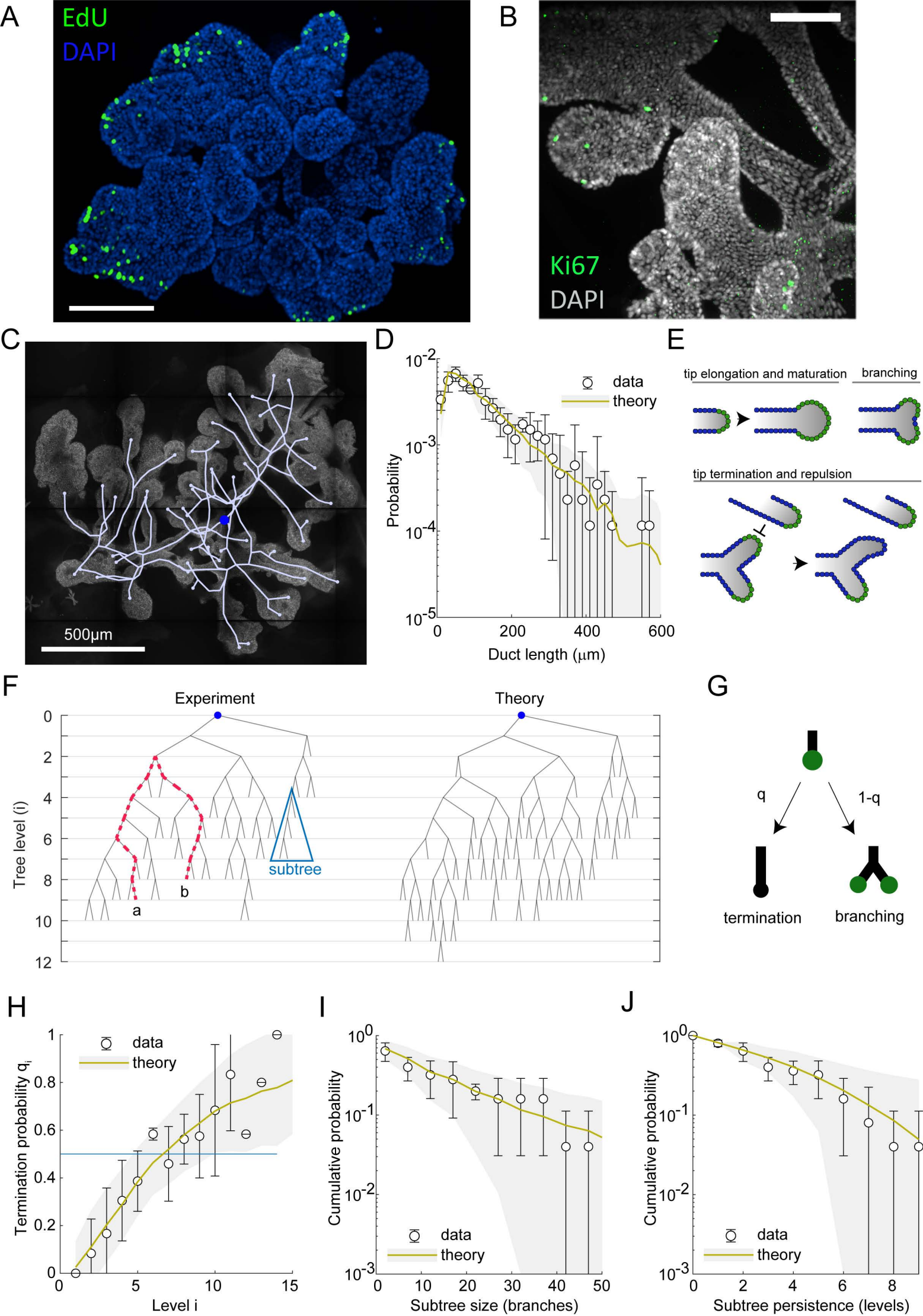
A
EdU
DAPI
B
Ki67
DAPI
C
500μm
D
Probability
data
theory
Duct length (μm)
E
tip elongation and maturation
branching
tip termination and repulsion
F
Experiment
Theory
Tree level (i)
subtree
a
b
G
q
1-q
termination
branching
H
Termination probability q_i
data
theory
Level i
I
Cumulative probability
data
theory
Subtree size (branches)
J
Cumulative probability
data
theory
Subtree persistence (levels)

A

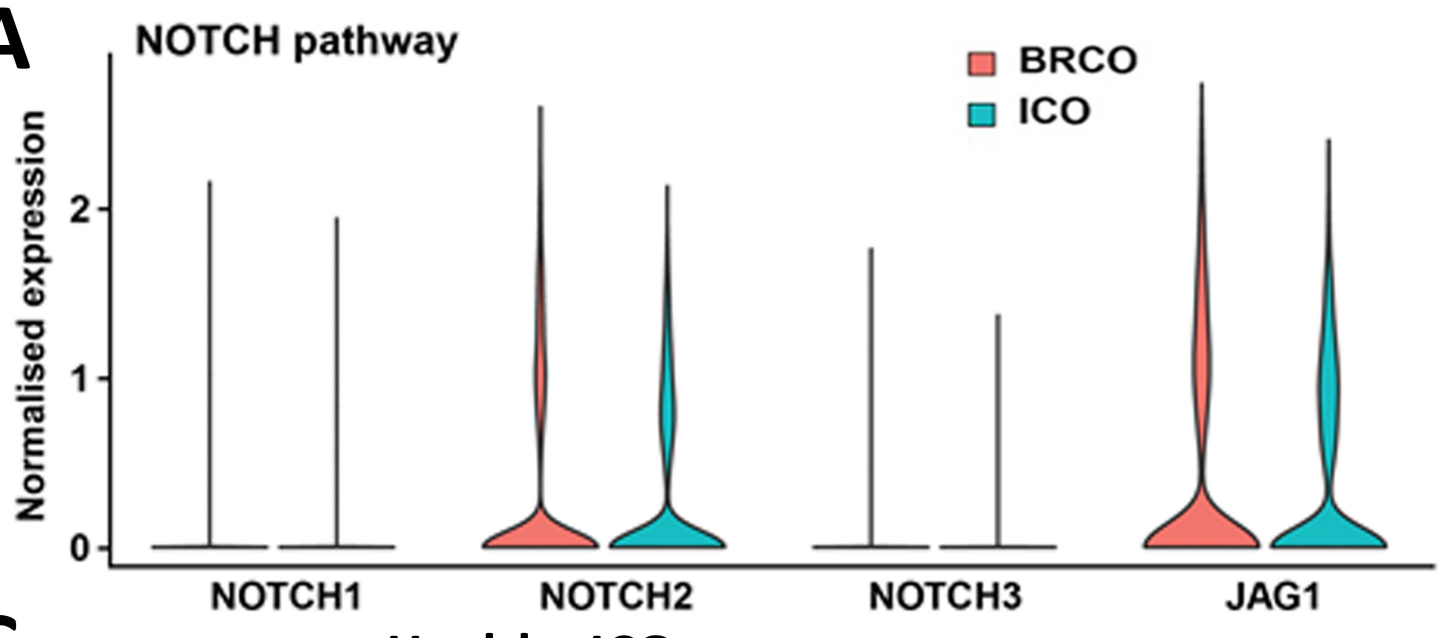
NOTCH pathway
BRCO
ICO
Normalised expression
0
1
2
NOTCH1
NOTCH2
NOTCH3
JAG1

B

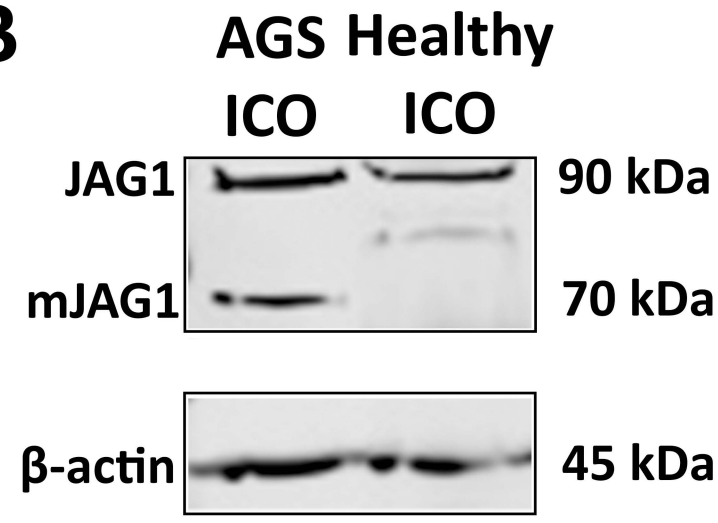
AGS Healthy
ICO
ICO
JAG1
90 kDa
mJAG1
70 kDa
β-actin
45 kDa

C

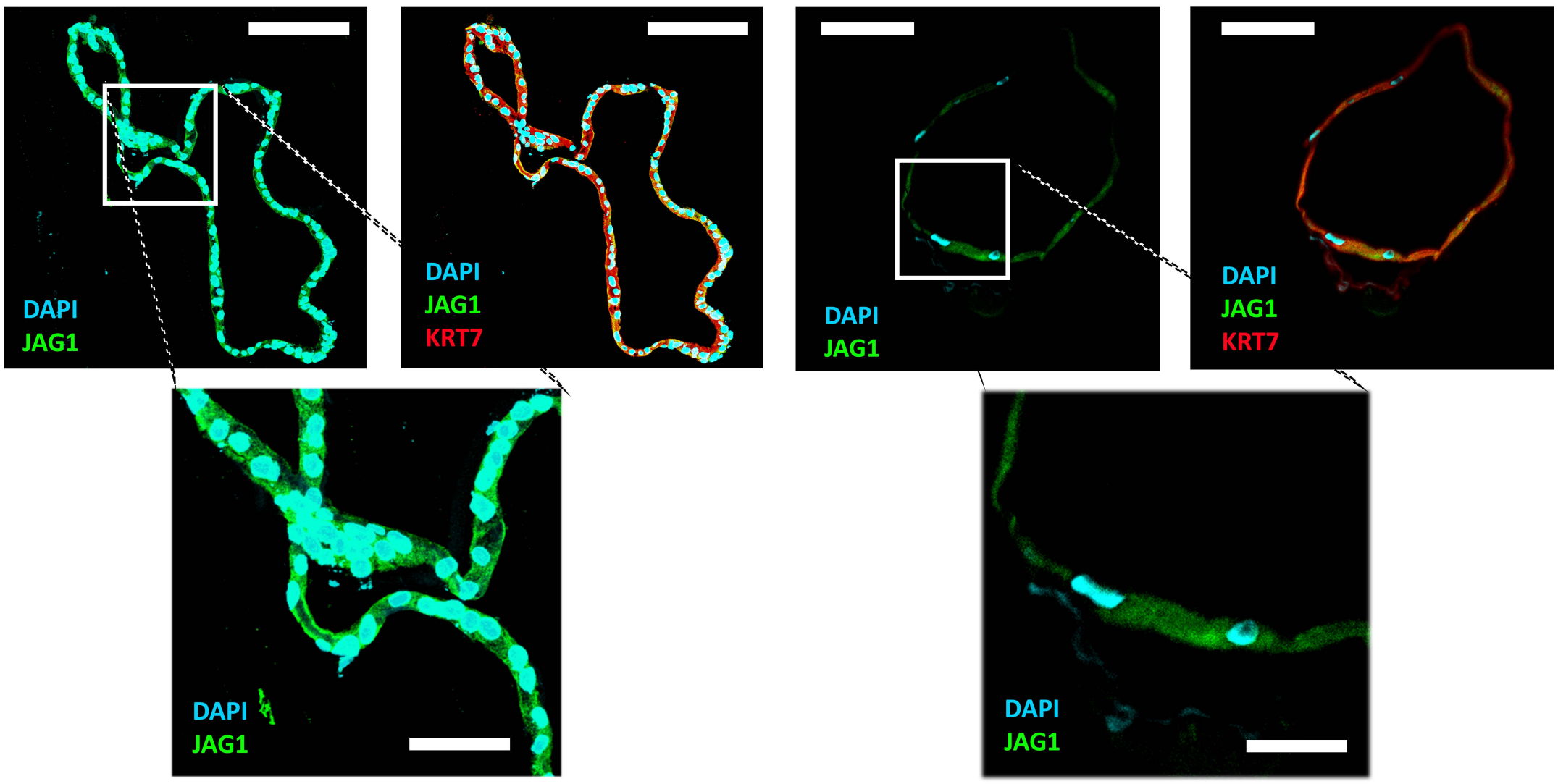
Healthy ICOs
AGS ICOs
DAPI
JAG1
DAPI
JAG1
KRT7
DAPI
JAG1
DAPI
JAG1
KRT7
DAPI
JAG1
DAPI
JAG1

D

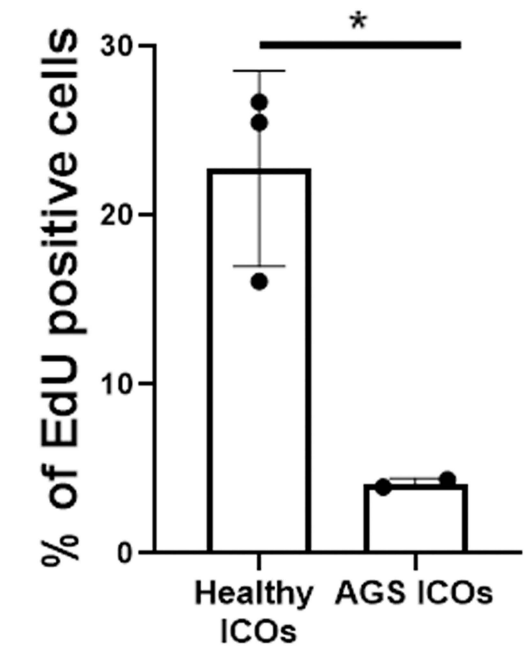
*
% of EdU positive cells
0
10
20
30
Healthy ICOs
AGS ICOs

E

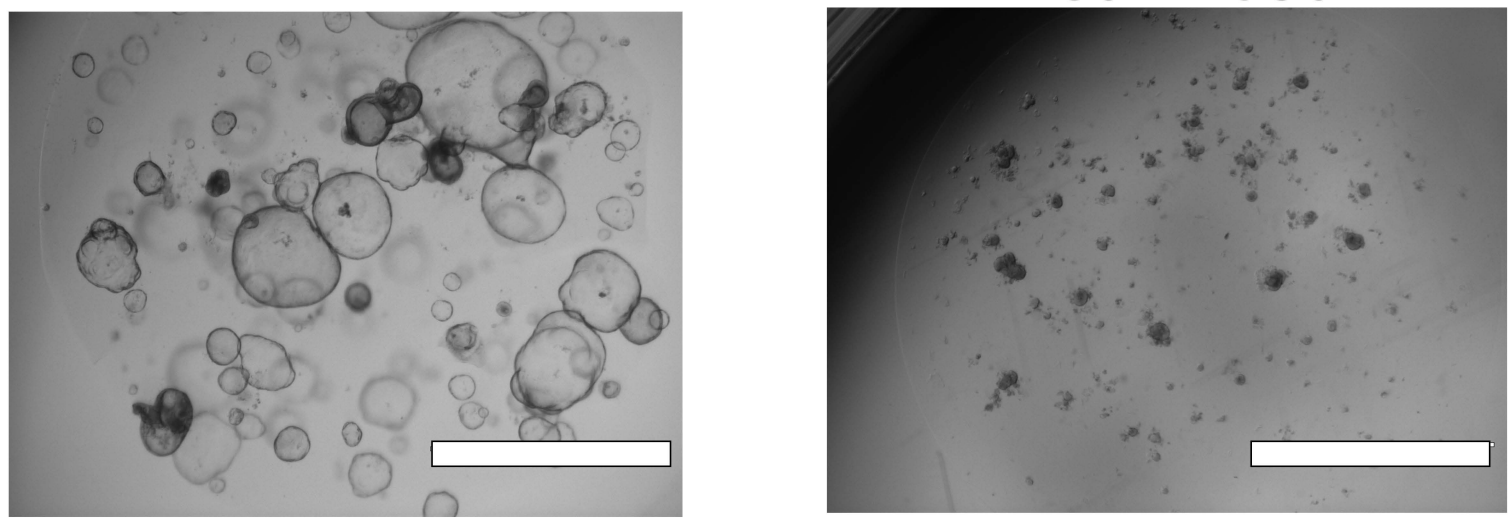
AGS ICOs
AGS BRCOs

F

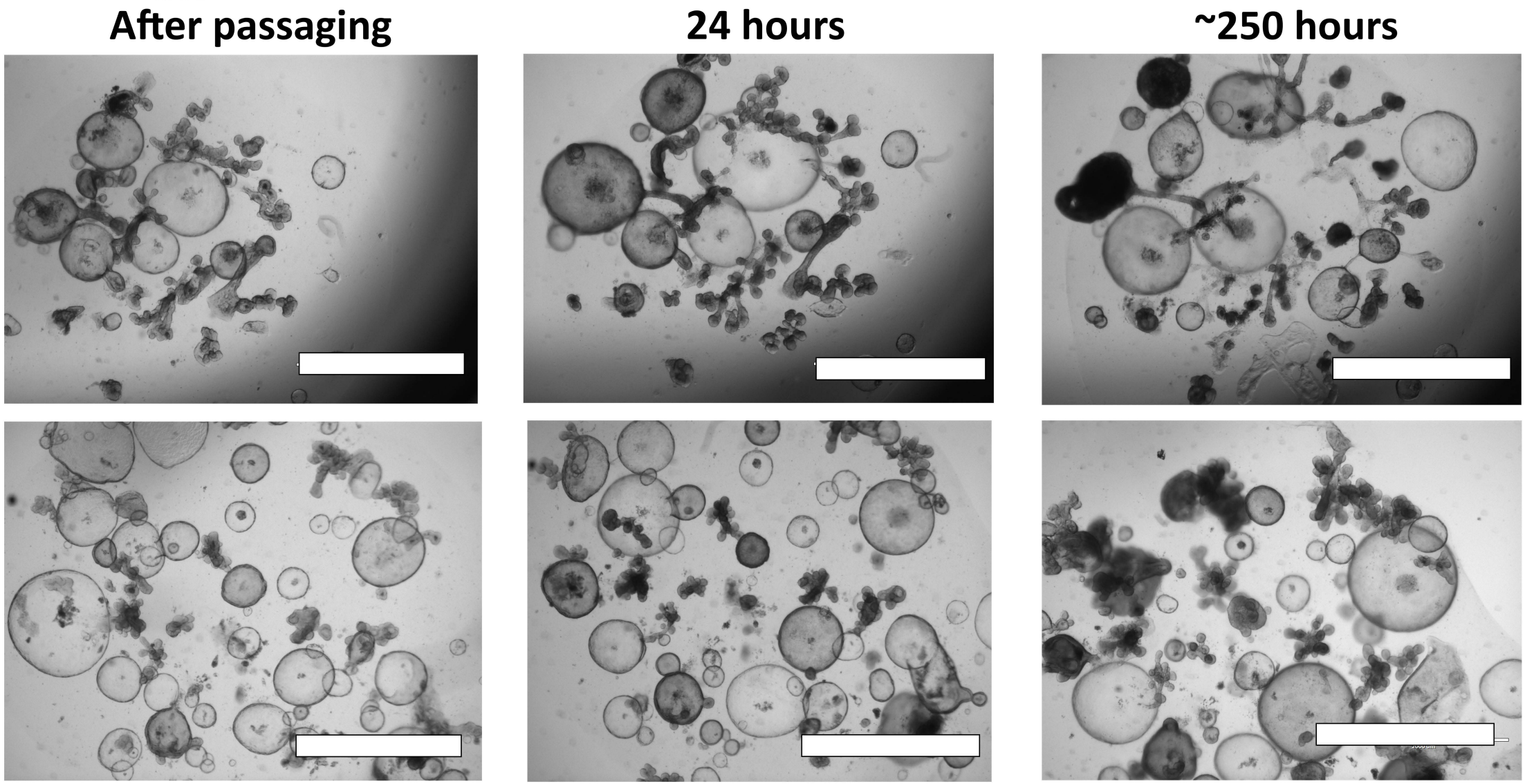
After passaging
24 hours
~250 hours
+ 50µM DAPT
Untreated Control

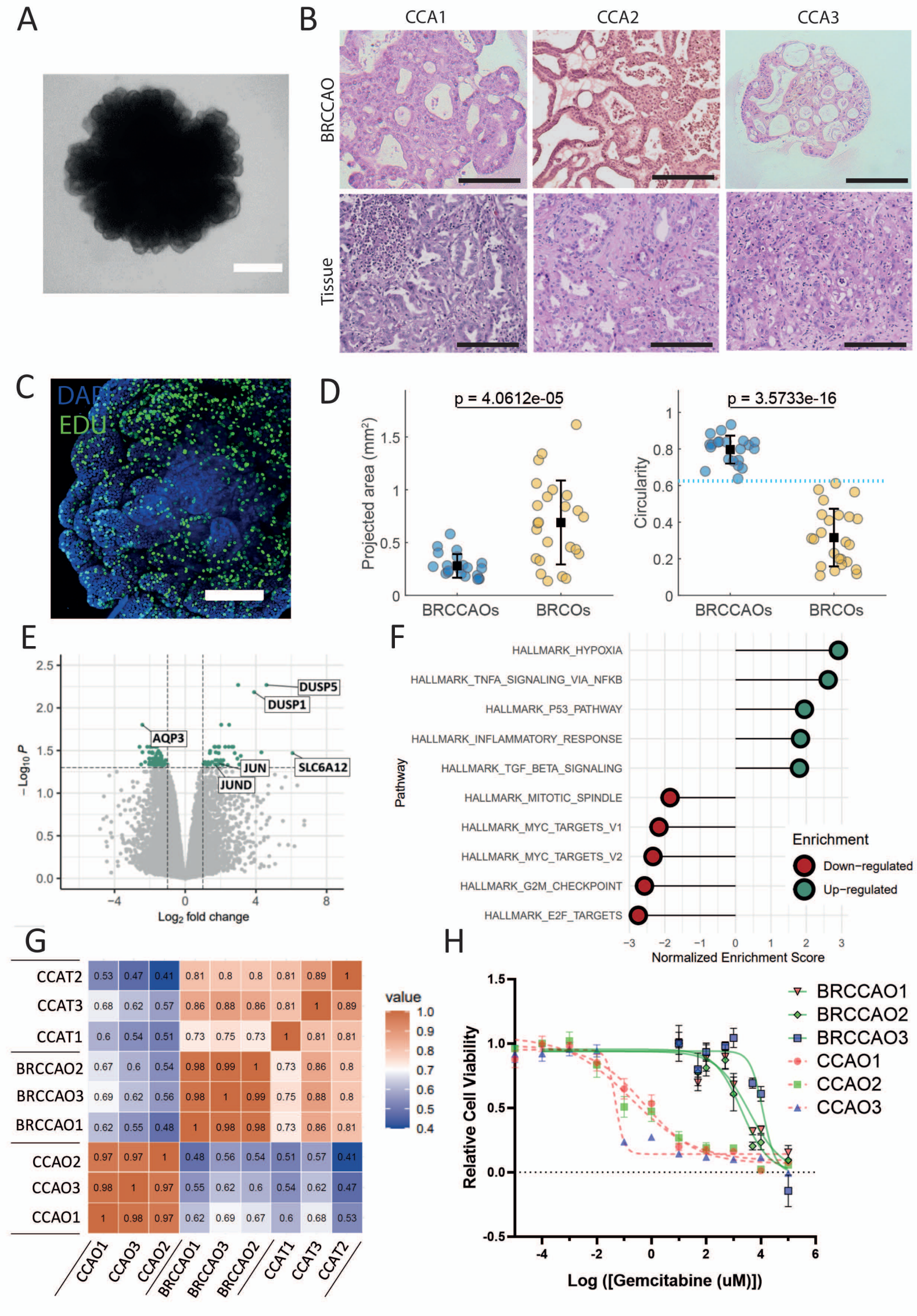
A
B
CCA1
CCA2
CCA3
BRCCAO
Tissue
C
DAPI
EDU
D
p = 4.0612e-05
p = 3.5733e-16
Projected area (mm²)
Circularity
BRCCAOs
BRCOs
E
DUSP5
DUSP1
AQP3
JUN
JUND
SLC6A12
−Log10 P
Log2 fold change
F
HALLMARK_HYPOXIA
HALLMARK_TNFA_SIGNALING_VIA_NFKB
HALLMARK_P53_PATHWAY
HALLMARK_INFLAMMATORY_RESPONSE
HALLMARK_TGF_BETA_SIGNALING
HALLMARK_MITOTIC_SPINDLE
HALLMARK_MYC_TARGETS_V1
HALLMARK_MYC_TARGETS_V2
HALLMARK_G2M_CHECKPOINT
HALLMARK_E2F_TARGETS
Pathway
Enrichment
Down−regulated
Up−regulated
Normalized Enrichment Score
G
CCAT2 0.53 0.47 0.41 0.81 0.8 0.8 0.81 0.89 1
CCAT3 0.68 0.62 0.57 0.86 0.88 0.86 0.81 1 0.89
CCAT1 0.6 0.54 0.51 0.73 0.75 0.73 1 0.81 0.81
BRCCAO2 0.67 0.6 0.54 0.98 0.99 1 0.73 0.86 0.8
BRCCAO3 0.69 0.62 0.56 0.98 1 0.99 0.75 0.88 0.8
BRCCAO1 0.62 0.55 0.48 1 0.98 0.98 0.73 0.86 0.81
CCAO2 0.97 0.97 1 0.48 0.56 0.54 0.51 0.57 0.41
CCAO3 0.98 1 0.97 0.55 0.62 0.6 0.54 0.62 0.47
CCAO1 1 0.98 0.97 0.62 0.69 0.67 0.6 0.68 0.53
CCAO1 CCAO3 CCAO2 BRCCAO1 BRCCAO3 BRCCAO2 CCAT1 CCAT3 CCAT2
value
H
BRCCAO1
BRCCAO2
BRCCAO3
CCAO1
CCAO2
CCAO3
Relative Cell Viability
Log ([Gemcitabine (uM)])

Supplementary Information

Table S1. Patient and organoid culture characteristics.

Culture type	Age patient (years)	Gender	Cell Source	Donor Type/ Surgical Indication	Cultured until passage	Genomic analysis
ICO 1, ECO 1, BRCO 1	67	M	Liver-, EHBD biopsy	DCD	25	No tumor mutations
ICO 2, ECO 2, BRCO 2	75	F	Liver-, EHBD biopsy	DBD	25	No tumor mutations
ICO 3, ECO 3, BRCO 3	47	M	Liver-, EHBD biopsy	DBD	15	No tumor mutations
ICO 4, BRCO 4	65	F	Liver biopsy	DBD	20	n/p
ICO 5, BRCO 5	41	M	Liver biopsy	DBD	15	n/p
ICO 6, BRCO 6	50	M	Liver biopsy	DBD	15	n/p
ICO 7, BRCO 7	80	F	Liver biopsy	DBD	15	n/p
ICO 8, BRCO 8	75	F	Liver biopsy	DBD	10	n/p
ICO 9, BRCO 9	58	M	Liver biopsy	DBD	10	n/p
ICO 10, BRCO 10	22	F	Liver biopsy	DCD	10	n/p
ICO 11, BRCO 11	72	M	Liver biopsy	DBD	10	n/p
ICO 12, BRCO 12	51	F	Liver biopsy	DBD	15	n/p
ICO 13, BRCO 13	72	F	Liver biopsy (explant liver)	Toxic-induced acute liver failure	15	n/p
ICO 14, BRCO 14	43	F	Liver biopsy (explant liver)	Alcoholic induced liver cirrhosis	15	n/p
ICO 15	78	F	Liver biopsy	DBD	15	
ICO 16	50	F	Liver biopsy	DCD	15	
AGS ICO	47	F	Liver biopsy (explant liver)	Alagille Syndrome	15	
Fetal-ICO 1	17-18 weeks	unknown	Fetal Liver	Explant fetal liver	8	
Fetal-ICO 2	17-18 weeks	unknown	Fetal Liver	Explant fetal liver	8	
Fetal-ICO 3	17-18 weeks	unknown	Fetal Liver	Explant fetal liver	7	
CCAO 1, BRCCAO 1	34	F	pCCA	Cholangiocarcinoma (surgical resection specimen)	n/a	
CCAO 2, BRCCAO 2	59	M	iCCA	Cholangiocarcinoma (surgical resection specimen)	n/a	
CCAO 3, BRCCAO 3	76	F	iCCA	Cholangiocarcinoma (surgical resection specimen)	n/a	

Abbreviations. ICO: intrahepatic cholangiocyte organoids, ECO: extrahepatic cholangiocyte organoids, BRCO: branching cholangiocyte organoids, EHBD: extrahepatic bile duct, DCD: donation after circulatory death, DBD: donation after brain death, AGS: Alagille Syndrome, CCAO: cholangiocarcinoma organoid, BRCCAO: Branching cholangiocarcinoma organoid, pCCA: perihilar cholangiocarcinoma, iCCA: intrahepatic cholangiocarcinoma, n/a: not applicable, n/p: not performed.

Table S2. List of genes and primers used.

Gene		Primer sequence (5' à 3')
KRT7	F	GGGGACGACCTCCGGAATAC
	R	CTCAGCCAGGGAGACAGG
GGT	F	TGGTGGACATCATAGGTGGGGA
	R	ATGACGGCAGCACCTCACTT
ASBT	F	GGTGGCCTTTGACATCCTCCC
	R	GCATCATTCCGAGGGCAAGC
SOX9	F	ACCAGTACCCGCACTTGCAC
	R	GCGCCTTGAAGATGGCGTTG
EpCAM	F	GACTTTTGCCGCAGCTCAGGA
	R	AGCAGTTTACGGCCAGCTTGT
CFTR	F	TGGCGGTCACTCGGCAATTT
	R	TCCAGCAACCGCCAACAACT
LGR5	F	GTCAGCTGCTCCCGAATCCC
	R	TGAAACAGCTTGGGGGCACA
CYP3A4	F	AGCAAAGAGCAACACAGAGCTGAA
	R	CAGAGGTGTGGGCCCTGGAAT
TFF1	F	ACAAGCTGCTGTACACGGACA
	R	AAGTTTCCAGGGCCGGGCAAT
MRP2	F	TGGGATGAAAGGTCATCCTTTACGG
	R	GGGGCCAGGAGCCATAGGTA
TACSTD2/TROP2	F	CGAGCTTGTAGGTACCCGGCG
	R	TGCGCCGAGGAATCAGGAAGC
JAG1_exon24	F	TGAATGGACGGATCGCCTGC
	R	TTGTTCGCTGAAGGGGAAGG
JAG1_exon9/10	F	ACAGAAGACGAGCGTGTGGC
JAG1_exon9	F	TCTCCTAATAACTGTTCCCACGG
JAG1_exon11	F	GCCAGTGTCAGAATGACGCCT

Gene		Primer sequence (5'à 3)
SERPINA1	F	GAGGAGAGCAGGAAAGGACA
	R	CTTGGCACGCTGGTTCTTGA
KRT19	F	GCACTACAGCCACTACTACACGA
	R	CTCATGCGCAGAGCCTGTT
TFF2	F	TCTGTCCTGCCTCCCTGATCCA
	R	CTCTGGCACGTGAATCCCGGT
HPRT1	F	TATAAATTCTTTGCTGACCTGCG
	R	CTTCGTGGGGTCCTTTTCACC
ALB	F	CTGCCTGCCTGTTGCCAAAGC
	R	GGCAAGGTCCGCCCTGTCATC
GAPDH	F	CTTTTGCGTCGCCAGCCGAG
	R	CCAGGCGCCCAATACGACCA
HNF4α	F	GTACTCCTGCAGATTTAGCC
	R	CTGTCCTCATAGCTTGACCT
AQP1	F	GGCCAGCGAGTTCAAGAAGAA
	R	TCACACCATCAGCCAGGTCAT
β-catenin	F	GAAAATCCAGCGTGGACAATG
	R	TTGTCAGTTCAGGGATTGC
MUC1	F	CTGTCAGTGCCGCCGAAAGA
	R	CGTGCCCCTACAAGTTGGCA
JAG1_exon11/24	F	GGAGCAAGTCTGGAGACAGCC
	R	TGAATGGACGGATCGCCTGC
JAG1_exon25/26	F	GGCACTGCCAGATAATCCCTCG
JAG1_exon25	R	TCAGCGAGCTGTTTCCATCA
JAG1_exon26	R	ATCCTTGATGGGGACCGTGT
JAG1_e10	F	GCCAAACCTTGTGTAAACGC

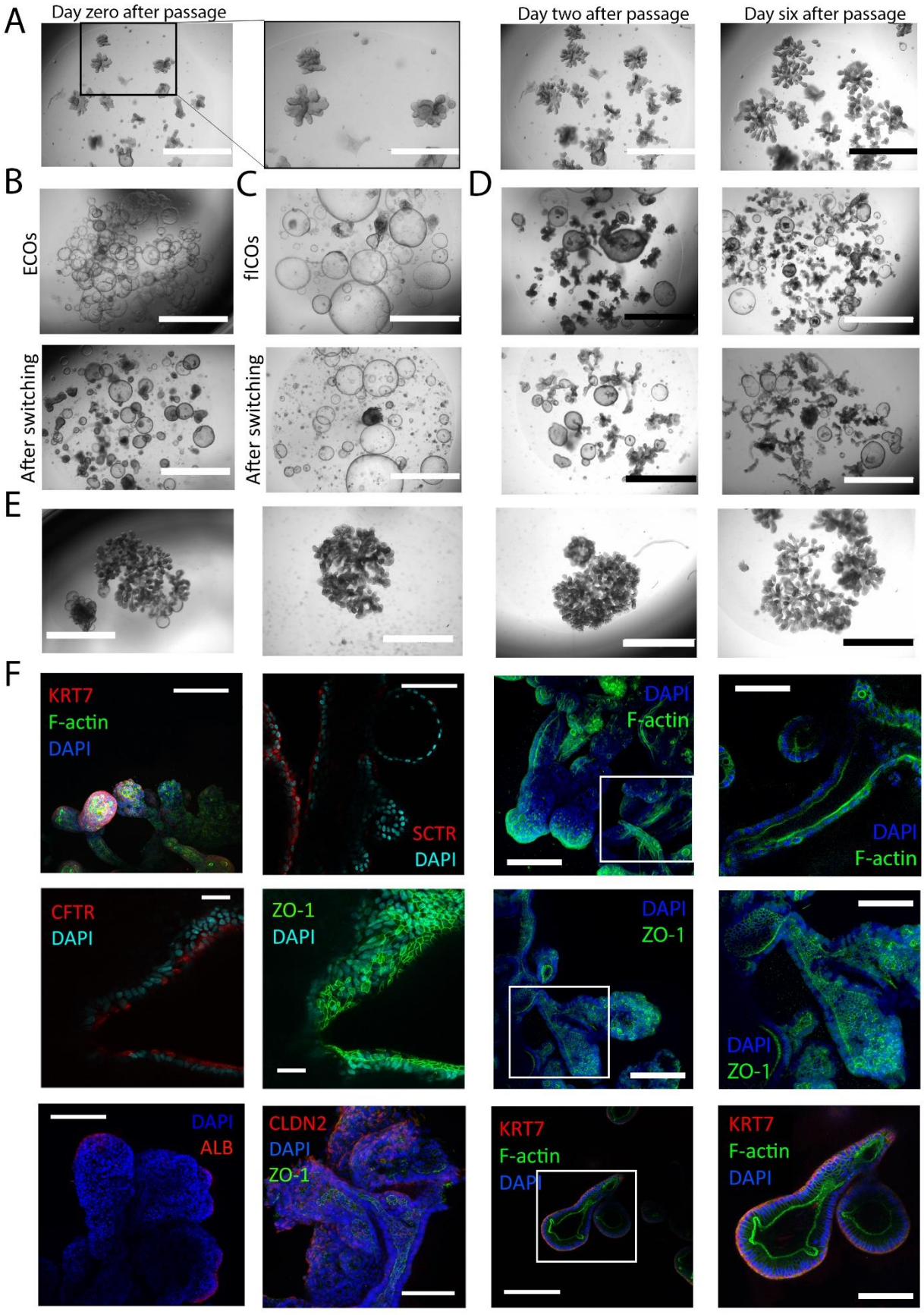
A
Day zero after passage
Day two after passage
Day six after passage
B
ECOs
C
fICOs
D
After switching
After switching
E
F
KRT7
F-actin
DAPI
SCTR
DAPI
DAPI
F-actin
DAPI
F-actin
CFTR
DAPI
ZO-1
DAPI
DAPI
ZO-1
DAPI
ZO-1
DAPI
ALB
CLDN2
DAPI
ZO-1
KRT7
F-actin
DAPI
KRT7
F-actin
DAPI

Figure S1. BRCOs represent complex tubular cholangiocyte organoids that can only be established from intrahepatic cholangiocytes.

(a) Growth of BRCOs after mechanical dissociation. Scale bars indicate 2000 µm and upon zoom 1000 µm. **(b)** Organoids derived from the extrahepatic part of the biliary tree do not form BRCOs after switching (n=3). **(c)** Organoids derived from fetal liver biopsies do not form BRCOs after switching culture conditions (n=3). **(d)** The percentage of BRCOs differs between cultures after switching. **(e)** Different examples of BRCOs from 4 different individual donors (line 1-4), scale bars in a-d represent 2000 µm. **(f)** Whole mount confocal images of BRCOs reveal the presence of polarized cholangiocyte like cells across an open tubular lumen, similar to the *in vivo* situation, scale bars indicate 100 µm except for the zoomed in pictures where it indicates 25 µm. All experiments with ECOs and BRCOs in Figure S2 are performed with lines 1-3.

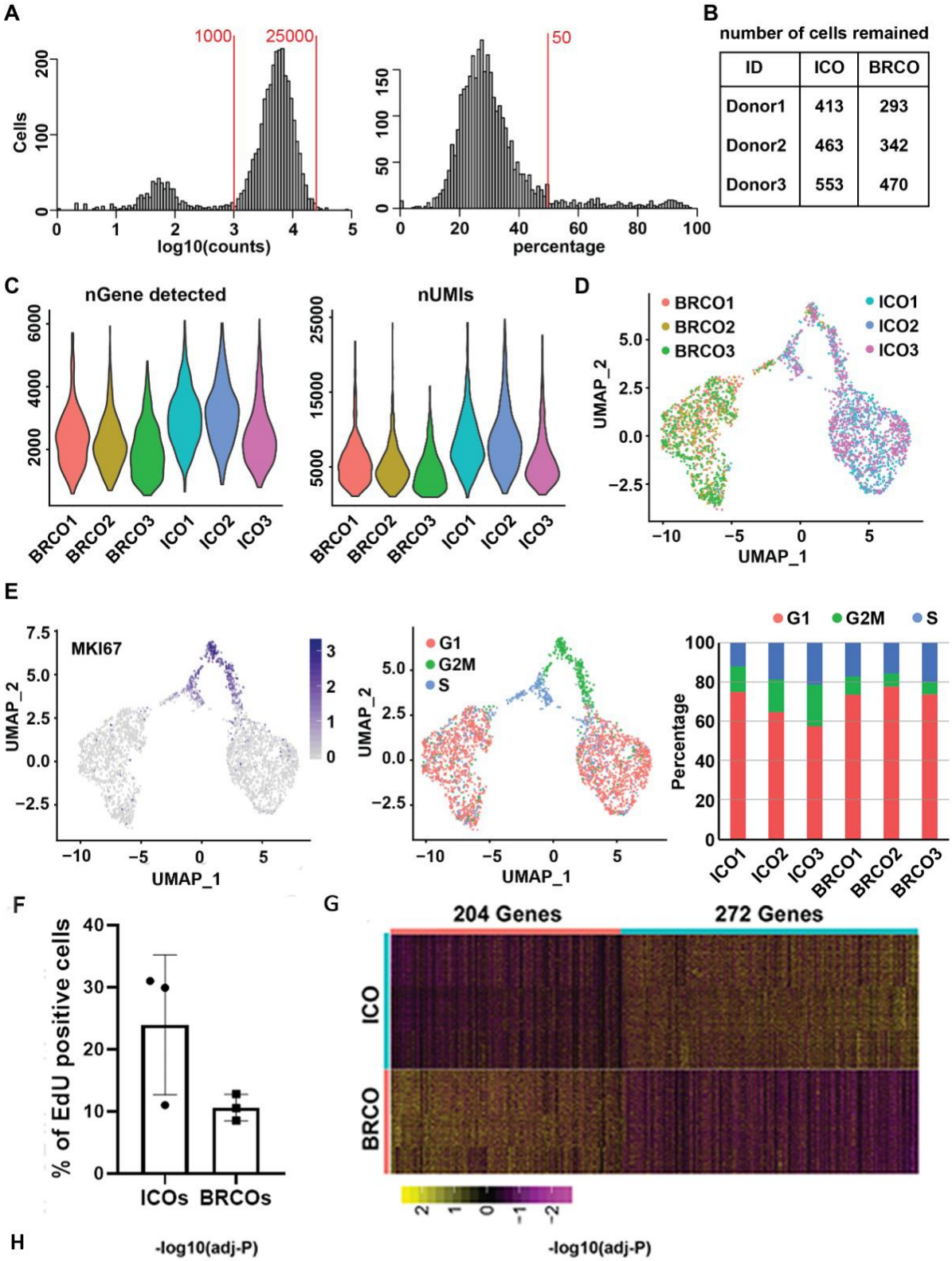
A
1000
25000
50
Cells
log10(counts)
percentage
B
number of cells remained
ID | ICO | BRCO
Donor1 | 413 | 293
Donor2 | 463 | 342
Donor3 | 553 | 470
C
nGene detected
nUMIs
BRCO1
BRCO2
BRCO3
ICO1
ICO2
ICO3
D
UMAP_1
UMAP_2
E
MKI67
G1
G2M
S
Percentage
F
% of EdU positive cells
ICOs
BRCOs
G
204 Genes
272 Genes
ICO
BRCO
H
-log10(adj-P)
regulation of cell proliferation
prostanoid metabolic process
steroid metabolic process
platelet degranulation
prostaglandin metabolic process
regulation of protein localization to Cajal body
positive regulation of protein localization to Cajal body
O-glycan processing
protein O-linked glycosylation
positive regulation of telomerase RNA localization to Cajal body

Figure S2. BRCOs are significantly limited in their proliferation compared to ICOs.

Fig. S2 corresponds to the scRNA-seq experiment as outlined in Fig. **(a)** 3A. Histograms showing the numbers of UMIs (in log10 format) in each cell on the left, and percentage of mitochondrial gene expression per cells on the right. Only the cells following the criteria (1000 < unique transcripts < 25000, MT% < 50%) are used for the analysis. **(b)** Number of ICO and BRCO cells from different donors remained after the filtering. **(c)** Violin plots of numbers of detected genes (on the left) and UMIs (on the right) from both ICOs and BRCOs. Cells are grouped based on the cell types and donors. **(d)** UMAP plot showing the single cells colored by cell types and donors. **(e)** Expression UMAP plot for MKI67 gene. Color bar indicates log2 normalized read counts (on the left). UMAP plot of single cells colored by different cell-cycle phases (G1, G2M, and S phases), and the distribution of cells by cell-cycle phase (on the right). Cells are grouped by cell types and donors. **(f)** Percentage of positive single cells in organoids after 4 hours of EdU incorporation as analyzed by flow cytometry on paired BRCO and ICO samples (n=3). **(g)** Heatmap of the differentially expressed genes up-regulated in BRCOs (n=204 genes) and ICOs (n=272 genes). **(h)** GO analysis (biological process) for the same gene sets from the DE gene analysis. Only the top five most significant pathways are listed here.

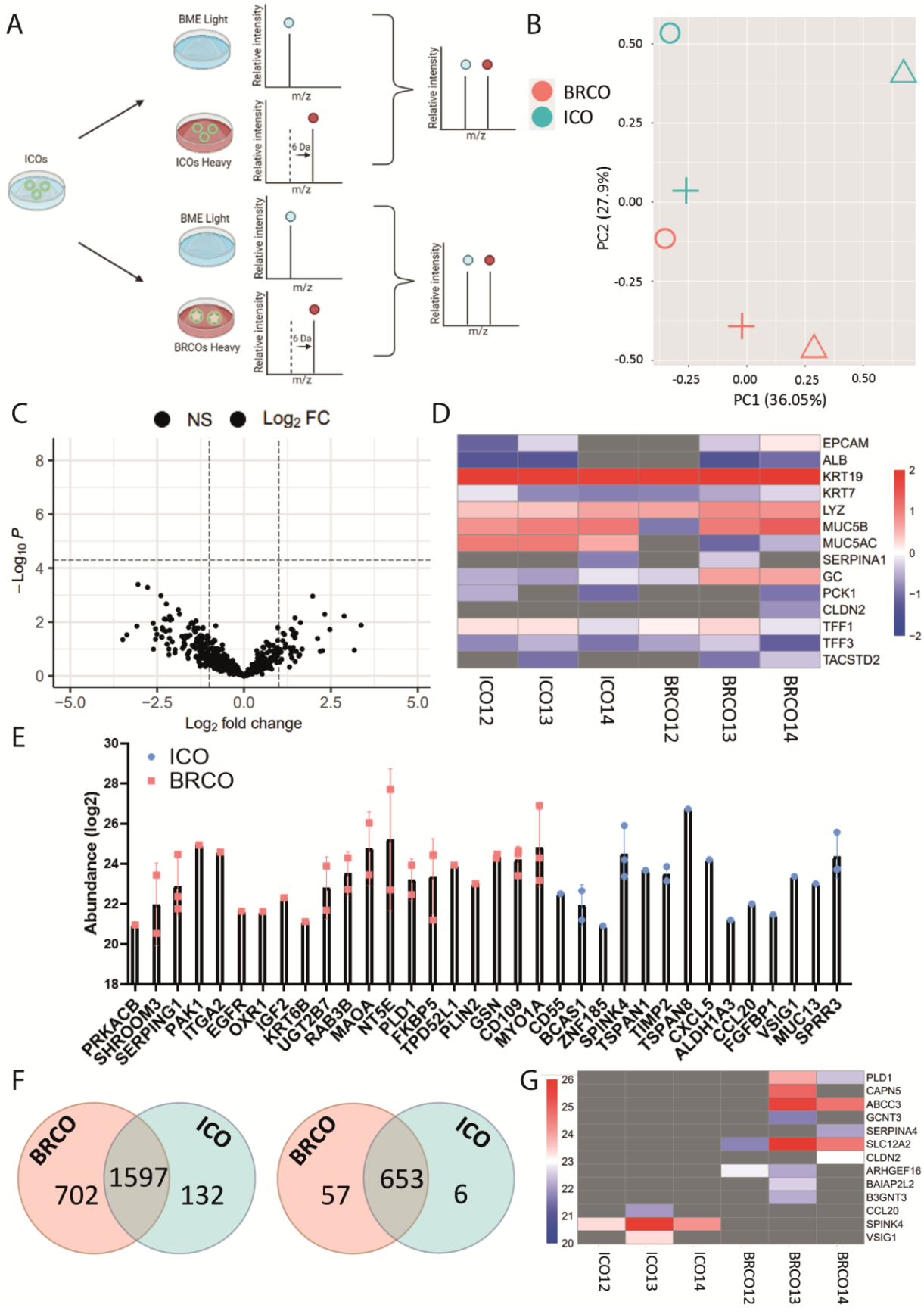
A
BME Light
ICOs
ICOs Heavy
BME Light
BRCOs Heavy
Relative intensity
m/z
6 Da
B
BRCO
ICO
PC2 (27.9%)
PC1 (36.05%)
C
NS
Log2 FC
−Log10 P
Log2 fold change
D
EPCAM
ALB
KRT19
KRT7
LYZ
MUC5B
MUC5AC
SERPINA1
GC
PCK1
CLDN2
TFF1
TFF3
TACSTD2
ICO12
ICO13
ICO14
BRCO12
BRCO13
BRCO14
E
ICO
BRCO
Abundance (log2)
PRKACB
SHROOM3
SERPING1
PAK1
ITGA2
EGFR
OXR1
IGF2
KRT6B
UGT2B7
RAB3B
MAOA
NT5E
PLD1
FKBP5
TPD52L1
PLIN2
GSN
CD109
MYO1A
CD55
BCAS1
ZNF185
SPINK4
TSPAN1
TIMP2
TSPAN8
CXCL5
ALDH1A3
CCL20
FGFBP1
VSIG1
MUC13
SPRR3
F
BRCO
ICO
702
1597
132
BRCO
ICO
57
653
6
G
PLD1
CAPN5
ABCC3
GCNT3
SERPINA4
SLC12A2
CLDN2
ARHGEF16
BAIAP2L2
B3GNT3
CCL20
SPINK4
VSIG1
ICO12
ICO13
ICO14
BRCO12
BRCO13
BRCO14

Figure S3. Protein expression analyzed by SILAC reveals differences between BRCOs and ICOs.
(a) Schematic overview of the experiment. **(b)** PCA plot displaying overall protein abundance values of paired BRCOs and ICOs. Intensity values were transformed using variance stabilizing transformation before plotting. The different shapes represent different organoid lines. Only proteins present in all conditions were taken into consideration. **(c)** A volcano scatter plot of statistical significance (adj. P-value <0.05) vs. magnitude of change (Log2FC) showing no overall DE proteins present between BRCOs and ICOs. Only proteins present in all conditions were used for analysis. **(d)** Heatmap showing protein abundance levels of previously described cholangiocyte (organoid) markers (EPCAM, KRT19, KRT7, LYZ, MUC5B, TACSTD2, TFF1, and TFF3) and hepatocyte related markers (ALB, GC, PCK1, and SERPINA1). All data was transformed and z-scored per sample (see legend). Grey values represent non-detected protein levels in the sample. **(e)** Interleaved scatter plot of matched exclusive proteins and DE Genes from the scRNAseq analysis (Fig. 3A) for both BRCOs and ICOs. Each dot represents an overlap in that particular gene and corresponding protein for a sample. **(f)** Protein overlaps and exclusivity when applying loose criteria (present in 1 of 3 samples, not present in 3 of 3 samples of other group, left) and stringent criteria (present in 3 of 3 samples, not present in 3 of 3 samples of another group, right). **(g)** Uniquely produced proteins according to loose criteria in BRCOs and ICOs, correlated to DE proteins in primary cholangiocytes (from the gallbladder) as previously described.[26] All experiments performed in this figure are with lines 12-14 (3 biological replicates for ICOs and BRCOs).

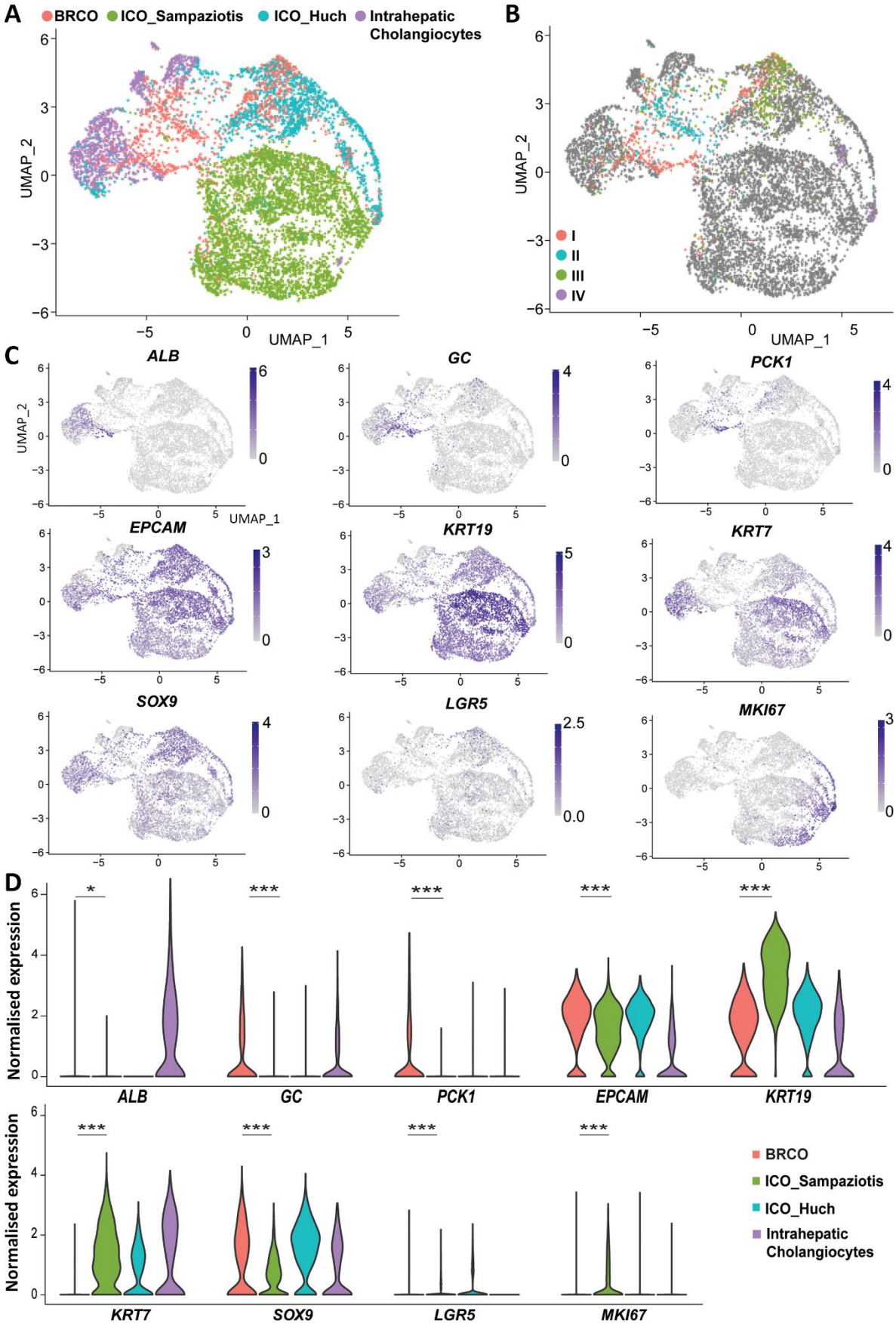
A
BRCO
ICO_Sampaziotis
ICO_Huch
Intrahepatic Cholangiocytes
UMAP_2
UMAP_1
B
I
II
III
IV
C
ALB
GC
PCK1
EPCAM
KRT19
KRT7
SOX9
LGR5
MKI67
D
Normalised expression
ALB
GC
PCK1
EPCAM
KRT19
KRT7
SOX9
LGR5
MKI67
BRCO
ICO_Sampaziotis
ICO_Huch
Intrahepatic Cholangiocytes

Figure S4. scRNAseq. demonstrate transcriptomic differences between BRCOs and ICOs.
(a) UMAP plots of single cells isolated from ICOs cultured according to Huch *et al.* [7] (n=3, ICO_Huch, Fig. 3), BRCOs (n=3, Fig. 3), and integrated with the scRN-Aseq data from Sampaziotis *et al.*[29] consisting of ICOs cultured according to Tysoe *et al*.[12] (n=1, ICO_Sampaziotis) and donor matched intrahepatic cholangiocytes (n=1). Cells colored by different cell types (on top). **(b)** UMAP plots of the different clusters present in BRCOs (cluster I-IV) of Figure 4B, and color-matched according to Figure 4B. **(c)** UMAP plots showing expression levels of previously described cholangiocyte organoid markers (*EPCAM*, *SOX9*, *KRT19* and *KRT7*), WNT-target gene *LGR5*, proliferation marker *Ki67* and hepatocyte related markers (*ALB*, *GC* and *PCK1*). **(d)** Expression violin plot showing the transcription levels of the selected genes in **c**. Only transcriptomic differences between ICO_Sampaziotis and BRCOs are shown. * P<0.05, *** p<0.001 by Wilcox test.

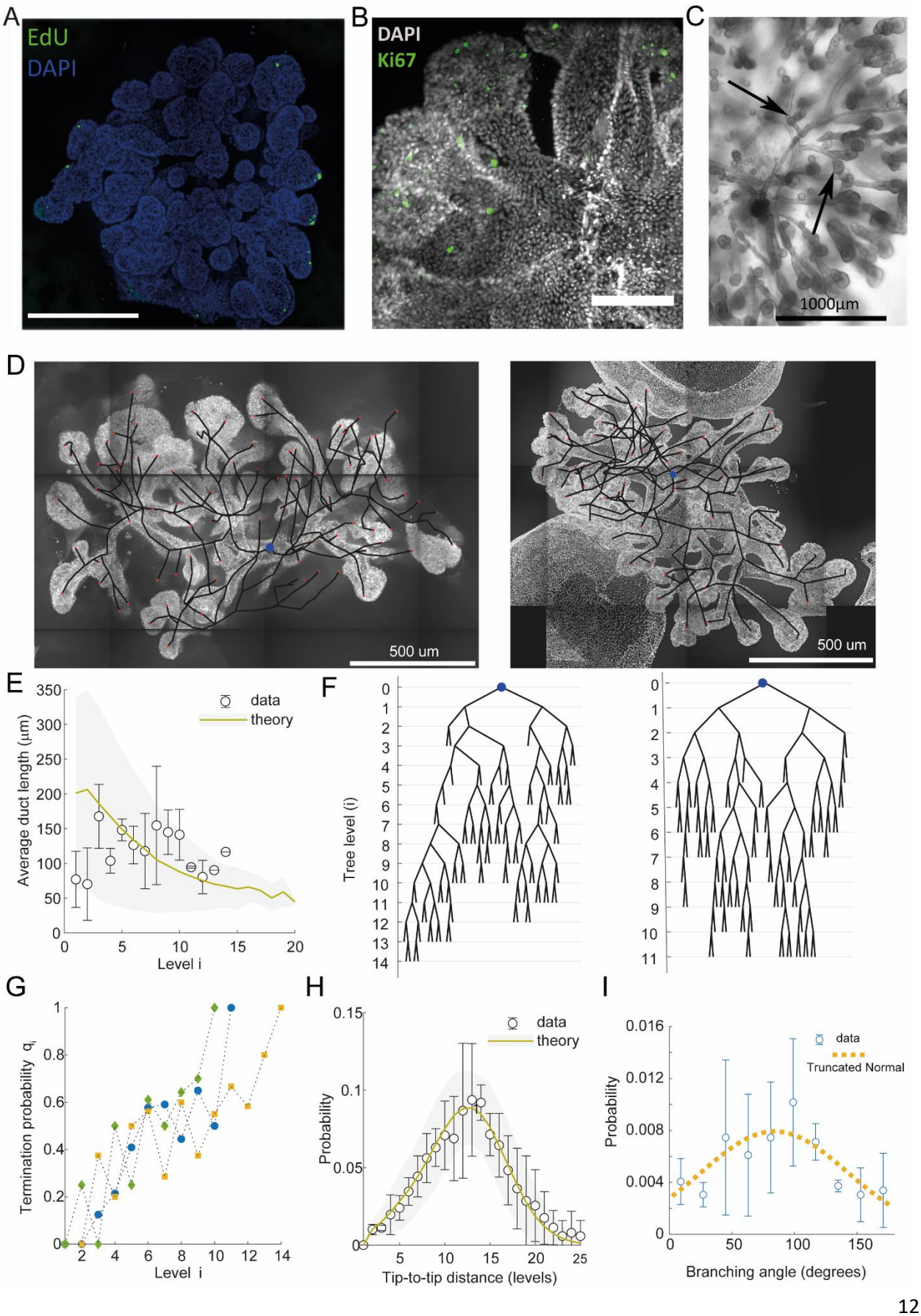
A
EdU
DAPI
B
DAPI
Ki67
C
1000μm
D
500 um
500 um
E
data
theory
Average duct length (μm)
Level i
F
Tree level (i)
G
Termination probability q_i
Level i
H
data
theory
Probability
Tip-to-tip distance (levels)
I
data
Truncated Normal
Probability
Branching angle (degrees)

Figure S5. BRCOs network reconstruction and statistics.

Fig. S5 provides additional analysis and data corresponding to Fig. 5. **(a-b)** Max-projection of confocal image of EdU (green) incorporation and Ki67 (green). Nuclei are counterstained with DAPI (blue and grey), and scale bars indicate 500µm (left) and 200 µm (right). **(c)** Close-up of the internal ductal structure of a BRCO, with arrows indicating arrested tips. **(d)** Single z-slice of two 3D confocal BRCO images overlaid with the full reconstructed ductal networks (grey lines), and the position identified as the sources are indicated in blue. **(e)** Average duct-length as a function of the level in the tree. Black markers indicate the average and SD from n = 3 repeats. The model predictions are shown in yellow and its SD by the shaded area. **(f)** Branching tree corresponding to the organoids shown in panels **(d)**, with the left tree corresponding to the left organoid and the right to the right. **(g)** Termination probability as a function of the level in the tree, for each independent repeat (see average and SD in Fig. 5H). **(h)** Tip-to-tip node distance distribution, measured in levels (see Fig. 5F), obtained from experiments (black, error bars show the SD), and model (yellow, shaded area is SD), R^2=0.97. **(i)** Distribution of angles formed by two offspring branches, measured from n=3 samples, showing a peak around 95 degrees. All experiments conducted in this figure are performed on BRCO 10 and a technical duplicate of BRCO 9.

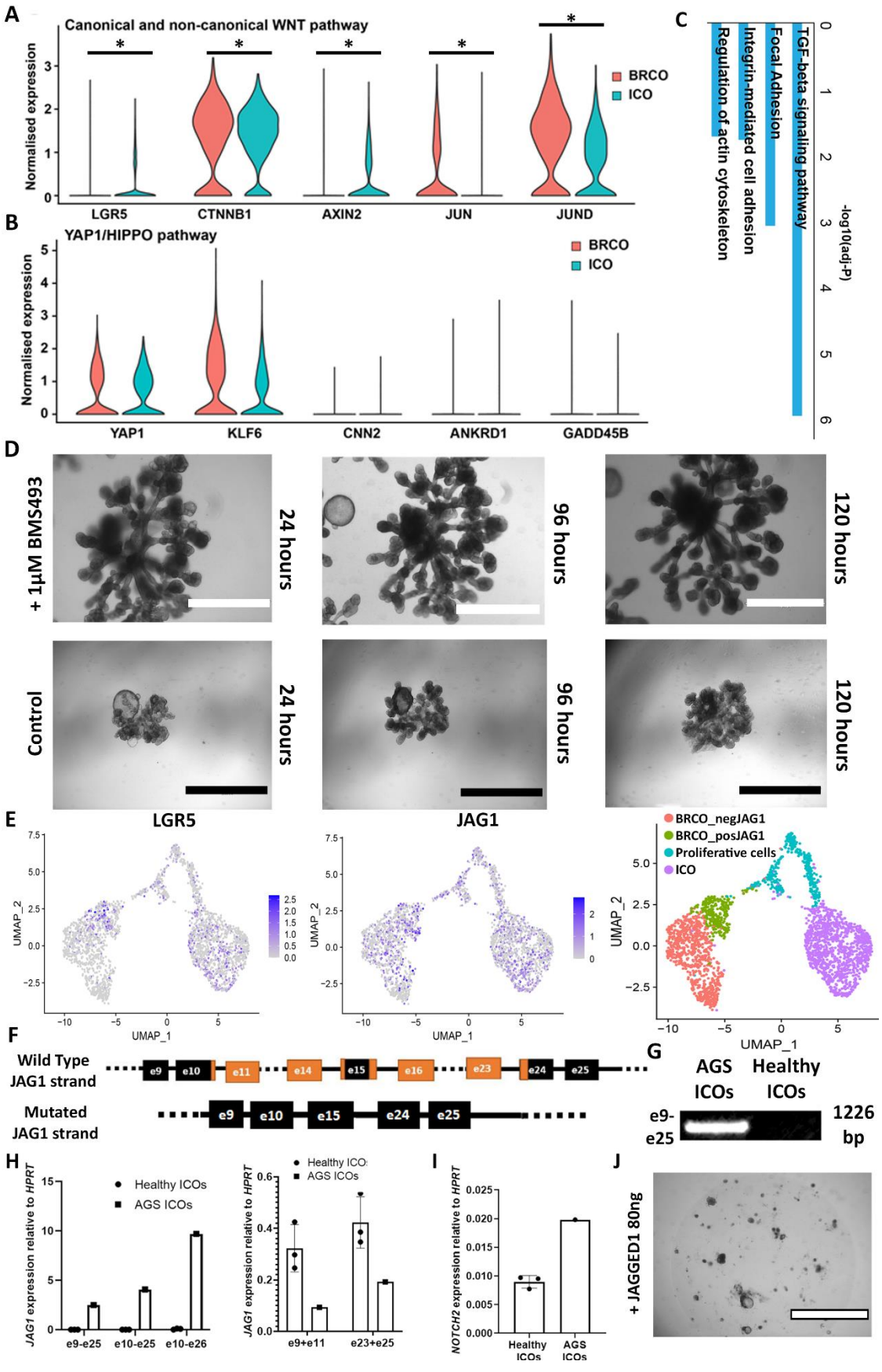
A
Canonical and non-canonical WNT pathway
Normalised expression
BRCO
ICO
LGR5
CTNNB1
AXIN2
JUN
JUND
B
YAP1/HIPPO pathway
Normalised expression
BRCO
ICO
YAP1
KLF6
CNN2
ANKRD1
GADD45B
C
Regulation of actin cytoskeleton
Integrin-mediated cell adhesion
Focal Adhesion
TGF-beta signaling pathway
-log10(adj-P)
D
+ 1µM BMS493
Control
24 hours
96 hours
120 hours
E
LGR5
JAG1
UMAP_1
UMAP_2
BRCO_negJAG1
BRCO_posJAG1
Proliferative cells
ICO
F
Wild Type JAG1 strand
Mutated JAG1 strand
e9
e10
e11
e14
e15
e16
e23
e24
e25
G
AGS ICOs
Healthy ICOs
e9-e25
1226 bp
H
JAG1 expression relative to HPRT
Healthy ICOs
AGS ICOs
e9-e25
e10-e25
e10-e26
e9+e11
e23+e25
I
NOTCH2 expression relative to HPRT
Healthy ICOs
AGS ICOs
J
+ JAGGED1 80ng

Figure S6. Pathways important for branching in BRCOs.

(a-b) Violin plots showing the expression of selected genes involved in different pathways (*LGR5*, *CTNNB1*, *AXIN2*, *JUN*, and *JUND* from WNT pathway; *YAP1*, *KLF6*, *CNN2*, *ANKRD1*, and *GADD45B* from YAP1/HIPPO pathway). Cells were grouped based on the cell types. **(c)** Cytoskeletal pathway analysis of ICOs and BRCOs (n=3) obtained via scRNAseq. **(d)** BMS493 addition (1µM) does not inhibit branching 120 hours of culture, scale bars indicate 1000 µm (top row). In the bottom row, the control line is displayed, here scale bars indicate 2000 µm. **(e)** Expression UMAP plot for *LGR5* and *JAG1*. Color bar indicates log2 normalized read counts (on the left and middle). On the right UMAP plot for *JAG1* colored coded by different cell types, cell cycle status and expression of *JAG1* in clusters of BRCOs (green corresponds to cluster 3 and orange to cluster 2 and 4 of Figure 3B). **(f)** Both *JAG1* strands of the AGS patient. Black squared indicate exons that are present in the healthy and the mutated JAG1 strand and orange exons are solely present in the healthy. Introns are as black (dashed) lines. **(g)** Gel electrophoresis of the *mJAG1* PCR product in AGS ICOs (left) and healthy ICOs (right). **(h)** JAG1 expression of specific exons in healthy (n=3) and AGS ICOs relative to *HPRT*. **(i)** qPCR of *NOTCH2* in healthy ICOs (n=3) compared to AGS ICOs relative to *HPRT*, e indicates exon. **(j)** Chimeric JAGGED1 addition (80 ng) towards culture media does not result in formation of BRCOs in the AGS patient after switching culture conditions. Scale bar indicates 2000 µm. Experiments in panel a-c and e (scRNAseq) are performed with ICOs and BRCO 6,7 and 10. Panel d with ICOs and BRCOs 7-9 and g-i with ICO 12, 15 and 16. * P<0.05 by Wilcox test.

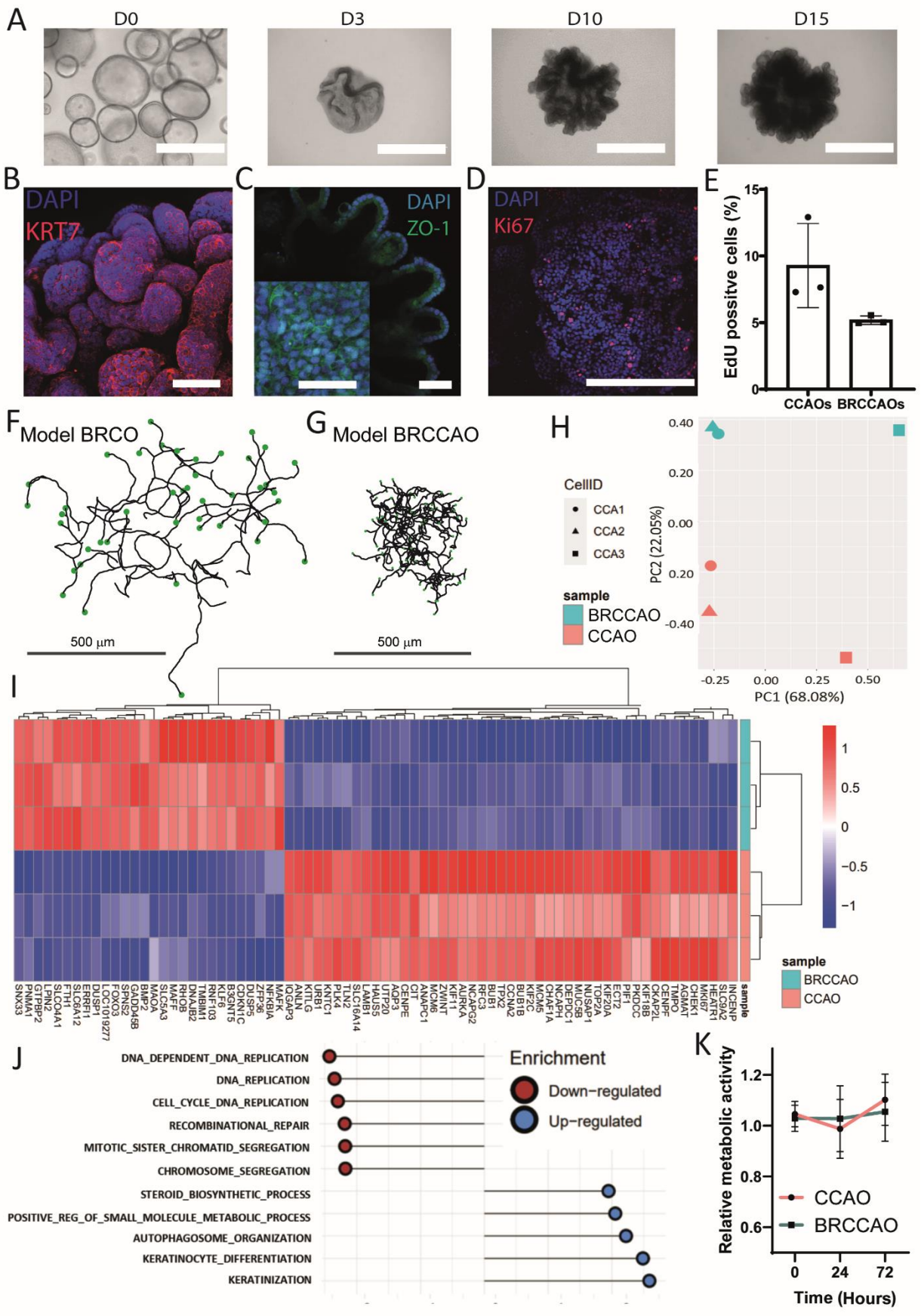
A
D0
D3
D10
D15
B
DAPI
KRT7
C
DAPI
ZO-1
D
DAPI
Ki67
E
EdU possitive cells (%)
CCAOs
BRCCAOs
F
Model BRCO
500 μm
G
Model BRCCAO
500 μm
H
CellID
CCA1
CCA2
CCA3
sample
BRCCAO
CCAO
PC2 (22.05%)
PC1 (68.08%)
I
sample
BRCCAO
CCAO
J
DNA_DEPENDENT_DNA_REPLICATION
DNA_REPLICATION
CELL_CYCLE_DNA_REPLICATION
RECOMBINATIONAL_REPAIR
MITOTIC_SISTER_CHROMATID_SEGREGATION
CHROMOSOME_SEGREGATION
STEROID_BIOSYNTHETIC_PROCESS
POSITIVE_REG_OF_SMALL_MOLECULE_METABOLIC_PROCESS
AUTOPHAGOSOME_ORGANIZATION
KERATINOCYTE_DIFFERENTIATION
KERATINIZATION
Enrichment
Down−regulated
Up−regulated
K
Relative metabolic activity
CCAO
BRCCAO
Time (Hours)

Figure S7. Additional characterization of BRCCAOs.

Fig. S7 provides additional analysis and data corresponding to Fig. 7. **(a**) Bright field images of growth of BRCAOs. T=0 is defined as the day of switching medium from expansion medium to non-canonical WNT stimulating medium. Total time period is 15 days. Scale bars indicate 400 µm. **(b)** Whole mount confocal image of BRCCAO for KRT7 (red), nuclei are stained by DAPI (blue), scale bar indicates 200 µm. **(c)** Immunofluorescence staining of BRCCAOs for Zonula occludens-1 (ZO-1, green) and nuclei (DAPI, blue) indicating no cell polarization in the branching structures. Bottom-left shows a magnification of the center (non-branching part) of the same BRCCAO with ZO-1 signal indicating cell polarity and tight junction presence. Scale bars indicate 100 µm**. (d)** Whole mount confocal image of Ki67, a marker for proliferation, showing no evidence for tip-driven growth occurring. Scale bar indicates 400 µm. **(e)** Percentage of positive cells for EdU incorporation as analyzed by flow cytometry in CCAOs and BRCCAOs (n=3). **(f)** Representative BRCO and in **(g)** a BRCCAO obtained from numerical simulations of the BARW model, scale is equal for both schematics (see Methods for parameter values and scale bar indicates 500 µm), active tips are labeled green, terminated tips are black. **(h)** PCA plot displaying paired CCAOs and BRCCAOs. **(i)** Heatmap of top 75 DE genes when comparing BRCCAOs and CCAOs. **(j)** GSEA of the top 5 GO: biological processes up and downregulated in BRCCAOs. **(k)** Metabolic activity indicating cellular activity over the period of 72h before addition of (chemo)therapeutics. No significant difference can be observed. All experiments for BRCCAOs and CCAOs are performed with the biological triplicates.